

AFRL-IF-RS-TR-2001-258
Final Technical Report
December 2001



MICROELECTROMECHANICAL SYSTEMS (MEMS) AND SOLDER SELF-ASSEMBLY FOR 3-D MEMS AND MEMS ARRAYS

University of Colorado

Sponsored by
Defense Advanced Research Projects Agency
DARPA Order No. G176/0

APPROVED FOR PUBLIC RELEASE; DISTRIBUTION UNLIMITED.

The views and conclusions contained in this document are those of the authors and should not be interpreted as necessarily representing the official policies, either expressed or implied, of the Defense Advanced Research Projects Agency or the U.S. Government.

20020308 068

AIR FORCE RESEARCH LABORATORY
INFORMATION DIRECTORATE
ROME RESEARCH SITE
ROME, NEW YORK

This report has been reviewed by the Air Force Research Laboratory, Information Directorate, Public Affairs Office (IFOIPA) and is releasable to the National Technical Information Service (NTIS). At NTIS it will be releasable to the general public, including foreign nations.

AFRL-IF-RS-TR-2001-258 has been reviewed and is approved for publication.

APPROVED:



THOMAS RENZ
Project Engineer

FOR THE DIRECTOR:



MICHAEL TALBERT, Maj., USAF, Technical Advisor
Information Technology Division
Information Directorate

If your address has changed or if you wish to be removed from the Air Force Research Laboratory Rome Research Site mailing list, or if the addressee is no longer employed by your organization, please notify AFRL/IFTC, 26 Electronic Pky, Rome, NY 13441-4514. This will assist us in maintaining a current mailing list.

Do not return copies of this report unless contractual obligations or notices on a specific document require that it be returned.

REPORT DOCUMENTATION PAGE			Form Approved OMB No. 0704-0188	
Public reporting burden for this collection of information is estimated to average 1 hour per response, including the time for reviewing instructions, searching existing data sources, gathering and maintaining the data needed, and completing and reviewing the collection of information. Send comments regarding this burden estimate or any other aspect of this collection of information, including suggestions for reducing this burden, to Washington Headquarters Services, Directorate for Information Operations and Reports, 1215 Jefferson Davis Highway, Suite 1204, Arlington, VA 22202-4302, and to the Office of Management and Budget, Paperwork Reduction Project (0704-0188), Washington, DC 20503.				
1. AGENCY USE ONLY (Leave blank)		2. REPORT DATE DECEMBER 2001		3. REPORT TYPE AND DATES COVERED Final May 98 - May 01
4. TITLE AND SUBTITLE MICROELECTROMECHANICAL SYSTEMS (MEMS) AND SOLDER SELF-ASSEMBLY FOR 3-D MEMS AND MEMS ARRAYS			5. FUNDING NUMBERS C - F30602-98-1-0219 PE - 63739E PR - E117 TA - 00 WU - 40	
6. AUTHOR(S) Victor M. Bright, Y. C. Lee, and Martin L. Dunn				
7. PERFORMING ORGANIZATION NAME(S) AND ADDRESS(ES) University of Colorado The Regents of the University of Colorado Office of Contracts and Grants 1511 University Avenue, Room 206 Boulder Colorado 80309-0572			8. PERFORMING ORGANIZATION REPORT NUMBER N/A	
9. SPONSORING/MONITORING AGENCY NAME(S) AND ADDRESS(ES) Defense Advanced Research Projects Agency Air Force Research Laboratory/IFTC 3701 North Fairfax Drive 26 Electronic Parkway Arlington Virginia 22203-1714 Rome New York 13441-4514			10. SPONSORING/MONITORING AGENCY REPORT NUMBER AFRL-IF-RS-TR-2001-258	
11. SUPPLEMENTARY NOTES Air Force Research Laboratory Project Engineer: Thomas Renz/IFTC/(315) 330-3423				
12a. DISTRIBUTION AVAILABILITY STATEMENT APPROVED FOR PUBLIC RELEASE; DISTRIBUTION UNLIMITED.			12b. DISTRIBUTION CODE	
13. ABSTRACT (Maximum 200 words) One method of MEMS manufacturing is surface micromachining. The challenge of this method is its inability to produce structures with high aspect ratio due to its planar fabrication. The surface micromachined structures, however, can be assembled out of the plane of the substrate to achieve a 3-dimensional function. A common solution for assembly of highly 3-D MEMS is the fabrication of hinged components that can be lifted or "popped-up" into assembled structures. The hinged structures then can be combined with microactuators for positioning and operating MEMS. Hinged devices are commonly assembled manually, a time consuming and delicate process which leads to low yield and inability to produce devices in large quantities. The research objective of our work focused on elimination of fabrication limitations by using two novel self-assembly techniques for MEMS: assembly using integrated micromechanisms (MEMS Self-Assembly), and assembly using a solder re-flow process (Solder Self-Assembly). The self-assembly of MEMS eliminates the need for manual assembly or adjustment, thus making batch fabrication feasible. In addition to manufacturability, the self-assembly of MEMS may be particularly important for applications which require reliable deployment and remote assembly of delicate structures in the operating environment or readjustment of components to align a system for optimal performance. This work was divided into eight sections: The study and development of self-assembled corner cube reflectors, self assembled 3-D switches, 3-D micro-robot legs, hybrid assembly structures, and advanced structures, design for MEMS mechanism driven self-assembly, design for surface tension driven self-assembly, and quality and reliability of self-assembled MEMS.				
14. SUBJECT TERMS Microelectromechanical Systems, MEMS, 3-D MEMS, MEMS Fabrication			15. NUMBER OF PAGES 64	
			16. PRICE CODE	
17. SECURITY CLASSIFICATION OF REPORT UNCLASSIFIED	18. SECURITY CLASSIFICATION OF THIS PAGE UNCLASSIFIED	19. SECURITY CLASSIFICATION OF ABSTRACT UNCLASSIFIED	20. LIMITATION OF ABSTRACT UL	

Abstract

Current advances in microfabrication allow for implementation of miniaturized electro-mechanical systems that fit on a single integrated circuit die. Micro-electro-mechanical systems (MEMS) have many practical benefits, including integration with control and signal processing electronics, batch-fabrication, and low cost. Moreover, the small individual mass of the micromachined devices leads to superior ruggedness and fast system response time, making MEMS ideal for a variety of military and commercial applications.

One method for MEMS manufacturing is surface micromachining. The challenge with this method is its inability to produce structures with high aspect ratio due to its planar fabrication. The surface micromachined structures, however, can be assembled out of the plane of the substrate to achieve a 3-dimensional function. A common solution for assembly of highly 3-dimensional MEMS is the fabrication of hinged components that can be lifted or "popped-up" into assembled structures. The hinged structures can then be combined with microactuators for positioning and operating MEMS. Hinged devices are commonly assembled manually, a time-consuming and delicate process which leads to low yield and inability to produce devices in large quantities. The research objectives of our work focused on elimination of such fabrication limitations by using two novel self-assembly techniques for MEMS: assembly using integrated micromechanisms (referred to as *MEMS Self-Assembly*), and assembly using a solder reflow process (referred to as *Solder Self-Assembly*). The self-assembly of MEMS eliminates the need for manual assembly or adjustment, thus making batch fabrication feasible. In addition to manufacturability, the self-assembly of MEMS may be particularly important for applications which require reliable deployment and remote assembly of delicate structures in the operating environment or readjustment of components to align a system for optimum performance. Specifically, this work was divided into eight subsections:

- The study and development of self-assembled corner cube reflectors.
- The study and development of self-assembled 3D switches.
- The study and development of 3D micro-robot legs.
- Design for MEMS mechanism driven self-assembly.
- Design for surface tension driven self-assembly.
- The study and development of hybrid assembly structures.
- The study and development of advanced structures.
- The quality and reliability of self-assembled MEMS.

Table of Contents

1. Summary of Research Objectives	1
2. Technical Status Report	2
2.1 Status of Effort	2
2.2 Research Summary	4
Task 1: 3-D Corner Cube Reflector (CCR)	4
Task 2: Array of 3-D Switches	6
Task 3: Array of 3-D Microrobot Legs	7
Task 4: Design for MEMS Self-Assembly	9
Task 5: Design for Solder Self-Assembly	11
Task 6: Hybrid Technology	26
Task 7: Futuristic MEMS	27
Task 8: Quality and Reliability	31
3. Publications Relevant to This Effort and Technology Transfer	49

List of Figures

Figure T1-1: Assembled CCR (a), and associated thermal actuators and micromechanisms (b,c).	4
Figure T1-2: Captured video images, from different perspectives, of solder self-assembled CCRs. (Top) 200 x 200 μm mirror CCR. (Bottom Left) 500 x 500 μm mirror CCR. (Bottom Right) 500x500 μm reflector.	5
Figure T1-3: Experimental setup for verifying operation of the CCR.	5
Figure T2-1: (a) SEM of a normally closed (N.C.) and two normally open (N.O.) electrostatically actuated switches and (b) a top view of the same switches showing electrical connections.	6
Figure T2-2: A close view of the N.C. switch.	7
Figure T3-2: A solder self-assembled two-degree-of-freedom microrobot leg showing close views of the left and right indium solder joints and the electro-mechanical linkage isolating the right solder joint from the leg.	8
Figure T3-3: A solder self-assembled one-degree-of-freedom microrobot leg showing a close view of the center indium solder joints and outlines of gold pads.	8
Figure T4-1: CAD of the vertically deflecting thermal actuator. The scale is in micrometers and corresponds to the scale in Figure T4-2.	9
Figure T4-2: The calculated temperature distribution throughout the vertically deflecting thermal actuator's hot and cold arm when supplied by 2.5 mA at 2.5 V.	9
Figure T4-3: Simulated deformation of the vertically deflecting thermal actuator with an average hot/cold arm temperature difference of 158 $^{\circ}\text{C}$. The predicted tip deflection is 4 μm .	9
Figure T4-4: SEM and interferometric microscope measurement of a stressed cantilever.	10
Figure T4-5: Microrobot leg assembly with stressed cantilevers.	10
Figure T4-6: SDA assembly of a mirror. Left: video stills of a single mirror being assembled using an array of scratch drive actuators. Top right: diagram of SDA driven assembly design. Bottom right: SEM of basic SDA assembly for a mirror.	11
Figure T5-1: Solder model for a solder-assembled hinged plate rotated to 45 $^{\circ}$.	11
Figure T5-2: Example of a solder-assembled hinged plate.	11
Figure T5-3: Comparison between predicted and measured final angles for solder-assembled single-hinged plates.	12
Figure T5-4: Side-locked plate.	13
Figure T5-5: Kickstand locked plate.	13
Figure T5-6: Approximation of solder joint with simple geometric shapes.	13
Figure T5-7: Comparison of the two models and a volume normalized plot of equilibrium angle and solder volume useful for square plates of an arbitrary size.	14
Figure T5-8: (Left) <i>Surface Evolver</i> predictions of surface energy for the range of possible hinge positions. (Right) Diagram of hinge positions. The lowest energy position is at the lower right position (0.5, -1.375).	15
Figure T5-9: SEM photos of sample hinge pin positions that can result from varying design parameters.	16
Figure T5-10: Abaqus FEM of deformation occurring due to solder solidification and shrinkage. (Left) Defined structural areas. (Right) Resulting deformation scaled by a factor of 10.	16
Figure T5-11: Finite element model of a solder assembled MEMS plate. Top Left: residual doping stresses and substrate contact. Top Right: residual doping stresses but no substrate contact. Bottom Left: substrate contact but no residual doping stresses. Bottom Right: no residual doping stresses and no substrate contact.	16
Figure T5-12: (left) Diagram of basic plate structure. (right) SEM photo of basic plate structure.	17
Figure T5-13: (left) Sample optimized pad shape for simple plate structure. (Right) Simulated resultant deformation where red is ~ 1.5 microns deflection and dark blue is zero.	17
Figure T5-14: Comparison of results: (top) prediction when no lock or hinges are used, (middle) prediction when lock and hinge position are poorly chosen. (bottom) Algorithm prediction for optimum pad size and lock/hinge position.	18
Figure T5-16: Diagram of basic test structures and SEM of example test structures.	20
Figure T5-17: Plots of sample endpoint measurements versus the desired position for the seven two-plate angle combinations. Lower right: sample photo measurement of a typical 135/135 device.	21

Figure T5-18: Solder nano-spheres formed by surface tension. Left: SEM of a field of indium micro and nano scale spheres. Middle: Atomic force microscope plot of a field of nano-spheres.	22
Figure T5-19: Consumption of 10 μm gold lines by an 8 mil Sn/Pb solder joint.	22
Figure T5-20: Inter-metallic effects on a solder sphere approximately 25 μm in diameter. The indium solder was deposited on 0.5 μm of gold fabricated through MUMPs.	22
Figure T5-21: Picture of reflowed indium on different sized gold disks.	23
Figure T5-22: Left: Total dewetting of pad (1 minute). Right: Total wetting of pad (10 seconds).	23
Figure T5-23: Diagram and photograph of fluxless vacuum soldering system.	24
Figure T5-24: Depiction of the pick and placement method of a solder sphere and an example of patterned indium before reflow.	25
Figure T5-25: Example of a hinged polysilicon plate assembled to 90° with respect to the substrate using AZP4620 photoresist.	25
Figure T6-1: Solder self-assembled plate heated to solder melting point using integrated polysilicon resistive heater lines.	26
Figure T6-2: Example of gold-on-polysilicon bi-morph cantilevers combined with solder assembly.	27
Figure T6-3: Micromirror array combined with solder assembly; micromirrors are lifted parallel to the substrate to achieve greater angle of rotation.	27
Figure T7-1: SEM of a polysilicon box.	28
Figure T7-2: A MEMS garage with opening door.	28
Figure T7-3: A 14 hinged-plate structure.	28
Figure T7-4: Mirrors assembled using solder self-assembly but attached via linkages to allow for external actuation methods.	28
Figure T7-5: Five-plate hook mechanism. Each plate is 400x450 μm	29
Figure T7-6: Linked-plate solder-assembled fiber grippers grasping a 200 micron diameter optical fiber.	29
Figure T7-7: Solder assembled antenna. Device stands 1 cm tall and is 100 μm wide and 2 μm thick. It was assembled using a single 8-mil diameter, 63% Sn / 37% Pb, solder sphere.	29
Figure T7-8: (a) Captured video image of the micro axial flow fan during operational testing with exploded view of 4 of the solder joints used to assemble the fan blades. (b) Scanning electron micrograph of a micro axial flow fan.	30
Figure T7-9: The top shows captured video images of an unreleased micro axial flow fan and the assembly sequence, after release, while solder is assembling the fan blades during heating on a hot plate. The bottom is a SEM showing the SDA rotary motor and solder joints with an exploded view of the fan blade hinges.	30
Figure T8-1-1: (a) SEM photo of gold/polysilicon plate (MUMPS 28) that bends upward from the substrate. (b) Capacitive plate (gold/polysilicon) on a transferred MEMS structure is substantially warped due to residual stresses.	31
Figure T8-1-2: Deformation of a 500 μm x 420 μm , 2 μm thick polysilicon plate with a 0.5 μm thick 125x125 μm gold pad. The plate was assembled with an 8 mil solder ball located underneath the plate.	31
Figure T8-2-1: (a) Scanning white light interferometric microscope that is used to measure the full field deformed shapes; (b) optical drawing of the interferometric microscope.	32
Figure T8-2-2: Setup for measuring plate deformation at various temperatures.	32
Figure T8-2-3: Instrumented microindenter.	32
Figure T8-3-1: (a) Curvature study for fixed thickness of gold. (b) Stress across the thickness for fixed thickness of gold.	33
Figure T8-3-2: SEM of L, D = 300 μm gold/polysilicon plate structures. The support post and etch holes are apparent and the x-y coordinate system used in subsequent measurements and analysis is identified.	34
Figure T8-3-3: Transverse displacement contours at room temperature for square gold/polysilicon plate structures (L = 150, 200, 250, and 300 μm from left to right): (a) measured, and (b) predicted. 10 contours for each contour plot, each contour band diagram represents a displacement of 0.23 μm , 0.35 μm , 0.45 μm , and 0.6 μm for L = 150 μm , 200 μm , 250 μm , and 300 μm respectively.	35
Figure T8-3-4: Transverse displacement contours at room temperature for circular gold/polysilicon plate structures (D = 150, 200, 250, and 300 μm from left to right): (a) measured, and (b) predicted. 10 contours for each contour plot, each	

contour band diagram represents a displacement of 0.11 μm , 0.24 μm , 0.37 μm , and 0.43 μm for $D = 150 \mu\text{m}$, 200 μm , 250 μm , and 300 μm , respectively.	36
Figure T8-3-5: Average measured (top) and predicted (bottom) curvature as a function of temperature upon cooling from 100°C to room temperature. The curves from top to bottom are for the $L, D = 150, 200, 250$, and 300 μm structures, respectively.	37
Figure T8-3-6: Average predicted curvature as a function of temperature upon cooling from 100°C to room temperature. $L = 300 \text{ mm}$ square plate: $\delta\alpha_g$ from 0.01% of α_g to 1.0 % of α_g	37
Figure T8-3-7: Nondimensional average curvature as a function of temperature change for the linear and nonlinear regimes. Measurements (open symbols for square structures and filled symbols for circular structures) and the prediction (solid line for square and circular structures).	38
Figure T8-3-8: Temperature change required for the initiation of nonlinear geometry effects as a function of plate size and the thickness of polysilicon for the gold/polysilicon microstructures.	39
Figure T8-3-9: Critical temperature change for bifurcation as a function of plate size and the thickness of polysilicon for the square and circular gold/polysilicon microstructures.	39
Figure T8-3-10: Point wise curvature as function of temperature change for the $L = 300 \mu\text{m}$ structure at four locations, $2x/L$. Solid lines are predictions and the open circles are measurements.	39
Figure T8-3-11: Predicted pointwise curvature as function of temperature change for the $L = 300 \mu\text{m}$ structure at various positions $2x/L$ along the x-axis ($y=0$).	40
Figure T8-3-12: Critical average curvature for bifurcation as a function of plate size for the gold/polysilicon microstructures. The solid line is the analytical prediction of Salamon and Masters (1995) based on the constant curvature assumption. The open symbols are predictions from the finite element calculations and the filled symbol is the measurement.	40
Figure T8-4-1: Measured room temperature deformed shapes of polysilicon ($450 \mu\text{m} \times 450 \mu\text{m}$)/gold ($L \times L$) test structures as a function of gold pad dimensions: a) $L = 0 \mu\text{m}$, b) $L = 100 \mu\text{m}$, c) $L = 150 \mu\text{m}$, d) $L = 200 \mu\text{m}$	41
Figure T8-4-2: Measured room temperature deformed shapes of polysilicon ($450 \mu\text{m} \times 450 \mu\text{m}$)/gold ($D = \text{diameter}$) test structures as a function of gold pad dimensions: a) $D = 0 \mu\text{m}$, b) $D = 100 \mu\text{m}$, c) $D = 150 \mu\text{m}$	41
Figure T8-4-3: CAD layout of test structures to understand and guide modeling of MEMS deformation. The gray areas are polysilicon (1.5 μm thick) and the teal areas are gold pads (0.5 μm thick).	41
Figure T8-4-4: Measured room temperature deformed shapes of polysilicon ($300 \mu\text{m} \times 300 \mu\text{m}$)/gold ($L \times L$) test structures as a function of gold pad dimensions. (a) $L = 140 \mu\text{m}$, (b) $L = 160 \mu\text{m}$, (c) $L = 180 \mu\text{m}$, (d) $L = 200 \mu\text{m}$, (e) $L = 250 \mu\text{m}$, (f) $L = 300 \mu\text{m}$	42
Figure T8-4-5: Measured and predicted curvature development during the cooling process from 100 °C to room temperature for the center supported bilayer structures. The bilayer structures are composed of polysilicon plates ($W \times W$, $W=300 \mu\text{m}$) and partially covering gold pad ($L \times L$): (a) $L=180 \mu\text{m}$, (b) $L=250 \mu\text{m}$	42
Figure T8-4-6: Experiment result shows: (a) the $L=250 \mu\text{m}$ structure bifurcates earlier than the $L=180 \mu\text{m}$ structure, (b) the $L=250 \mu\text{m}$ structure bifurcates earlier than the $L=300 \mu\text{m}$ structure.	43
Figure T8-4-7: Prediction results of the cooling process from 100 °C to room temperature for <i>square</i> polysilicon plates ($300 \mu\text{m} \times 300 \mu\text{m}$) with <i>square</i> gold pads ($L \times L$). (a) $L=100, 150, 175, 200$, and 225 μm ; (b) $L=225, 250, 275$, and 300 μm	43
Figure T8-5-1: Curvature variation during the thermal cycle process between 190 °C and room temperature for the center supported gold/poly1+poly2 200 $\mu\text{m} \times 200 \mu\text{m}$ square plate.	44
Figure T8-6-1: Measured curvature development during cooling and a subsequent stress relaxation process at elevated temperature of a 300 $\mu\text{m} \times 300 \mu\text{m}$ gold (0.5 μm thick) / polysilicon (1.5 μm thick) plate structure: (a) Curvature development during cooling from 190 °C to 120 °C; (b) Curvature development due to the stress relaxation when the structure was held at a constant temperature of 120 °C.	45
Figure T8-6-2: Measured and predicted curvature development during isothermal stress relaxation process at elevated temperature of 120 °C. (a) 200 $\mu\text{m} \times 200 \mu\text{m}$ gold / polysilicon plate structure with different thickness of polysilicon; (b) 300 $\mu\text{m} \times 300 \mu\text{m}$ gold/polysilicon plate structure.	45
Figure T8-7-1: (a) Multilayer structures after indium deposition; (b) schematic diagram of the plate and substrate, red dots indicate the locations of the dot test, red lines indicate the locations of the line scan test.	46

Figure T8-7-2: (a) SEM picture of the line scan area. (b) Line scan result which shows Si, Au, and In element component distribution along the scan line.....	46
Figure T8-7-3: (a) SEM picture of the dot test position. (b) Dot test results which show element component at the point.....	47
Figure T8-7-4: Dot map results which show element distribution at the area.....	47
Figure T8-8-1: (a) 5 mil solder balls were put on top of circular structures and reflowed ; (b) SEM picture of room temperature solder shape after reflow.....	48
Figure T8-8-2: Measured and predicted deformation of polysilicon plate with solder in the center. (a) Measured; (b) Predicted.....	48

1. Summary of Research Objectives

Current advances in microfabrication allow for implementation of miniaturized electro-mechanical systems that fit on a single integrated circuit die. Micro-electro-mechanical systems (MEMS) have many practical benefits, including integration with control and signal processing electronics, batch-fabrication, and low cost. Moreover, the small individual mass of the micromachined devices leads to superior ruggedness and fast system response time, making MEMS ideal for a variety of military and commercial applications.

One method for MEMS manufacturing is surface micromachining. The challenge with this method is its inability to produce structures with high aspect ratio due to its planar fabrication. The surface micromachined structures, however, can be assembled out of the plane of the substrate to achieve a 3-dimensional function. A common solution for assembly of highly 3-dimensional MEMS is the fabrication of hinged components that can be lifted or "popped-up" into assembled structures. The hinged structures can then be combined with microactuators for positioning and operating MEMS. Hinged devices are commonly assembled manually, a time-consuming and delicate process which leads to low yield and inability to produce devices in large quantities. The research objectives of our work focused on elimination of such fabrication limitations by using two novel self-assembly techniques for MEMS: assembly using integrated micromechanisms (referred to as *MEMS Self-Assembly*), and assembly using a solder reflow process (referred to as *Solder Self-Assembly*). The self-assembly of MEMS eliminates the need for manual assembly or adjustment, thus making batch fabrication feasible. In addition to manufacturability, the self-assembly of MEMS may be particularly important for applications which require reliable deployment and remote assembly of delicate structures in the operating environment or readjustment of components to align a system for optimum performance.

2. Technical Status Report

2.1 Status of Effort

For reference, the schedule of tasks as set prior to the start of this contract is included below. The shaded time period blocks indicate completed tasks. In the remainder of this report Section 2.2 summarizes the completed work, and Section 3 lists publications/consultations related to this research.

Task 1: 3-D Corner Cube Reflector		Apr-98		Apr-99		Apr-00		Apr-01
a.	Design actuator/micromechanism for MEMS self-assembly							
b.	Demonstrate a MEMS self-assembled reflector							
c.	Develop fluxless solder technology							
d.	Develop a quick solder deposition technique using spheres							
e.	Demonstrate a solder self-assembled reflector							
f.	Demonstrate a reflector assembled using MEMS and solder							
g.	Characterize the performance of the reflector							

Task 2: Array Of 3-D Switches		Apr-98		Apr-99		Apr-00		Apr-01
a.	Demonstrate a solder self-assembled microswitch							
b.	Demonstrate an array of solder self-assembled microswitches							
c.	Characterize the performance of the microswitches							

Task 3: Array of 3-D Microrobot Legs		Apr-98		Apr-99		Apr-00		Apr-01
a.	Demonstrate a MEMS self-assembled microrobot							
b.	Control gas flow effect of the fluxless soldering							
c.	Improve solder deposition technique using an evaporator							
d.	Demonstrate a solder self-assembled microrobot							
e.	Demonstrate a microrobot assembled using solder & MEMS							
f.	Characterize the performance of the microrobots assembled							
g.	Determine the limitations of MEMS assembled microrobots							
h.	Improve deposition techniques for 2-um solder							
i.	Demonstrate a soldered microrobot using <10 um solder							
j.	Explore the use of non-solder materials for microrobots							
k.	Demonstrate a microrobot assembled using MEMS & solder (removed during project kick-off meeting)							
l.	Characterize the performance of the microrobots assembled (removed during project kick-off meeting)							

Task 4: Design For MEMS Self-Assembly		Apr-98		Apr-99		Apr-00		Apr-01
a.	Develop a model of thermal microactuators for mechanisms							
b.	Develop 1-hinge mechanisms using thermal microactuators							
c.	Experimentally determine the actuator model's limitations							
d.	Experimentally verify the 1-hinge mechanisms							

e.	Develop 5-hinge mechanisms using thermal microactuators (removed during project kick-off meeting)						
f.	Experimentally verify the 5-hinge mechanisms (removed during project kick-off meeting)						

Task 5: Design For Solder Self-Assembly		Apr-98		Apr-99		Apr-00	Apr-01
a.	Determine the limitations in scales 100 to 25 um.						
b.	Develop a model to design 1-hinge self-assembly						
c.	Experimentally verify the 1-hinge model's accuracy						
d.	Investigate the use of non-solder materials						
e.	Determine the limitations in scales < 25 um.						
f.	Expand the year-1 model for different solder materials						
g.	Develop a model to design 5-hinge assembly						
h.	Conclude the study of non-solder materials						
i.	Determine the limitations of controlled alignment sequence						
j.	Experimentally verify the 5-hinge model						
k.	Develop and verify a model for controlled alignment sequence						

Task 6: Hybrid Technology		Apr-98		Apr-99		Apr-00	Apr-01
a.	Determine the effect of soldering on MEMS self-assembly						
b.	Define integrated design procedure for the hybrid technology						
c.	Integrate solder and MEMS design models						
d.	Demonstrate hybrid technology using innovative MEMS						

-Task 7: Futuristic MEMS		Apr-98		Apr-99		Apr-00	Apr-01
a.	Explore new MEMS soldered with over 12 hinges (house)						
b.	Explore new MEMS, e.g. doors, using micromechanisms						
c.	Explore new MEMS, e.g. a 2-bedroom house						
d.	Explore new MEMS, e.g. a 3-bedroom house						

Task 8: Quality and Reliability		Apr-98		Apr-99		Apr-00	Apr-01
a.	Develop 3-D deformation models for micromirrors						
b.	Test micromirrors to validate the deformation models						
c.	Test hinged structures' force-deflection relationship						
d.	Integrate the relationship into the MEMS- and solder models						
e.	Identify single-hinge structures' failure modes						
f.	Identify multiple-hinge structures' failure mode						
g.	Quantify mechanical failure on single-hinge structures						
h.	Develop reliability models for single-hinged structures						
i.	Couple the deformation model with solder effects						
j.	Quantify mechanical failure on multiple-hinge structures						
k.	Develop reliability models for multiple-hinged structures						

2.2 Research Summary

Task 1: 3-D Corner Cube Reflector (CCR)

Thermal actuators and micromechanisms have been used in the MEMS self-assembly of a CCR [1]. Figure T1-1 shows scanning electron micrographs (SEMs) of an assembled CCR (a), a vertically deflecting thermal actuator (b), and a horizontally deflecting thermal actuator array of micromotor (c).

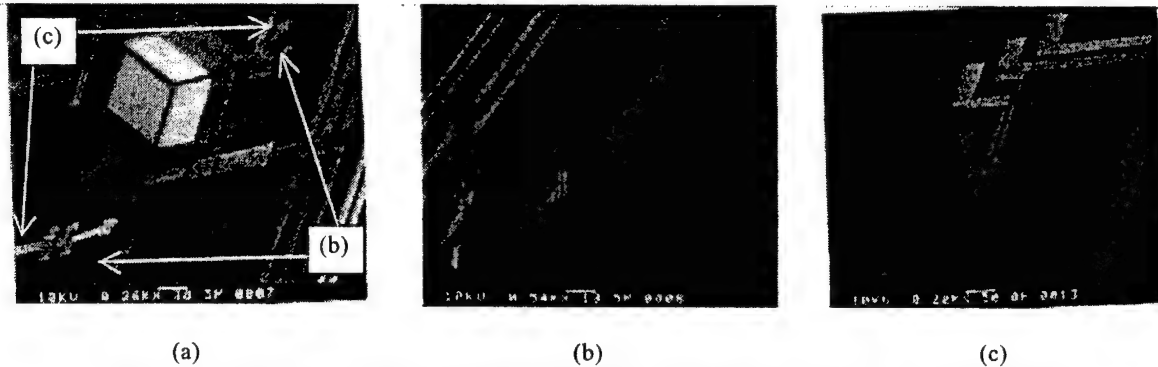


Figure T1-1: Assembled CCR (a), and associated thermal actuators and micromechanisms (b,c).

With reference to Figure T1-1: the assembled mirrors shown in (a) are initially fabricated laying on the substrate; the vertically deflecting actuator shown in (b) gives the mirror an initial lift; and the micromotor shown in (c), but out of view in (a), pushes the mirror the rest of the way up until it is locked into place.

We have developed a fluxless solder technology and a quick solder deposition using solder spheres. Solder spheres can be placed across gold plated pads attached to microstructures. The solder and microstructures are heated to the melting point of the solder while in an atmosphere of nitrogen gas and formic acid vapor [2]. The nitrogen gas and formic acid are used to inhibit and remove metal oxidation, respectively. This technique was used to assemble the CCRs shown in Figure T1-2. The diameter of the 63 % Sn / 37 % Pb solder spheres was 8 mil. A vertically deflecting thermal actuator (model presented in the Task 4 Section) is used to modulate the bottom mirror of the CCR.

Figure T1-3 depicts the experimental setup for determining the functionality of the CCR. Results show that the angle of reflected light deviates from the angle of incidence by less than one degree with zero applied voltage. The CCR thermal actuator is modulated with a 3 V peak square wave.

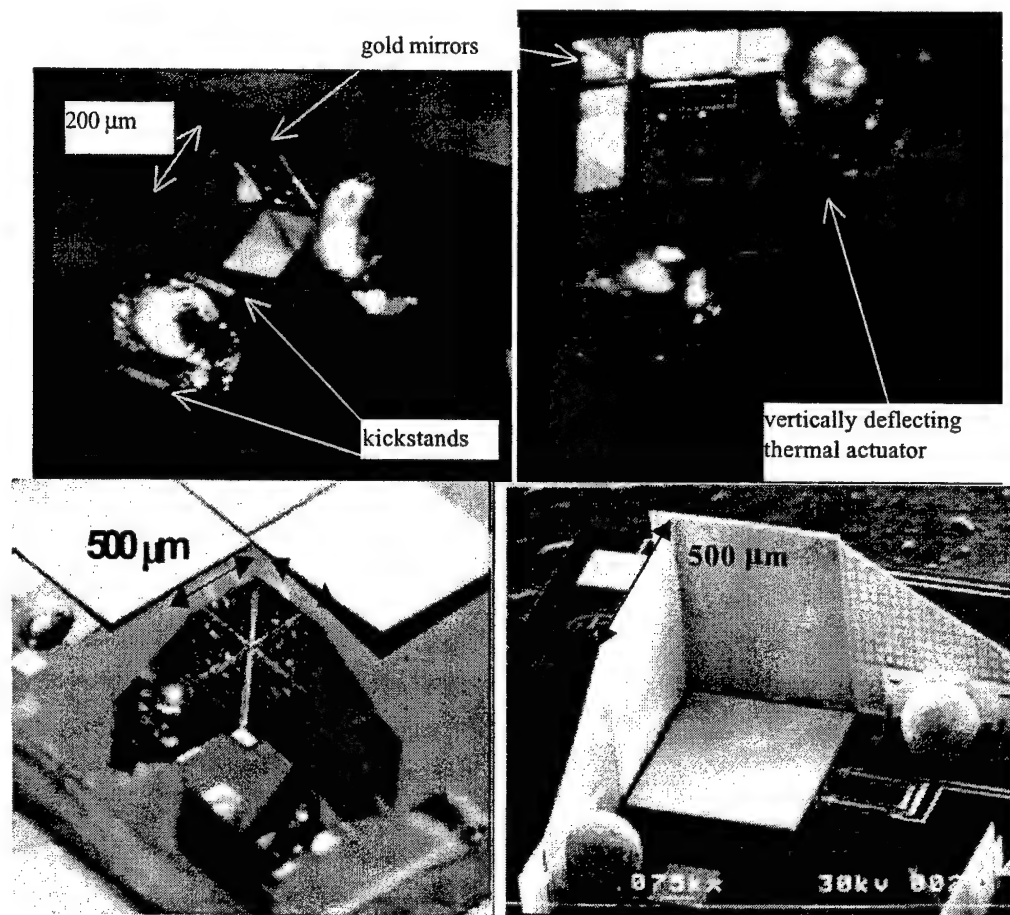


Figure T1-2: Captured video images, from different perspectives, of solder self-assembled CCRs. (Top) 200 x 200 μm mirror CCR. (Bottom Left) 500 x 500 μm mirror CCR. (Bottom Right) 500x500 μm reflector.

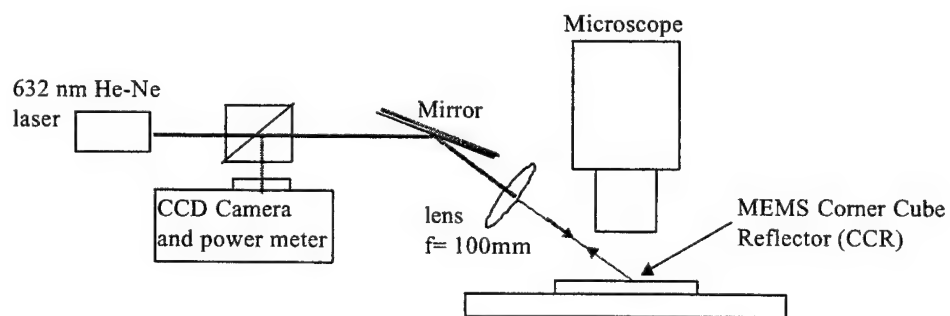


Figure T1-3: Experimental setup for verifying operation of the CCR.

Task 2: Array of 3-D Switches

This section summarizes development of solder-assembled 3D switches. Figure T2-1 (a) is a SEM of two, normally open (N.O.), and one, normally closed (N.C.), electrostatically actuated switches. Figure T2-1 (b) is a top view of the same switches showing the appropriate operation connections.

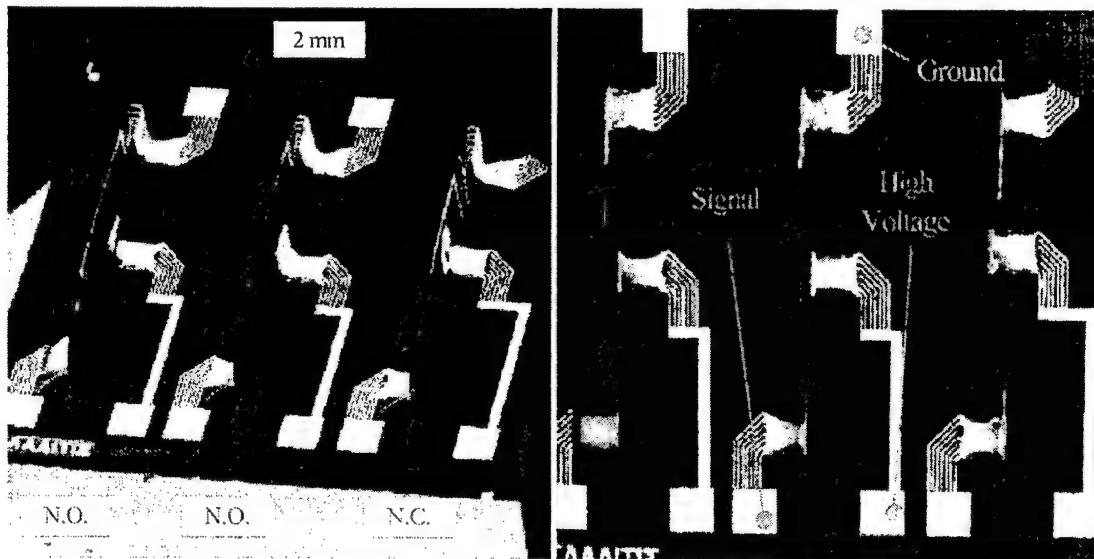


Figure T2-1: (a) SEM of a normally closed (N.C.) and two normally open (N.O.) electrostatically actuated switches and (b) a top view of the same switches showing electrical connections.

The switches were assembled with 4 mil diameter, 63Sn/37Pb, solder spheres. Each plate position was controlled using mechanical stops. The Signal-Ground resistance was measured at $6\ \Omega$. The snap-through voltage for the N.O. switch was 144 V, and 55 V for the N.C. switch. Each switch is comprised of three solder assembled plates: a grounded contact plate, a signal contact plate, and an attraction plate. The N.O. switch is operated by applying a high voltage to the attraction plate, thereby attracting the grounded contact plate and pulling the grounded contact plate against the signal contact plate. The N.C. switch is operated by applying a high voltage to the attraction plate, thereby attracting the grounded contact plate and pulling the grounded contact plate away from the signal contact plate. The grounded and signal contact plates are held in contact at room temperature by utilizing gold on polysilicon residual stress in the grounded contact plate. A close view of the N.C. switch is shown in Figure T2-2.

The solder assembled switch designs, based on three vertical solder-assembled plates, have two drawbacks. The first drawback is attributed to permanent/semi-permanent charge buildup in the plates. The charge buildup may be eliminated in the future by using alternative materials for the plates and/or by proper drive electronics. Secondly, the optimum combination of attraction area and contact plate flexibility is very important. For example, some designs have relatively low attraction voltages because the area of attraction is large, however, the grounded contact plate can undesirably come in contact with the attraction plate. Optimization of attraction area and plate flexibility is no trivial task – a concentrated effort should be made in this switch design if better results are desired.

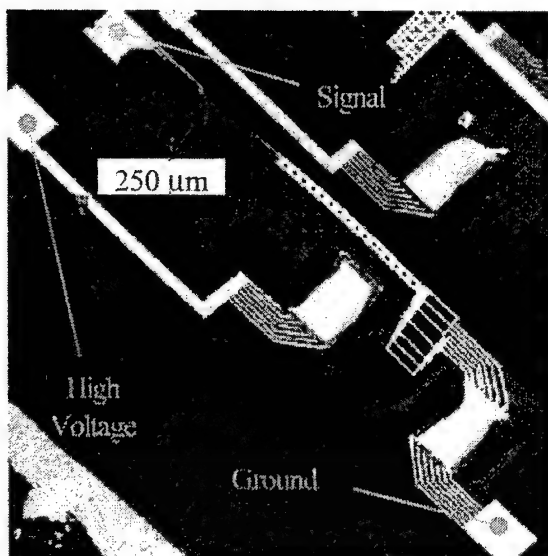


Figure T2-2: A close view of the N.C. switch.

Task 3: Array of 3-D Microrobot Legs

This section summarizes the development of 3-D microrobots. A solder deposition technique using an evaporator has been developed for solder assembly of microrobot legs. In this technique, a 2 μm thick pure indium layer is deposited and patterned using a thick photoresist lift-off process. The indium is reflowed in a nitrogen gas and formic acid vapor. Figure T3-1 is an example of a solder self-assembled microrobot leg array. In this example, indium was deposited and patterned into 118x118 μm squares.

Figure T3-2 shows a single solder self-assembled two-degree-of-freedom microrobot leg with close views of the left and right indium solder joints and the electro-mechanical linkage isolating the right solder joint from the leg. The legs did not assemble to 90° as planned in this design. The specific reasons for not achieving 90° include the deposition of more indium than planned due to the imperfect deposition/lift-off process, mechanical resistance from the flexible locking arms, and the extensive unintentional wetting of the indium to the gold wiring. These sources of error are correctable and can be eliminated in proper design and batch processing. The equivalent of a sphere of indium with diameter of 37 μm was deposited on each set of 25x25 μm gold pads for the microrobot leg shown in Figure T3-2. The outline of the location of the gold pads is also shown in Figure T3-2. The design planned on the indium wetting only within the area of the gold pads, however, the indium jumped its boundaries, wetting extensively along the gold wiring attached to the pads. Again, this error is correctable by providing breaks in the gold layer.

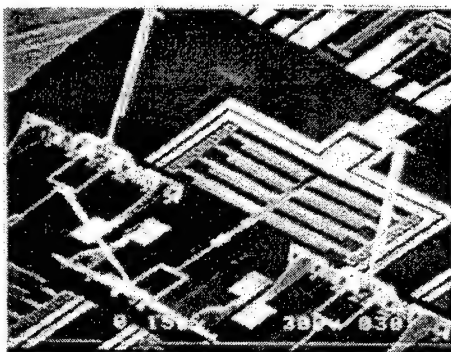


Figure T3-1: A solder self-assembled microrobot leg array after indium reflow.

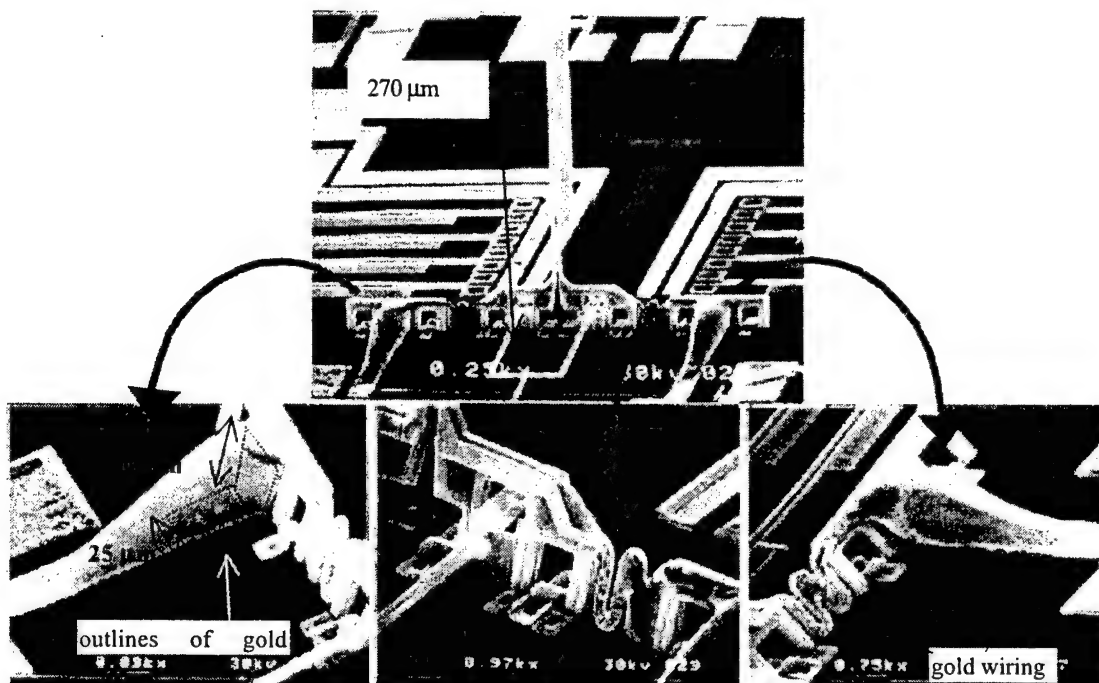


Figure T3-2: A solder self-assembled two-degree-of-freedom microrobot leg showing close views of the left and right indium solder joints and the electro-mechanical linkage isolating the right solder joint from the leg.

Figure T3-3 shows a single solder self-assembled one-degree-of-freedom microrobot leg. The equivalent of a sphere of indium with diameter of $15\text{ }\mu\text{m}$ was deposited on each set of $8\times 10\text{ }\mu\text{m}$ gold pads. This design also did not lift to 90° for the same reasons stated above for the two-degree-of-freedom microrobot leg. Figure T3-3 also reveals the results of reflowing small amounts of indium on gold, note the crystallized indium coating the gold pads and wiring in the close view of the figure.

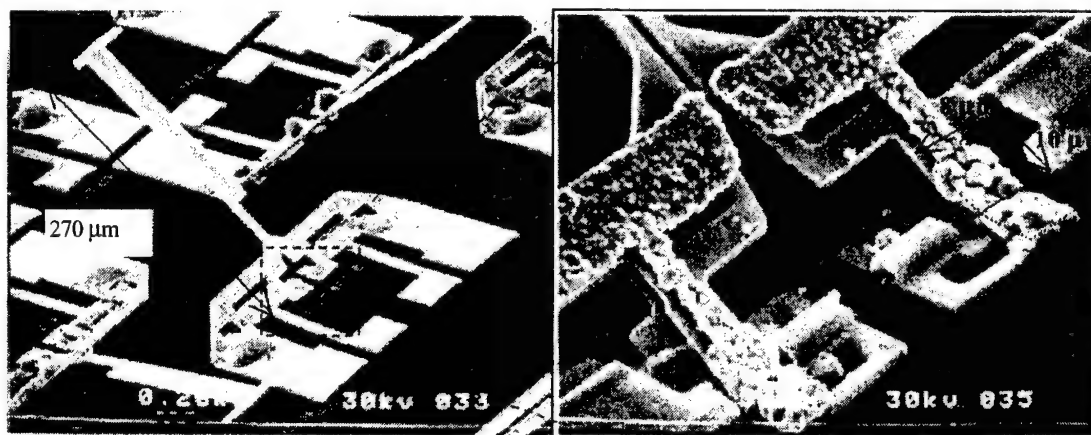


Figure T3-3: A solder self-assembled one-degree-of-freedom microrobot leg showing a close view of the center indium solder joints and outlines of gold pads.

Task 4: Design for MEMS Self-Assembly

This section summarizes work on the designs for MEMS self-assembly. We have developed MEMS self-assembly schemes based on thermal actuation, stressed cantilever actuation, and electrostatic actuation.

We have developed a method to model thermal actuators. First, for the given input current, the temperature distribution throughout the actuator can be calculated by the heat transfer model. The temperature distribution is then used as an input to a finite element model that calculates the thermal expansion and hence the bending of the actuator.

For example, the average temperature (ΔT) difference between a hot arm and the cold arm of the vertically deflecting actuator depicted in Figure T4-1 is calculated by:

$$\Delta T = (\Delta L_{hot} - \Delta L_{cold}) / (\alpha \times L_{hot}) ,$$

where

$$\Delta L_{cold} = \int_L \alpha (T - T_0) dx ,$$

$$\Delta L_{hot} = \int_L \alpha (T - T_0) dx ,$$

α is the coefficient of thermal expansion, and T is temperature. Model results show that the average temperature difference between the hot and cold arm is 158°C . Figure T4-2 is a graph of the simulated temperature distribution throughout the actuator's cold arm and a hot arm. Note, only half of the actuator is modeled due to the symmetry of the design. The data in Figure T4-2 are then used as input to a finite element model that can simulate the deformation of the actuator as shown in Figure T4-3. Simple mechanisms assembled using thermal actuators have been demonstrated with the corner cube reflector and microrobot legs.

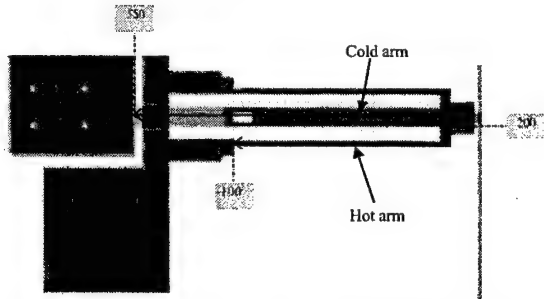


Figure T4-1: CAD of the vertically deflecting thermal actuator. The scale is in micrometers and corresponds to the scale in Figure T4-2.

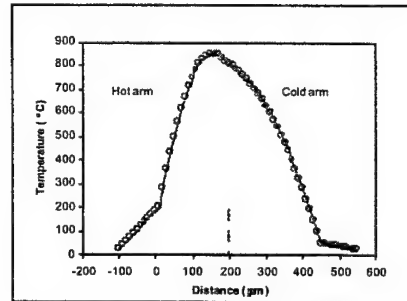


Figure T4-2: The calculated temperature distribution throughout the vertically deflecting thermal actuator's hot and cold arm when supplied by 2.5 mA at 2.5 V.



Figure T4-3: Simulated deformation of the vertically deflecting thermal actuator with an average hot/cold arm temperature difference of 158°C . The predicted tip deflection is $4\text{ }\mu\text{m}$.

We have developed analytic and finite element models to predict the deflection of the tip of a stressed cantilever, such as the cantilever depicted in Figure T4-4. A stressed cantilever is a polysilicon cantilever coated with a $0.5\ \mu\text{m}$ layer of gold. After release of the cantilever, the residual material stress and thermal mismatch of the gold layer on the polysilicon cause the cantilever to curl. Figure T4-5 shows two different designs that use stressed cantilevers to assemble microrobot legs.

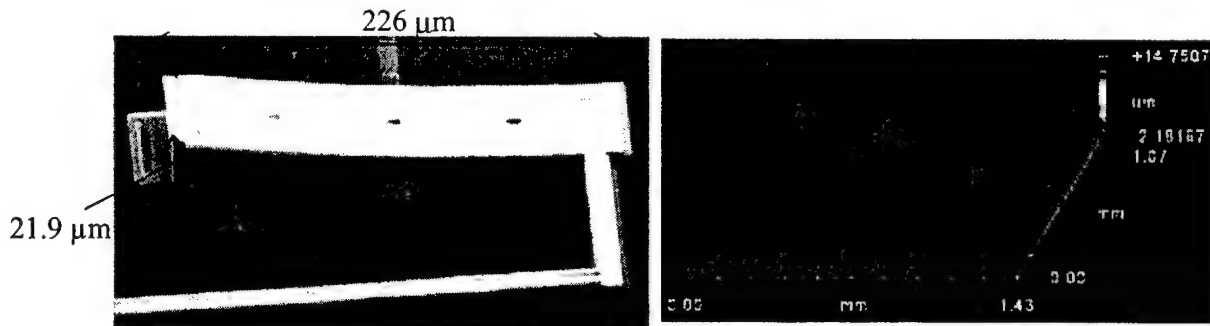


Figure T4-4: SEM and interferometric microscope measurement of a stressed cantilever.

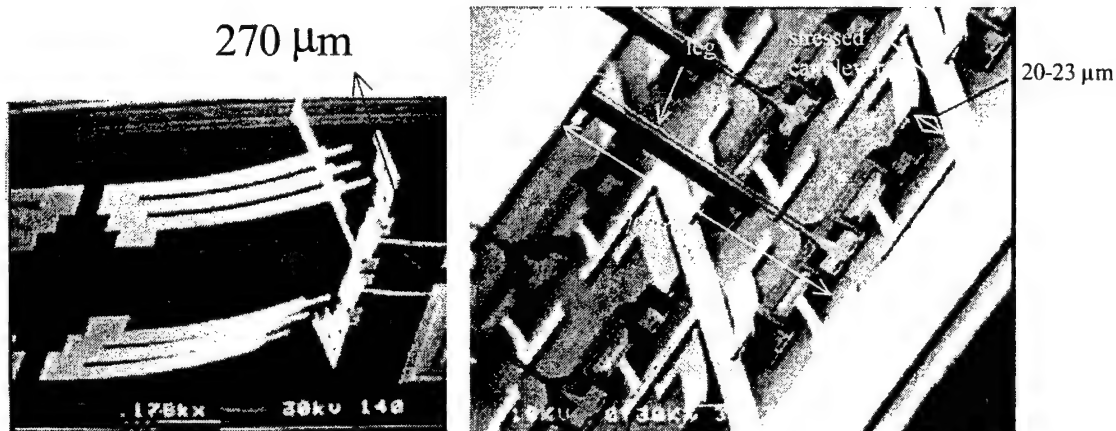


Figure T4-5: Microrobot leg assembly with stressed cantilevers.

Designs using stressed cantilevers for self-assembly of microrobot legs have been successfully demonstrated (Figure T4-5). Designs using stressed cantilevers for assembly of a CCR have also been implemented.

Actuation in the form of electrostatic scratch drives (SDAs) can also be used to assemble MEMS. Figure T4-6 shows one such design that uses SDAs to pull up a mirror. Other designs include a mechanical lock to keep the MEMS at desired position after being pulled into place by the SDAs.

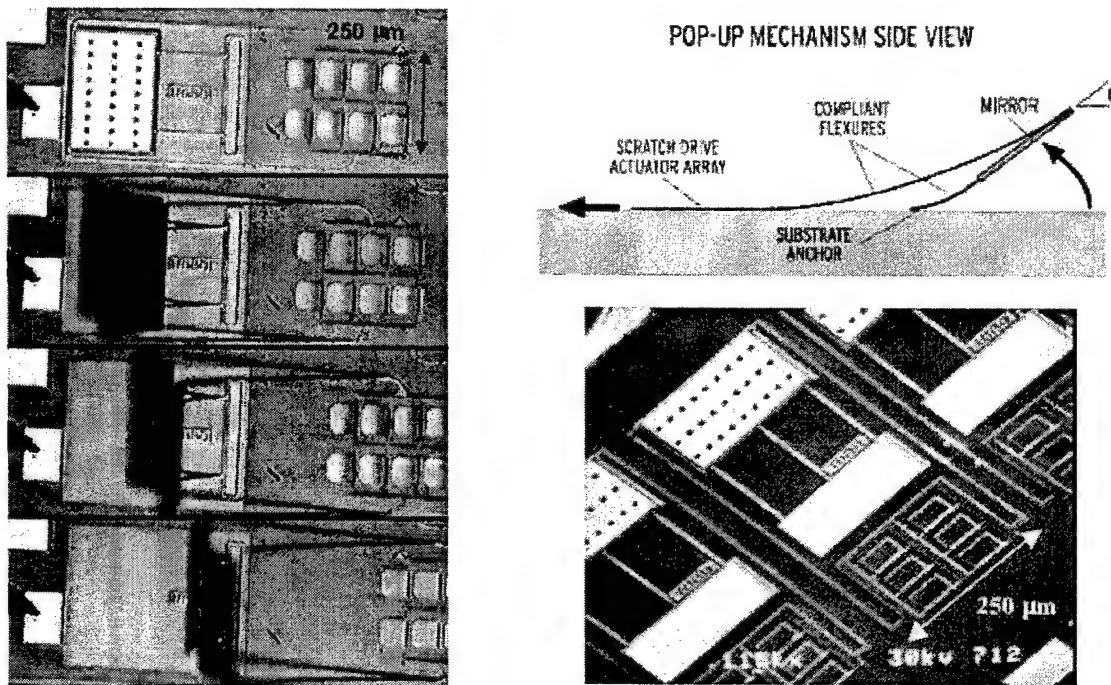


Figure T4-6: SDA assembly of a mirror. Left: video stills of a single mirror being assembled using an array of scratch drive actuators. Top right: diagram of SDA driven assembly design. Bottom right: SEM of basic SDA assembly for a mirror.

Task 5: Design for Solder Self-Assembly

This section summarizes the progress of the designs for solder self-assembly. A model, based on the surface energy minimization of liquids (*Surface Evolver*, Brakke K.A., *Surface Evolver Manual*, Version 1.99, June 1, 1995, University of Minnesota Geometry Center, Minneapolis, MN55455), has been completed that produces a very accurate depiction of the solder behavior [4-6]. Solder type, structure size, geometry, and material properties can be input and the model will calculate the angle of rotation of the MEMS structure. Figure T5-1 shows a completed solder model for a single hinged plate rotated to 45° off the substrate.

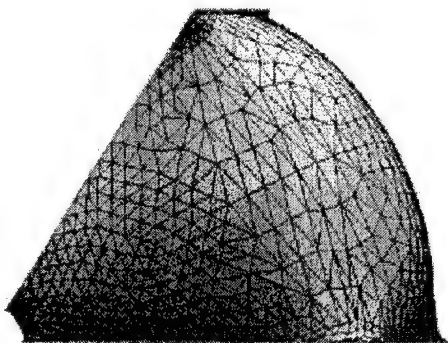


Figure T5-1: Solder model for a solder-assembled hinged plate rotated to 45° .

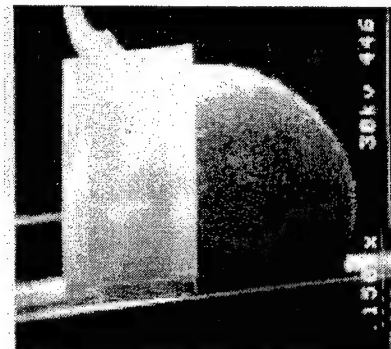


Figure T5-2: Example of a solder-assembled hinged plate.

An example of assembled plate is shown in Figure T5-2. Figure T5-3 illustrates experimental verification of the model. The error bars represent the sensitivity of the model to the variation in solder volume. The (63% Sn, 37%

Pb) solder balls used are commercially manufactured from 0.004" to 0.016", ± 0.001 " in diameter. This is a considerable amount of variation in volume, so its effect is important. The experiments showed that the model predictions were accurate to within ± 2 degrees.

Figure T5-2 is an example of a structure in which assembly is purely controlled by the solder surface energy minimization. The angle of rotation can be controlled fairly precisely, as shown in Figure T5-3; however, there are undoubtedly applications that would require more precise control. Several locking mechanisms have been developed and demonstrated in which the angle of rotation is a function of design geometry. Thus, the effect of solder volume variation is eliminated, and the accuracy of assembly is increased. Two locking mechanisms are shown in Figure T5-4 and Figure T5-5.

The locking mechanism shown in Figure T5-4 is called a "slat side-lock." The central plate is locked in place by two plates that trap it from each side. Tabs on the side of the center plate fit into tapered slots in the trap plates for fine alignment. This type of locking structure involves a sequential set of plate rotations to work correctly. During the heating process, smaller volumes of solder will become molten slightly quicker than larger volumes, and thus can be used for sequential assembly. Also, different types of solder with different melting temperatures could achieve the same effect.

Another way of mechanically controlling the angle of plate rotation is through the use of a "kickstand lock," as shown in Figure T5-5. As the solder rotates the structure out of the plane of the substrate, a rigid bar attached with a spring rotates with the plate until it slides into a hole or groove in the plate, thus stopping the plate movement. If designed correctly, the bar would not only stop the plate rotation, but also lock it in position.

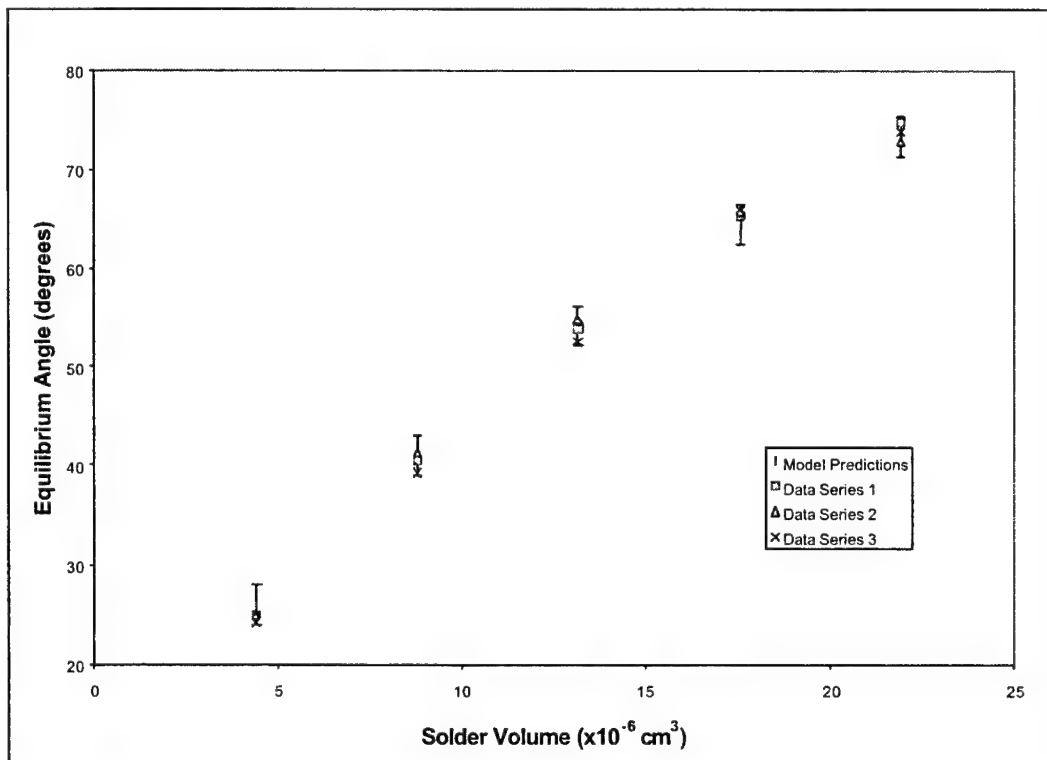


Figure T5-3: Comparison between predicted and measured final angles for solder-assembled single-hinged plates.

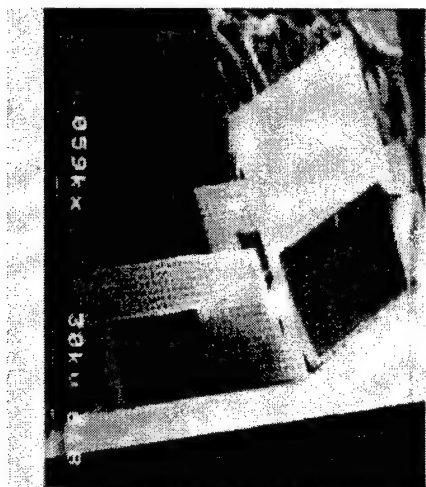


Figure T5-4: Side-locked plate.



Figure T5-5: Kickstand locked plate.

A study was done to gauge the effects of the locking mechanism on the accuracy of MEMS assembly. It was found that, depending on the design of the locking mechanism, the repeatability of the angle of rotation varied from $\pm 0.3^\circ$ for one structure, to $\pm 1.5^\circ$ for another. The best locking mechanism was found to be a kickstand locking mechanism (Figure T5-5) with mechanically rigid locks, with an average rotation of $90.7^\circ \pm 0.3^\circ$ for ten assembled samples.

A second modeling method developed predicts the equilibrium angle of a MEMS plate by approximating the shape and volume of the solder joint with simple geometric shapes as shown in Figure T5-6. This allows the modeling of the changing solder shape by an equation describing the torque on the plate from the surface tension and internal pressure of the solder, and an equation describing the changing shape of the solder joint for any angle. This model is much faster than the *Surface Evolver* model but requires training to be as accurate [8]. Figure T5-7 shows a comparison of the two models and a volume-normalized plot of equilibrium angle and solder volume predicted by this model, useful for square plates of an arbitrary size.

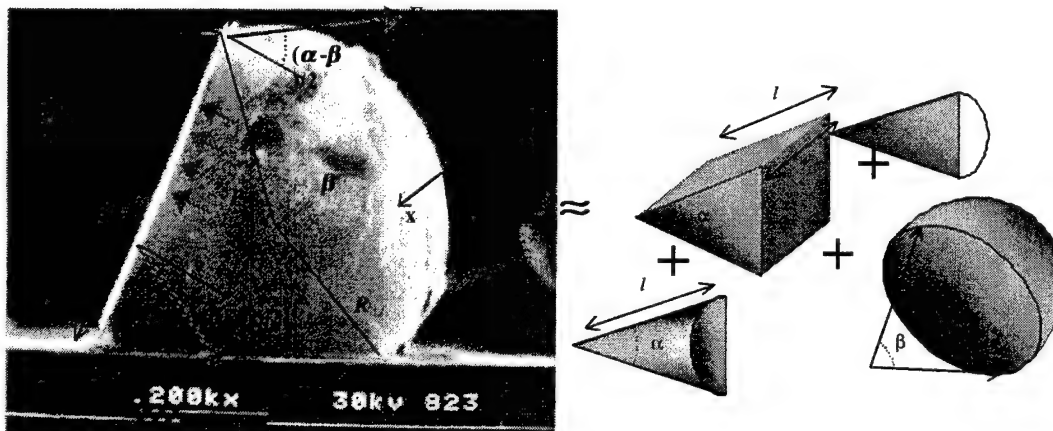


Figure T5-6: Approximation of solder joint with simple geometric shapes.

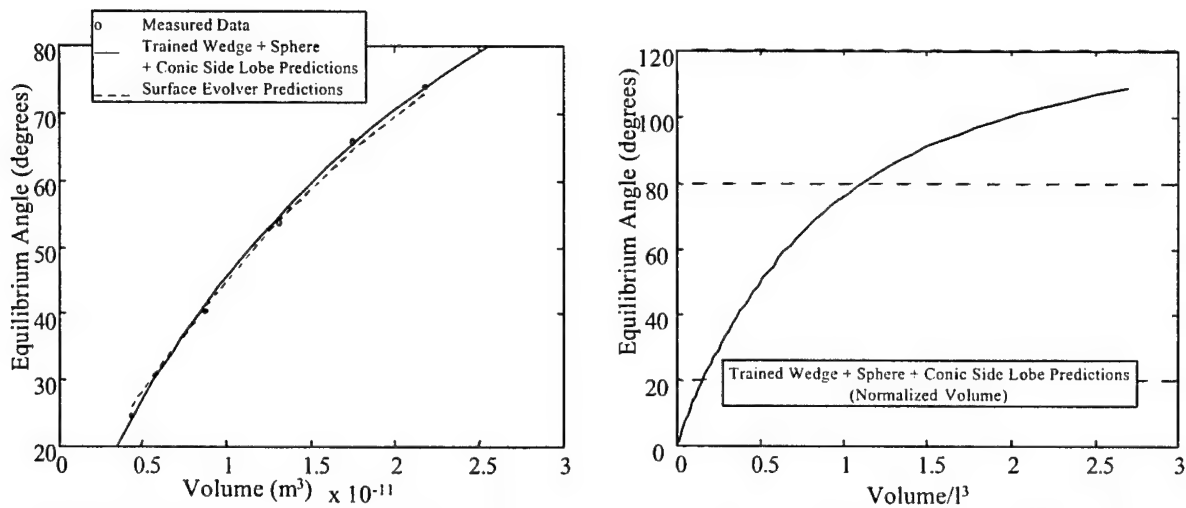


Figure T5-7: Comparison of the two models and a volume normalized plot of equilibrium angle and solder volume useful for square plates of an arbitrary size.

One of the unknowns of the solder self-assembly mechanism is what are its limitations when reducing the size of the MEMS structure. This question was examined and three major areas of limitations were identified: Fabrication Limitations, Modeling Limitations, and Solder Deposition/Metallurgical Limitations.

Fabrication limitations play a monumental role in the viability of reducing the size of the solder self-assembled mechanism. For example, the MUMPs technology used in our research has minimum fabrication geometry of two microns (<http://www.memsrus.com/cronos/svcs/mumps.html>). One aspect in which this is a problem is in the substrate hinge. The play in the hinge that results from the minimum geometry limitation allows the pin of the hinge to move up to two microns. The effects of the hinge play on different size structures, as well as locked and unlocked structures, were assessed. The data show that for the larger solder-assembled structures, the hinge play effect results in a lower angle error than in the smaller structures. Moreover, the mechanically locked assemblies yield consistently lower error in the equilibrium angle.

During solder assembly, the position of the hinge pin is most likely governed by some physical phenomena. If this phenomenon can be understood and predicted, then future designs can be created with this in mind to further increase alignment accuracy of assembly. For this reason, extensive modeling and experiments were performed to understand the hinge position phenomenon. Two possible factors were examined:

- Liquid surface energy controlled positioning. Is the hinge position a function of the potential energy of the system?
- Plate structural effects. Does the plate deformation, solder, and residual stress effect the hinge position?

To evaluate the surface energy effect on hinge position, *Surface Evolver* was used to find the minimum energy of a rotated plate system in which the hinge position is varied according to the two-micron fabrication limitations of the MUMPs process. Figure T5-8 shows an example of such analysis for a plate designed to rotate 90° using an 8-mil diameter 63% Sn / 37 % Pb solder sphere. In this case, there is a definite minimum energy position for the hinge pin (toward the substrate and toward the solder). For all systems modeled, similar result was consistently found.

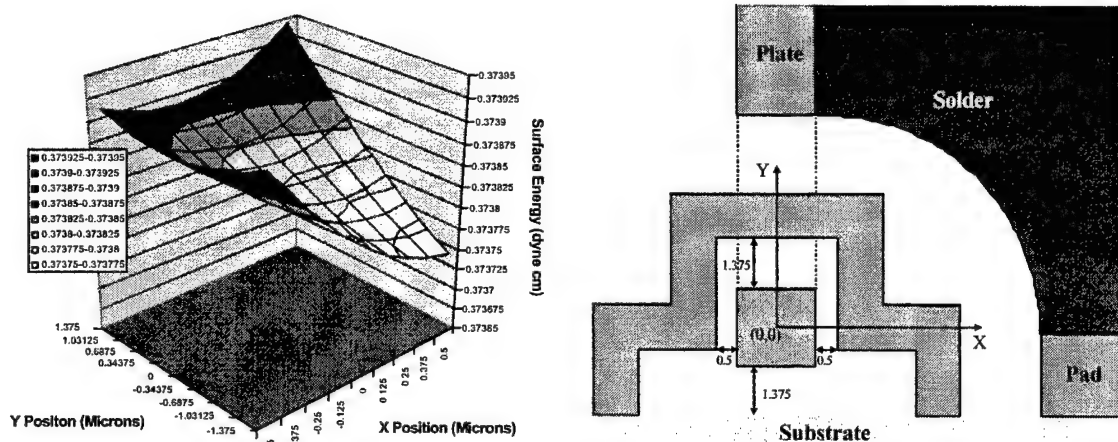


Figure T5-8: (Left) *Surface Evolver* predictions of surface energy for the range of possible hinge positions. (Right) Diagram of hinge positions. The lowest energy position is at the lower right position (0.5, -1.375).

In addition to surface energy effects on hinge position, there are many other fabrication and process issues that will effect the angle control precision such as solder thermal shrinkage and residual stresses. Figure T5-9 shows the effects of such factors. Both hinges in the figure are on identical structures except hinge one is located directly next to the solder pad, and hinge two is farther out on the plate (200 μm). The figure shows that the hinge pin in hinge one is in the *Surface Evolver* predicted position but that for hinge two, the pin has been pushed to a slanted middle position. This is not a random occurrence, finite element (FE) modeling has shown that for this case the residual stresses in the polysilicon have bent the plate backwards.

To evaluate the structural effects on hinge position and angle precision, FE modeling of a solder assembled structure has been performed. The primary effects analyzed are:

- Solder solidification and shrinkage during the cool down step of the reflow process.
- Residual stresses in the structural members.
- Hinge placement along plate edge.
- Kickstand lock placement and design.
- Plate contact with substrate.
- Induced stresses from inter-metallic formation.

Figure T5-10 shows one such result for a 450 x 400 μm plate rotated to 90° using a kickstand mechanical lock. The structure is symmetric (solder is in the center), so only half of the device was modeled, and the solder shape was approximated with a cube for simplicity. In this case, the model results (right) show that the hinge pin will move toward the kickstand lock during deformation. If substrate contact is added, or the kickstand lock is removed the plate will warp in an entirely different manner. Figures T5-11 shows the variety of warpage phenomenon that can occur in the same plate under different conditions (in this case substrate contact and residual doping stresses). All models are under loading due to thermal stresses resulting from thermal expansion mismatches between the solder, gold, and polysilicon. The warpage results are displayed in a contour plot of the deformation in the out of plane direction. In addition to thermal stresses the models account for: (top left) residual doping stresses and substrate contact, (top right) residual doping stresses but no substrate contact, (bottom left) substrate contact but no residual doping stresses, (bottom right) no residual doping stresses and no substrate contact. From this study we see that the position of the hinge pin and warpage of the plate are very dependent on design and process features. Therefore, proper design should minimize or eliminate many sources of plate angle variation and greatly increase the overall assembly precision.

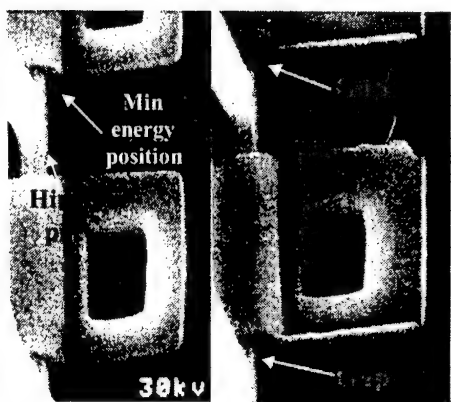


Figure T5-9: SEM photos of sample hinge pin positions that can result from varying design parameters.

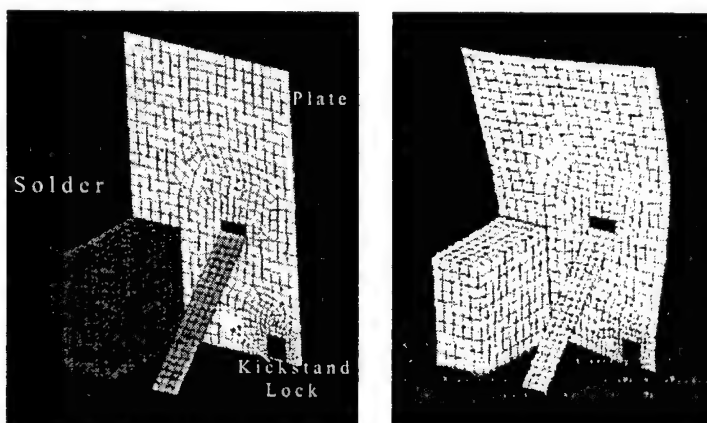


Figure T5-10: Abaqus FEM of deformation occurring due to solder solidification and shrinkage. (Left) Defined structural areas. (Right) Resulting deformation scaled by a factor of 10.

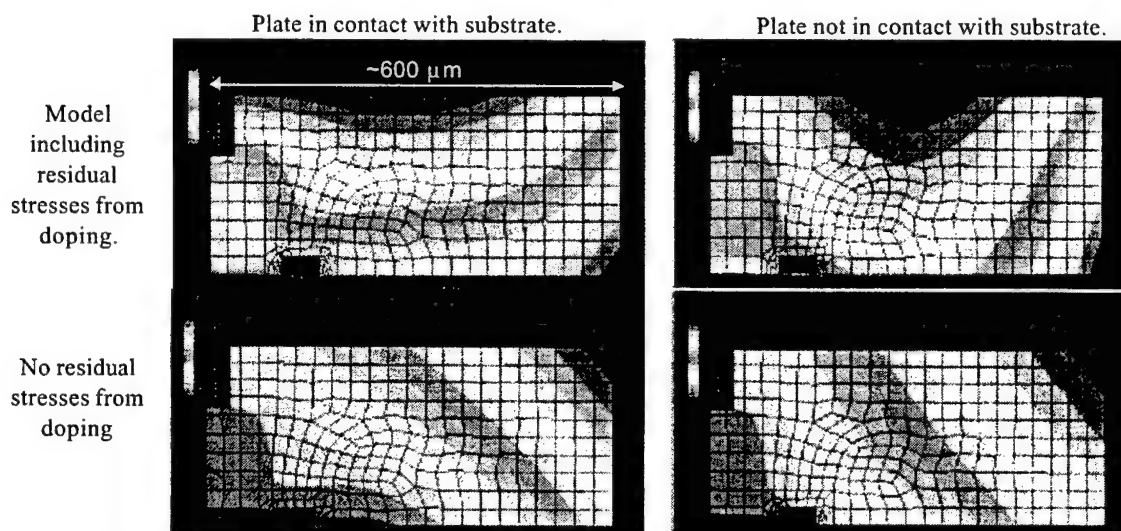


Figure T5-11: Finite element model of a solder assembled MEMS plate. Top Left: residual doping stresses and substrate contact. Top Right: residual doping stresses but no substrate contact. Bottom Left: substrate contact but no residual doping stresses. Bottom Right: no residual doping stresses and no substrate contact.

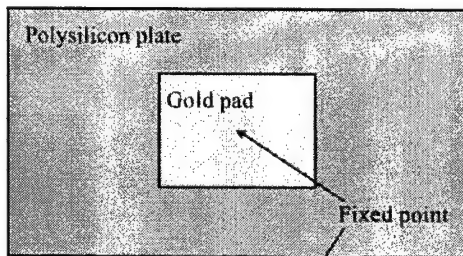
We have developed and experimentally identified FE models that predict the plate behavior for the different process factors stated above. The next step is to optimize the various design configurations such as solder pad shape, hinge position, and plate geometry to yield the optimum assembled angle precision. With the many variables that can be altered the minimum deformation solution is very non-obvious and potentially unsolvable analytically. To resolve this, the finite element models discussed above were integrated with optimization algorithms to find optimum designs.

The finite element software ABAQUS was used to model the structure and extract relevant data, and the optimization algorithm NLPQL was used to optimize the variables. The optimization process is as follows: starting with an initial guess for the variables, the model results and the derivative of those results with respect to each variable is evaluated. These guesses are used to create an ABAQUS input file, which is then processed, and the results extracted. Since this is not an analytical function to be optimized, the derivatives are found using a simple finite difference method. These values are then used by the NLPQL program to generate a new prediction. This process is repeated until the solution converges to some desired tolerance. Since this process could run for many iterations, it was important that an efficient model was used. For this reason Kirchhoff composite shell elements were used over standard 20 node 3D solid elements. The resulting computation time per model evaluation was reduced by

approximately 95%. The average time to converge to an optimum solution, when run on a It's 500 MHz DEC Alpha (DEC personal workstation model 500au) with 768 MB of RAM running DEC Unix V4.0 was about 30 minutes and involved ten step iterations and 40 model evaluations. For the sake of brevity, the optimization presented here is for a simple plate structure and for a basic, building block component, solder self-assembly structure.

The simple plate was studied to gain fundamental insight into the problem of plate deformation minimization, but also because of its application toward designing flatter MEMS mirrors for optical applications. Figure T5-12 illustrates the basic structure, a two microns thick polysilicon plate, point fixed at the center, with a half micron thick gold pad. The parameter to be varied, for pad and plate fixed areas, was the shape of the gold pad. The results to be optimized were chosen to be: the RMS deflection, average deflection, and maximum deflection across the surface of the plate. These values were chosen because combined they best depict the deformation in the plate. For example, it is possible that a plate deformed in a symmetric way could have an average deflection of zero, but by no means be considered flat. Similarly, a plate with a sharp peak in a concentrated area, could still have a low average and rms deflection value. By optimizing all three values, the overall parameter to be optimized is indeed the flatness of the plate. A sample result is shown in Figure T5-13. For 600 micron by 300 micron by two micron thick plate, the resulting optimum pad shape resembled a typical dog bone shape. This result is very non-obvious. It is very unlikely that the same solution could have been found with a standard analytical thin film plate bending model. This strongly illustrates the usefulness of using finite element modeling combined with an optimization algorithm to design MEMS structures.

Top view



Side view

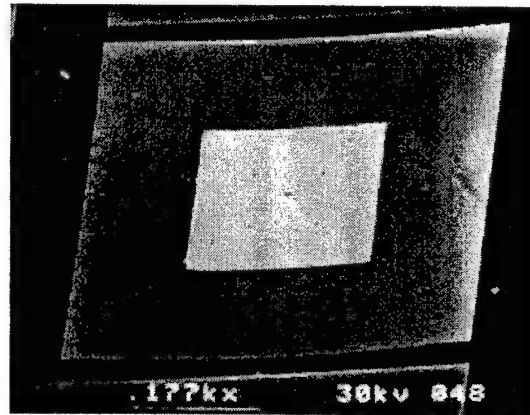
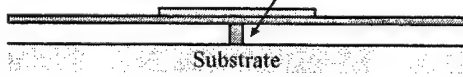


Figure T5-12: (left) Diagram of basic plate structure. (right) SEM photo of basic plate structure.

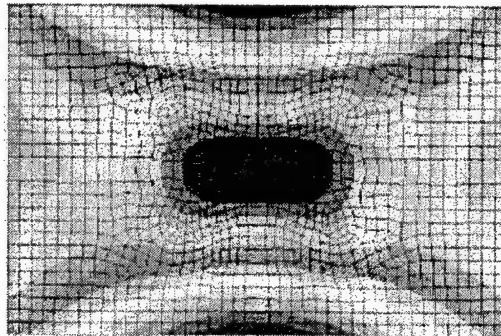
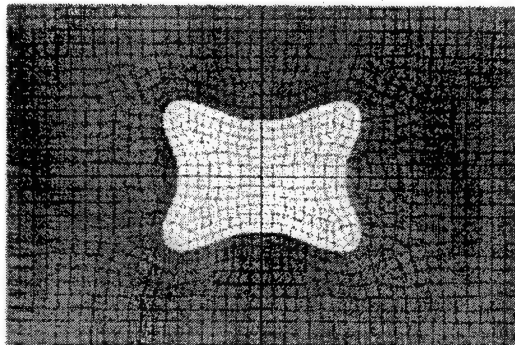


Figure T5-13: (left) Sample optimized pad shape for simple plate structure. (Right) Simulated resultant deformation where red is ~1.5 microns deflection and dark blue is zero.

The basic building block solder self-assembly structure consists of a single solder sphere with a hinge and mechanical lock on either side. A typical plate is between 100-500 microns on either side. A 600 micron wide by 200 micron tall structure was chosen to optimize because ample experimental samples were available to confirm the predictions. For this case, the parameters to be varied were: the contact position of the mechanical lock and plate, the width and height of the solder pad, and the position of the hinge. The only constraint was that the solder pad should remain large enough to be practical for solder deposition processing. The plate was again modeled using composite shell elements, but the solder was simulated with standard three-dimensional solid elements. The interaction of the kickstand and hinges was modeled using contact surface approximations rather than include the actual hinge and kickstand structure into the model. This greatly increased the computational efficiency of the model without effecting accuracy.

As with the simple mirror structure, the optimization program was able to generate a prediction that significantly optimized the deformation in the plate. Again, the values to be minimized were the RMS, average, and maximum deflections of the plate. Figure T5-14 shows three sample cases: a) a prediction in which there is no lock or hinge contact, b) a prediction in which the lock contact position and hinge have been placed with negative results, and c) the algorithm prediction for lock, hinge position, and pad dimensions that will result in minimum deformation. Interestingly, the case in which the lock and hinge were placed poorly resulted in a more severe deformation than with no lock at all. The poor lock and hinge position resulted in a maximum deflection of ~ 5.5 micron and a RMS deflection of ~ 3.4 microns, whereas, the prediction with no lock or hinge resulted in a max deflection of ~ 4 microns and an RMS deflection of ~ 2.1 microns. Finally, the optimized structure showed a significant improvement with a maximum deflection of ~ 0.9 microns and RMS deflection of ~ 0.6 microns. If the max deviation angle (resulting from deformation) were calculated as the deformation from flat as related to its position, the average angle deviation for the optimum structure would be approximately 0.03 degrees.

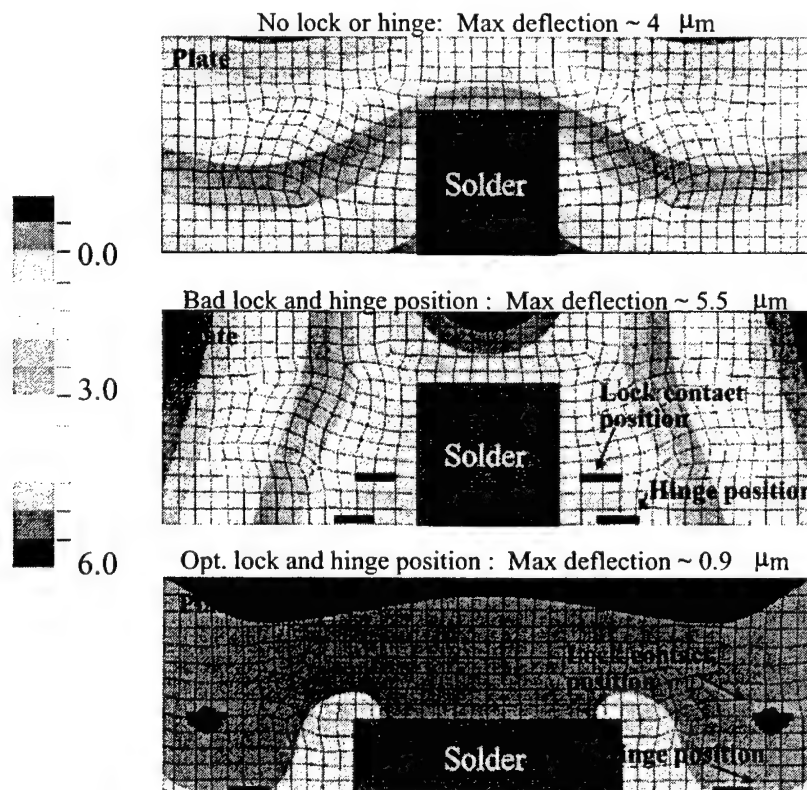


Figure T5-14: Comparison of results: (top) prediction when no lock or hinges are used, (middle) prediction when lock and hinge position are poorly chosen. (bottom) Algorithm prediction for optimum pad size and lock/hinge position.

The reason for the reduced deformation is likely due to the lock and hinge constraints working against the deformation due to thermal mismatch with the solder. The solder shrinkage tends to cup the plate around it like a shroud. By placing the hinge and lock near the edge of the plate, they restrict the plate and force it back toward the desired position. If the lock and hinge are placed too close to the solder, they only amplify the deformation. If they are too far out, the plate will bend significantly between them and the solder joint. It should also be noted that every structure will have its own specific optimum design that depends on its particular geometry and processing. It is also possible that for some applications, global flatness may not be the optimization goal. For example, a solder assembled mirror may need only be flat in a specific reflective region. Also it is possible to maximize curvature for added stiffness in one direction or for some optical application.

The above work discusses the reduction of plate deformation through design optimization. However, one of the primary points of this research is angle precision. At this point it should be reiterated that plate deformation and angle precision are closely related. To summarize, because the hinge position of both the lock and the plate is known and because the fabricated dimensions of the structures are very concise, copies of the same structure should all assemble to the same angle, with very little deviation. But, this is not the case. Because the plate deforms due to processing stresses, the plate will deviate from the intended design. The question is, with plate deformation how precise can angle precision still be? Using a mechanical lock it has been demonstrated that 0.5 degrees of variation in angle precision was possible.

The question is, using the optimized design, what is the achievable angle precision. Although an actual optimized structure has not been tested, similar devices with slightly less than optimal designs have been. In one experiment, six 400-by-400-by-3.5-micron structures were assembled and measured. The pads for each plate were 130-by-130 microns, and the hinge and lock were located at the far edges of the structure. After measurement, the average angle of assembly was 89.78. More importantly, the maximum deviating sample was at 89.69, which is a mere 0.09-degree angle deviation.

The position of more complex structures made from multiple solder joints has also been investigated. Additive rotation and position error occur when multiple solder joints are combined. The individual solder joints and connecting structures (components) have characteristics such as structure dimension, solder volume, temperature, hinge play, and multiple layer induced deformation. All of these characteristics are variable and may or may not be controllable.

The major question is: given a set of individual component tolerances, what is the resulting assembly tolerance? This question will become increasingly important as more complex, multi part, solder-assembled devices, are created. For example, consider the three-hinge optical fiber gripper structure shown in Figure T5-15 (right). The hinge play and solder variation at each joint will combine to create an overall position error at the end.

To investigate the overall contribution of individual component tolerances on the final assembled structure, a model has been created that takes into account all of the possible variations that can occur in a complex n-solder joint solder assembled structure. The model utilizes standard kinematic analysis combined with deformation and solder assembly angle models to find the assembled shape. The range of error for the final assembly is determined by applying tolerance analysis techniques to the model (assembly function in tolerance analysis terms).

The core of tolerance analysis is to find the assembly function that relates all of the component dimensions to the position of interest on the assembly. Figure T5-15 (left) is a sample graphical output of the assembly function for the fiber optic cable gripper. So far, the model requires that the angle variation, hinge play effects, structure geometry variation, and temperature (for effect of bi-layer residual stress induced deformations) be inputted. The purpose of this tolerance analysis model is two-fold:

1. To predict the tolerance of the final position of complex solder assembled structures given existing process capabilities.
2. To investigate the effect of component variations on the assembled structure.

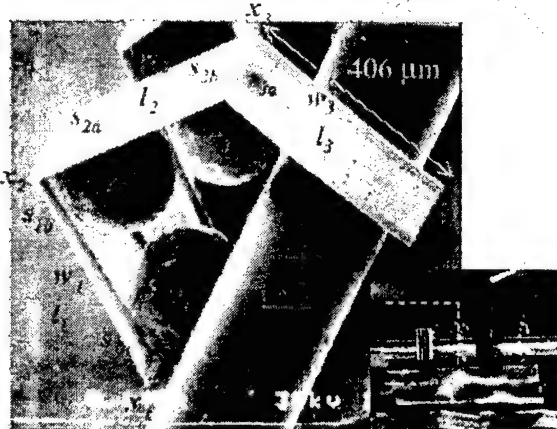
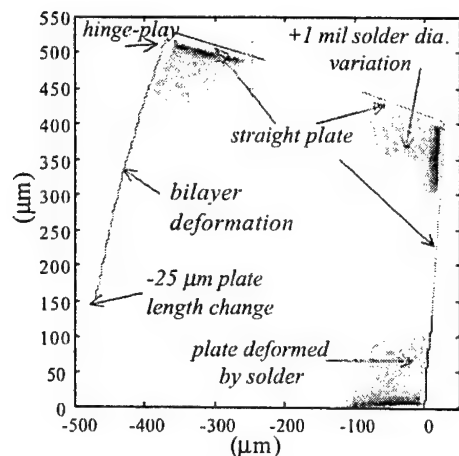


Figure T5-15: (Left) Sample graphical output of the assembly function for a three-plate fiber gripper. (Right): SEM of an optical fiber gripper assembled with 8 mil diameter 63Sn/37Pb solder spheres. The fiber is 220 μm in diameter.

This work is essential for product control and determination of design feasibility in the future commercialization of solder assembled microstructures. Unfortunately, a model is only an estimation of the effects of various parameters on assembly control. To truly understand the effect of various parameters, a set of samples were fabricated that would study the actual effect of structure geometry, internal stresses, pad deformations, hinge play, and joint diameter. The test structure is shown in Figure T5-16. The samples consist of seven two plate assemblies, each designed to assemble to different angle. For example the first structure was designed such that the first solder joint would assemble to 90 degrees and the second joint would assemble to 45 degrees and is thus denoted as 90/45. The other designed variations were 90/90, 90/135, 135/135, 135/90, 135/45, and 45/135. The ## samples of each device were assembled and their tip positions measured. This data is shown in figure T5-17 plotted against the model predictions for each device type. It was found that solder volume variation was the dominant source of variation, followed by the shape of the solder pad. The plate shape, internal stresses and deformation contributed very little, only one twentieth of the impact of the solder volume variation. Interesting the hinge play contributed the smallest amount, about 0.2 percent of the overall impact. This is interesting because the significant amount of possible hinge play could result in significant variation. The reason it does not is because the solder consistently pulls the hinge into the same position.

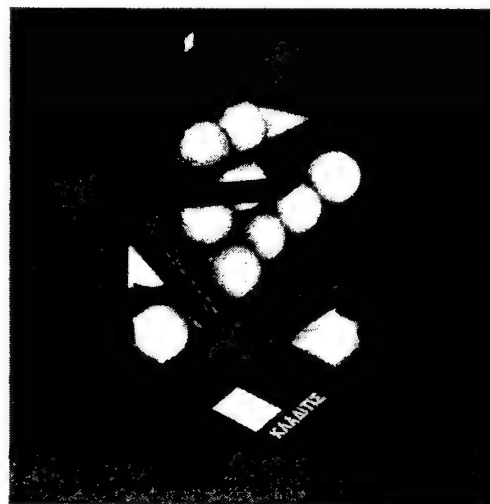
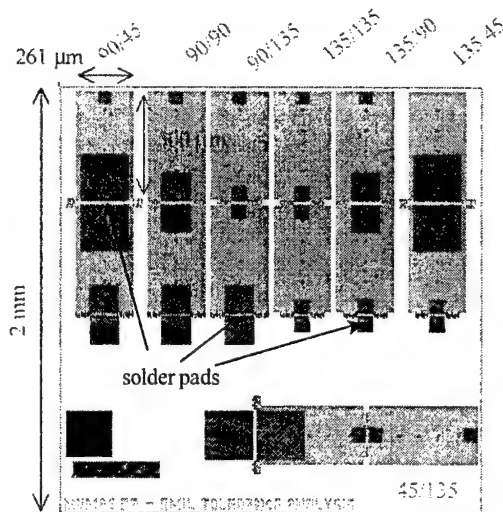


Figure T5-16: Diagram of basic test structures and SEM of example test structures.

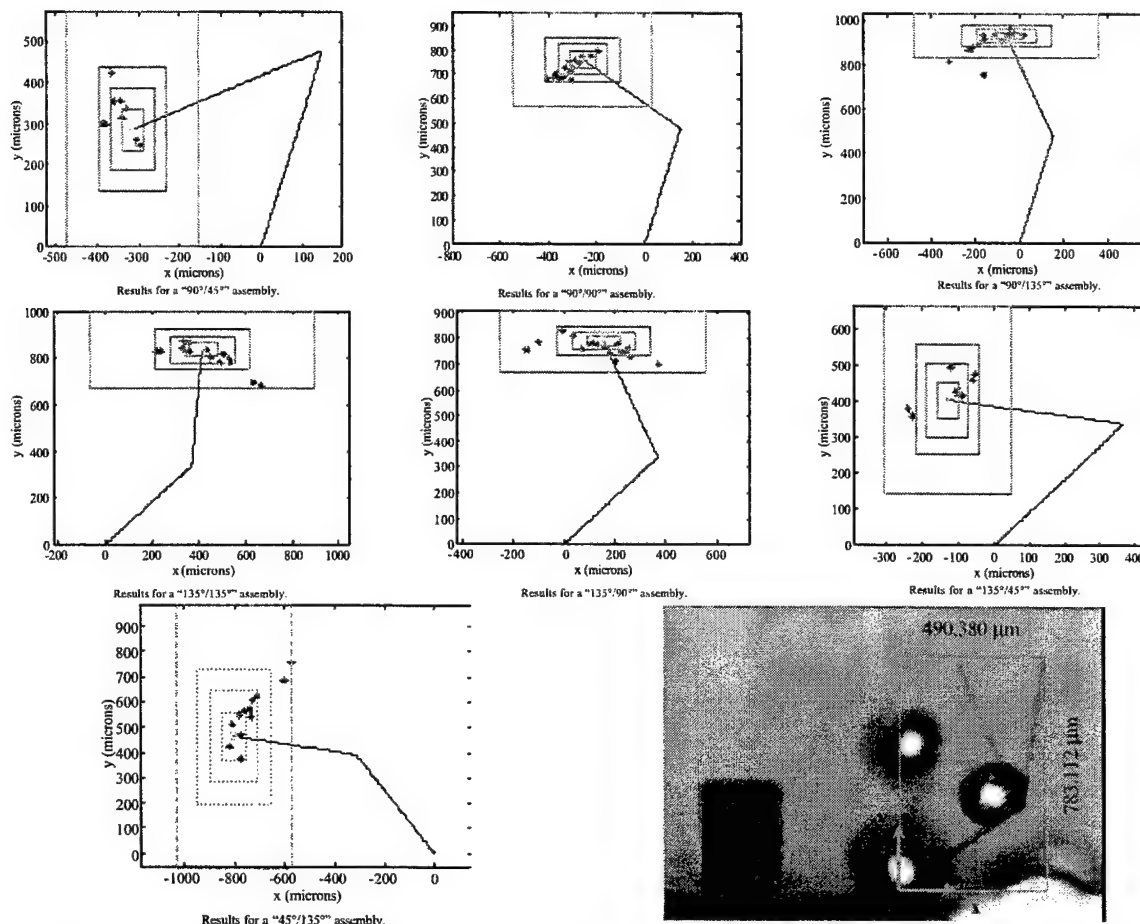


Figure T5-17: Plots of sample endpoint measurements versus the desired position for the seven two-plate angle combinations. Lower right: sample photo measurement of a typical 135/135 device.

Solder deposition and metallurgical considerations raise the following questions: how will the solder behave at a very small scale, and will it be acceptable for MEMS self-assembly? A test was performed to gauge the minimum size in which surface tension still dictates the shape of molten solder, barring metallurgical interactions. A 1000-angstrom layer of pure indium was deposited onto a non-wetting silicon wafer. The indium was then reflowed in formic acid gas atmosphere to remove and prevent oxidation. Figure T5-18 shows that nanometer scale solder spheres were very well formed. In order to see the smallest of the solder spheres, it was necessary to use an atomic force microscope (AFM). Using the AFM, we were able to identify solder spheres as small as 5 nm in diameter. This gives an indication that, barring metallurgical interactions, surface tension is a reliable way to assemble MEMS, and that the surface energy model is still valid at nano-scale.

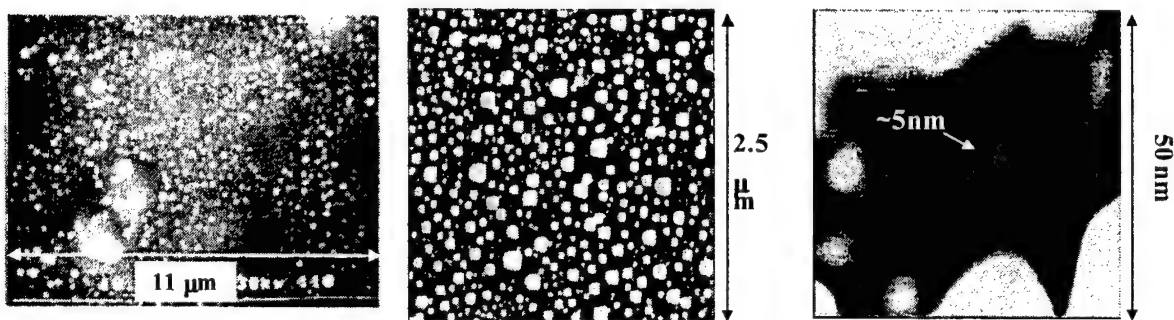


Figure T5-18: Solder nano-spheres formed by surface tension. Left: SEM of a field of indium micro and nano scale spheres. Middle: Atomic force microscope plot of a field of nano-spheres.

Other considerations in MEMS assembly size reduction are: can the solder be manufactured smaller, can it be deposited, and how well can the solder volume be controlled? These questions can be resolved by implementing a thin film solder deposition system for deposition directly onto the MEMS.

A more difficult issue is metallurgical limitations. For example, molten lead/tin solder will absorb gold, which changes the material properties of the solder, as shown in Figure T5-19. For larger assemblies, the amount of gold on the pads is small enough to not change the material properties of the solder significantly. For smaller solder volumes this is not the case, the solder no longer behaves in an easily predictable way, as shown with the indium on gold pads in Figure T3-3 and Figure T5-20. Due to its desirable melting temperature and wetting properties, the predominant material deposited for solder self-assembly is indium. Unfortunately the indium-gold inter-metallic formation rate is very fast. At room temperature the growth rate is in the range of microns per hour. This means that extensive growth has occurred even before the devices are removed from the deposition chamber. For the indium-gold system, the vastly predominant inter-metallic formed is AuIn_2 . AuIn_2 is brittle, has a high melting temperature (457 °C), and has material thermal expansion properties vastly different than those of indium or gold.

Although some research has been done on the inter-metallics commonly encountered in this project, there is very limited data available on the diffusion rates and inter-metallic growth rates. For that reason, we studied the existing theory by experimentally analyzing the inter-metallic growth patterns in the MEMS solder self-assembly systems. One such experiment is shown in Figure T5-21. Gold disks ranging in diameter from 2 to 50 μm were coated with an equal amount of indium and reflowed. The arrangements with a gold weight percentage larger than ~30 % showed no spherical reflow formation (marked 50 and 45 in Figure T5-20), indicating complete formation of AuIn_2 . The arrangements with a gold percentage less than ~10 % (marked 20 and 15 in Figure T5-20) showed complete spherical formation.



Figure T5-19: Consumption of 10 μm gold lines by an 8 mil Sn/Pb solder joint.

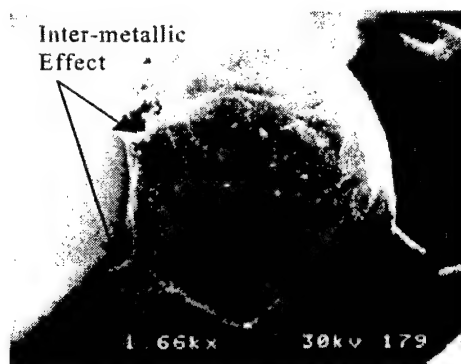


Figure T5-20: Inter-metallic effects on a solder sphere approximately 25 μm in diameter. The indium solder was deposited on 0.5 μm of gold fabricated through MUMPs.

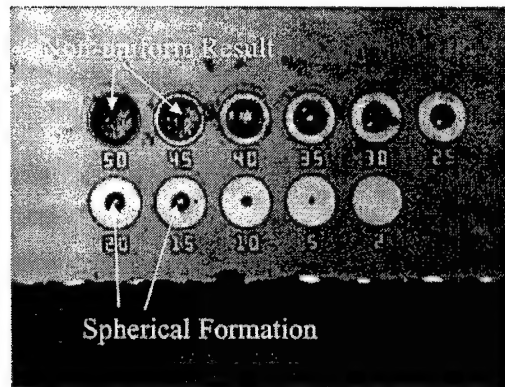


Figure T5-21: Picture of reflowed indium on different sized gold disks.

Another major intermetallic system studied was the lead-tin-gold reaction. This particular reaction is very well understood, as tin-lead (Pb-Sn) solders are among the most common solders used in industry. In the tin-lead-gold reaction gold is readily adsorbed and de-wetting from the pad may occur. While the room temperature diffusion may have long term effects, it should not greatly effect self-assembly. Conversely, the molten rate of consumption is crucial to good self-assembly. If all of the gold is consumed before final assembly, the solder will de-wet and the final solder shape will no longer be what was intended. Although the reaction has been studied thoroughly in industry, there are no concrete numbers that can be applied to solder self-assembled structures. While the studies speak in generalities, data specific to our particular system was needed to gauge and potentially control the de-wetting effect when using Pb-Sn solders. To do this a simple experiment was performed. Four and eight mil 63% SN 27%Pb solder spheres were placed on self-assembly structure pads identical to those used for actual devices. The various samples were then heated and analyzed.

Figure T5-22 shows the results of this study. From both sets of experiments it was concluded that, when the solder wet completely, the solder would remain wet for at least the first 17-25 seconds. After that the corners of the square pads begin to de-wet and pull away from the substrate. After two minutes, the solder has completely de-wet from the pads. A few more points should be noted about this data. This temperature cycle and solder were chosen to reflect what is commonly used for solder self-assembly. Other temperature ranges and solders will yield significantly different results. Also, the length of time each solder took to initially wet also varied (within five seconds of each other). The appropriate measure of the best reflow time should be from time of total wetting to the beginning of dewetting. Because of this, these experiments have some degree of error in the measurements. For this reason, it is concluded that a safe maximum time to allow the solder to stay molten and reflow should be less than ten seconds. Unfortunately, staying under ten seconds of molten time is not easy. In addition to the factor stated above, the rate at which the stage heats and cools will directly effect the time in which the solder remains liquidus. Controlling the temperature that precisely is difficult. To effectively use tin-lead solders for MEMS self-assembly, an ultra-fast heating system should be used.

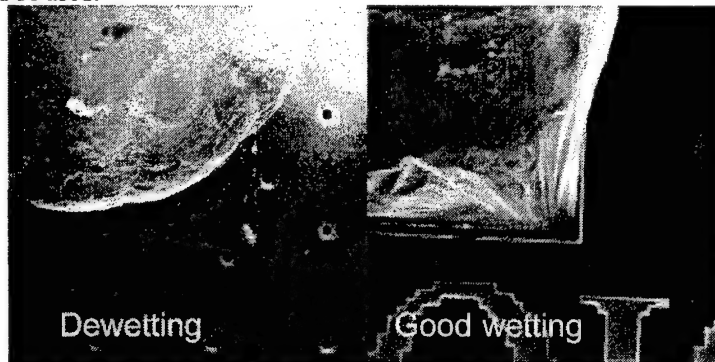


Figure T5-22: Left: Total dewetting of pad (1 minute). Right: Total wetting of pad (10 seconds).

Intermetallic reaction is an extremely complex and varied problem. Often complicating the situation is the chemical reaction that may additionally occur due to the necessary use of flux to remove metal oxide. An example is a black reactant that can occur in the area surrounding and indium solder being reflowed in formic acid vapor flux. Under the right conditions, this black reactant can coat adjacent MEMS structures. This reaction is a particular result of the combination of formic acid molecules and indium oxide, but is representative of a very common set of problems that arise when using chemical fluxes. To avoid these problems, one must use a truly fluxless soldering system. We developed a prototype of such a system, based on ultra-low vacuum removal of oxide. The system is based on the theory that if the partial pressure of oxygen is low enough, the Gibb's free energy of the oxidation reaction will change such that the oxygen will diffuse off of the metal surface, therefore omitting the need for flux. Figure T5-23 is a diagram of our vacuum soldering system. The soldered MEMS are placed inside a temperature controlled vacuum chamber that is itself enclosed in a chamber filled with nitrogen gas. The nitrogen is included because, at the very low pressure we are dealing with, it is near impossible to prevent some leaking. The nitrogen assures that, whatever leaking does occur, it will be nitrogen that leaks in, and will therefore not change the partial pressure of the oxygen. Successful reflow of both indium and tin lead solder has been demonstrated with this setup. But at this point little is known about the varied properties of the solder oxide we encounter. Future work must focus on quantifying these properties and to improve the system for MEMS solder self-assembly in a vacuum.

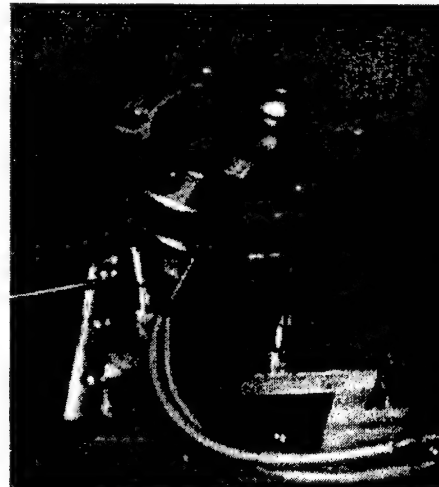
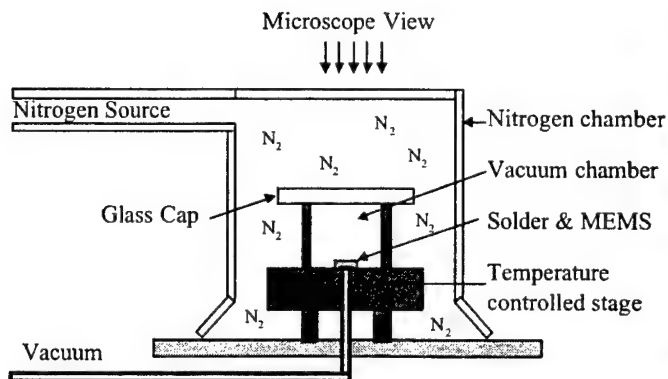


Figure T5-23: Diagram and photograph of fluxless vacuum soldering system.

Various methods currently exist in industry for placing solder on electronic parts, including the automated pick and placement of manufactured solder spheres, molten solder droplet printing – similar to inkjet printing, solder paste printing, evaporation and patterning of solder metals, and electroplating of solder metals. In our research facilities we apply solder by either manual pick and placement of individual manufactured solder spheres ranging in size from 2 to 16 mil or by evaporation and photolithographic patterning of pure indium. Solder can be applied and processed on the MEMS chips/wafers before or after oxide release, depending on which is more convenient for the application. Figure T5-24 depicts the pick and placement method of a solder sphere and an example of patterned indium before reflow.

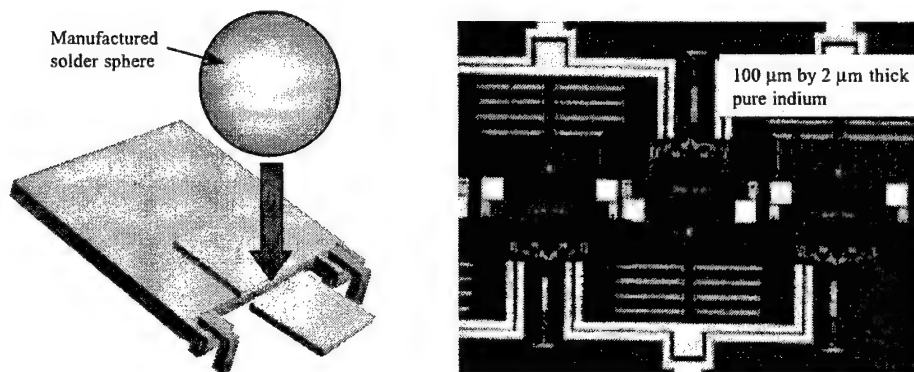


Figure T5-24: Depiction of the pick and placement method of a solder sphere and an example of patterned indium before reflow.

One possible way to eliminate the inter-metallic formation is to use non-solder materials in surface tension based self-assembly. Figure T5-25 shows an example of a polysilicon hinged plate that has been assembled, to 90° with respect to the substrate, using AZP4620 photoresist.

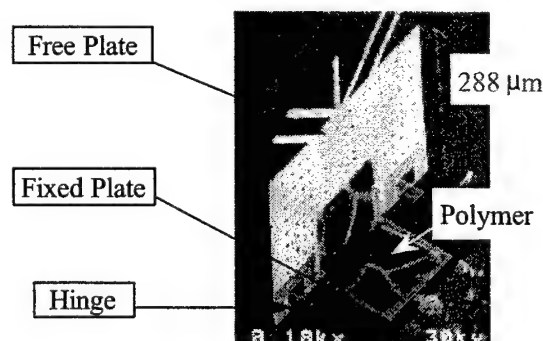


Figure T5-25: Example of a hinged polysilicon plate assembled to 90° with respect to the substrate using AZP4620 photoresist.

AZP4620 is a positive novolak resin based photoresist. The resist shown in Figure T5-25 was first applied to an unreleased MEMS chip and then patterned and developed using normal processing conditions, where soft baking does not exceed 110 °C. Subsequently, the chip was released and reheated on a hotplate in air up to 160 °C whereupon the resist shrinks and pulls up the plate over a period of approximately 5 minutes. The temperature was reduced once the free plate reached an angle of 90°. Any positive photoresist should exhibit this type of surface tension and shrinking behavior. For AZP4620, there are three mechanisms that cause the shrinking, and these are as follows. For temperatures above 120 °C, the remaining PGMEA solvent evaporates out of the resist and the DNQ begins to decompose, causing some shrinkage. Furthermore, for temperatures above 125 °C, the three diazo-groups, in the DNQ, begin crosslinking with the novolak resin, resulting in the tripling of the molecular weight, causing shrinking. Finally, for temperatures above 150 °C, the novolak resin begins crosslinking with itself, also contributing to the shrinkage. Simultaneously, surface tension forces are competing with the curing action (shrinking) causing a relatively slow assembly.

We have also used the pure shrinkage of 200 μm diameter, uncrosslinked, polystyrene spheres to assemble plates. When heated above 300 °C, the polystyrene can decompose and shrink to at least a quarter of its original size. One thing to keep in mind is that the polymers that we have experimented with are not appreciably selective as to what they stick to. Our observations indicate that the polymers stick equally well to silicon, silicon dioxide, silicon nitride, and gold. Other materials, such as thiol-based polymers, which attach selectively to gold should be investigated in future work.

Task 6: Hybrid Technology

One of the goals of this research was to combine MEMS actuation modes, with solder self-assembly to investigate solder effects, if any. We have combined thermal actuation with solder assembly in the solder self-assembled corner-cube reflectors, with no adverse effects noted.

Another hybrid device is shown in Figure T6-1. A released surface micromachined silicon chip, containing an array of six resistive point heater solder self-assembly devices arranged next to each other, was packaged and wire-bonded to a 14 pin ceramic dual inline package. Volumes of 63Sn/37Pb solder, each equivalent to an 8mil diameter solder sphere, were deposited across the gold pads of the hinged plate arrangement, fabricated over the resistive heater. Power (713 mW) was applied to the resistive heater causing the solder to melt, wet the gold pads, and assemble the surface micromachined plate.

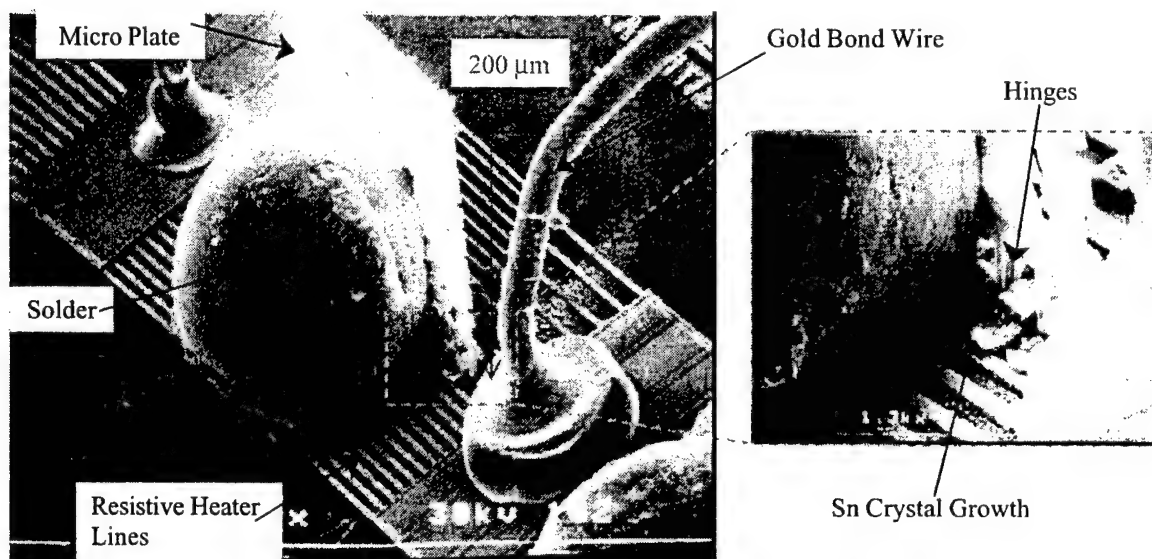


Figure T6-1: Solder self-assembled plate heated to solder melting point using integrated polysilicon resistive heater lines.

We have also combined gold-on-polysilicon bi-morph cantilevers with solder assembly as shown in Figure T6-2. A gold covered polysilicon cantilever is used to connect and mechanically isolate the solder assembly plates from a gold mirror. Because of the nature of this type of mechanical isolation, the cantilever was covered with gold in order to cause the cantilever to curl upwards, thereby, pulling the two connected plates up a little to initiate assembly in the proper direction and reducing the chance of mechanical jamming during assembly.

Finally, the solder assembled switch is an example of electrostatic actuation combined with solder assembly. We have also demonstrated an electrostatic rotary scratch drive motor with solder assembled fins attached to it (Figure T7-9), which is another example of an electrostatic/solder assembly hybrid.

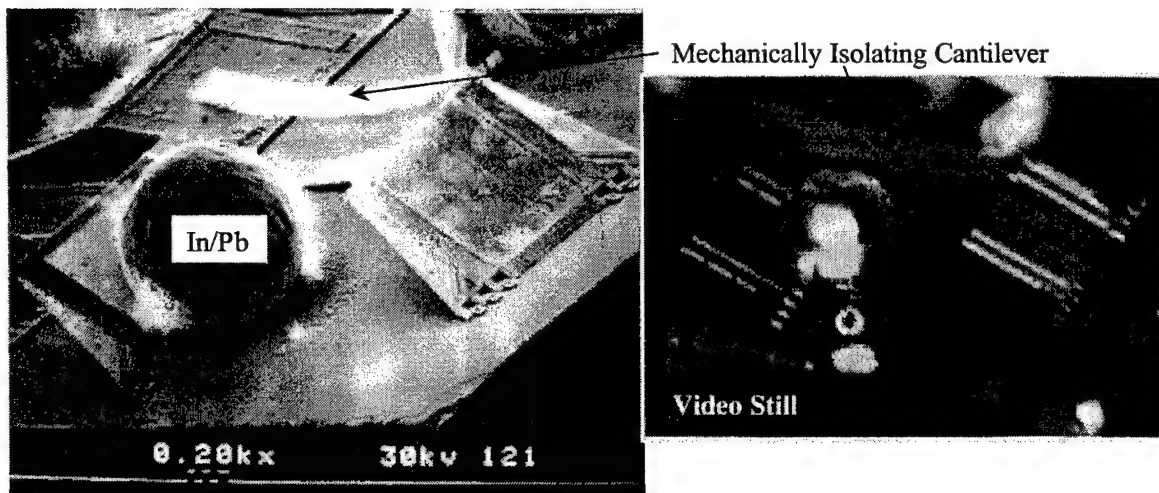


Figure T6-2: Example of gold-on-polysilicon bi-morph cantilevers combined with solder assembly.

Figure T6-3 shows a hybrid device that combines micromirror array with solder assembly. A set of four electrostatic micromirrors is lifted parallel to the substrate to achieve greater angle of rotation. The mirrors rotate ± 10 degrees and require 285 volts to operate. The entire array is approximately 1 mm across, and was assembled using 8 mil diameter tin-lead solder spheres.

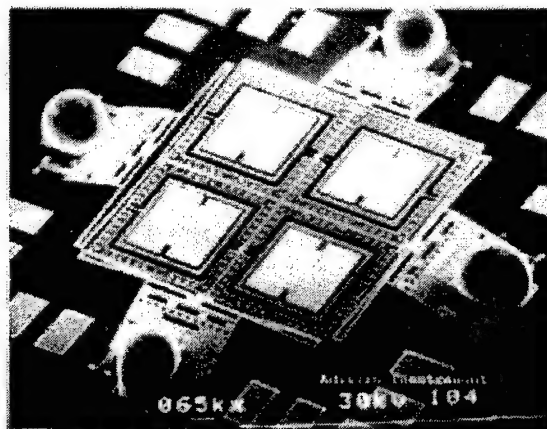


Figure T6-3: Micromirror array combined with solder assembly; micromirrors are lifted parallel to the substrate to achieve greater angle of rotation.

Task 7: Futuristic MEMS

This section summarizes development of other novel MEMS implemented as part of this research. Presented in this section are examples of multi-hinged self-assembled structures that have been demonstrated.

Figure T7-1 shows a polysilicon box enclosure. The box is $525\text{ }\mu\text{m}$ wide by $525\text{ }\mu\text{m}$ long by $555\text{ }\mu\text{m}$ high. Metalized pads are $125\text{ }\mu\text{m}$ by $125\text{ }\mu\text{m}$. 8 mil diameter, 60%In / 40%Pb, solder spheres were used to assemble the box. Figure T7-2 is a MEMS garage with opening door. The opening door is attached, at its base, to a gear that is driven by a thermal actuator array. Figure T7-3 is a 14 hinged-plate structure that was assembled with three solder balls. Tethers attached to the tops of the front polysilicon plates are used to lift up successive rows of plates.

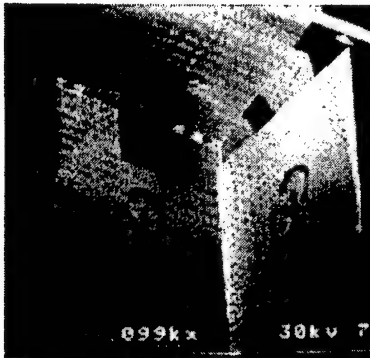


Figure T7-1: SEM of a polysilicon box.

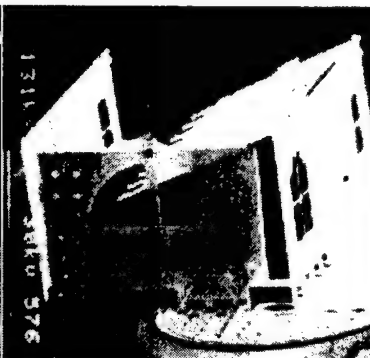


Figure T7-2: A MEMS garage with opening door.

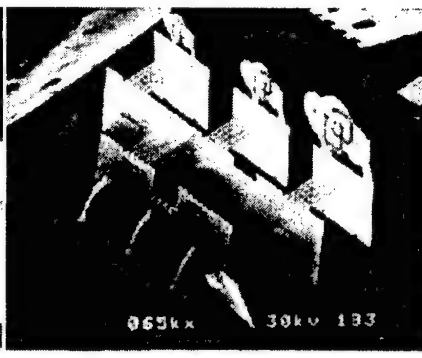


Figure T7-3: A 14 hinged-plate structure.

As Figure T7-3 shows, the concept of linking MEMS is a key in the creation of more complex hinged structures. Figures T7-4 through T7-6 demonstrate this concept further. Figure T7-4 illustrates two types of mirrors assembled using solder assembly and linkages. Each mirror was assembled using 8 mil diameter 63Sn/37Pb solder sphere. In these cases, the benefit of separating the mirror from the solder via linkages allows for movement of the mirror section via external actuation. Figure T7-5 is a photograph of five plates attached end-to-end and assembled using five independent 8mil diameter solder spheres to create a hook or arch. The device was designed to demonstrate the complexity that is achievable with linked solder self-assembly. Each plate is 400 μm wide and 450 μm long, and the entire structure stands approximately 750 μm tall.

Figure T7-6 shows a design of a linked multi-plate solder-assembly fiber-optic gripper/aligner. The device is designed such that when the solder rotates the series of linked plates, the motion will accurately pull and lock a single optical fiber into a specified position. The devices in Figure T7-6 were assembled using 8 mil diameter 63Sn/37Pb solder spheres. Figure T7-7 is a design of a solder assembled antenna. The device is 100 μm wide by 10,000 μm high.

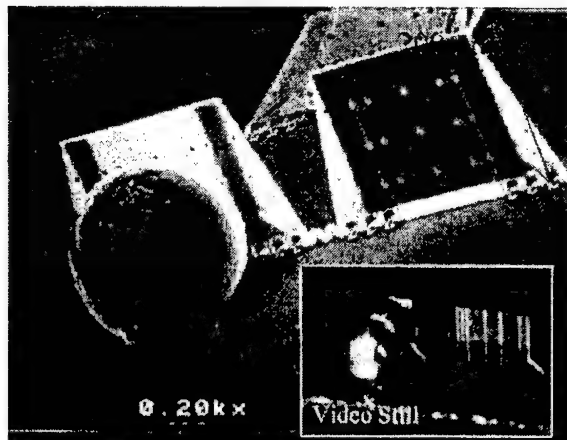


Figure T7-4: Mirrors assembled using solder self-assembly but attached via linkages to allow for external actuation methods.

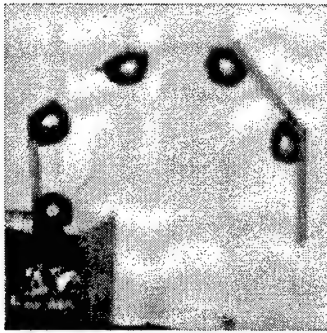


Figure T7-5: Five-plate hook mechanism. Each plate is 400x450 μm .



Figure T7-6: Linked-plate solder-assembled fiber grippers grasping a 200 micron diameter optical fiber.

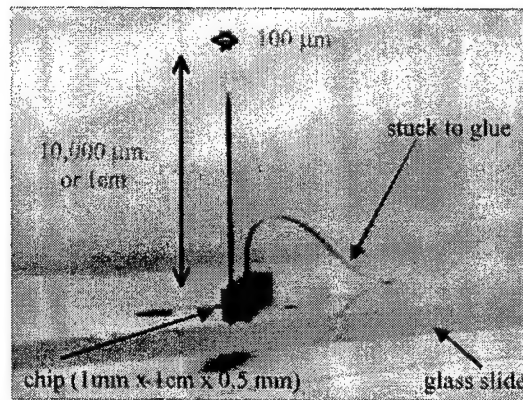
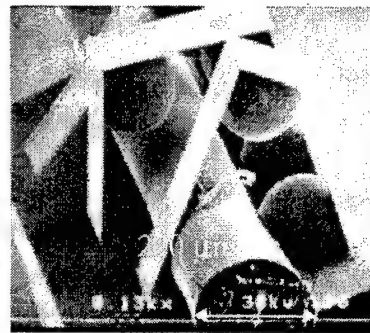


Figure T7-7: Solder assembled antenna. Device stands 1 cm tall and is 100 μm wide and 2 μm thick. It was assembled using a single 8-mil diameter, 63% Sn / 37% Pb, solder sphere.

Through the combination of several key technologies, we have demonstrated a solder self-assembled, surface micro-machined axial flow fan powered by a scratch drive actuator (SDA) rotary motor (Figure T7-8). This micro axial flow fan has the potential for integration into chip cooling systems, chemical and biological gas sensors, micro combustion mixing chambers, turbine systems, and a propulsion system for a micro-vehicle. Not only is the range of MEMS applications broadened by this invention, but the usefulness of some existing MEMS components can now be enhanced. For example, rotor-stator (wobble or toothed) electrostatic motors can be outfitted with solder assembled blades, transforming them into useful fluid propulsion devices instead of purely laboratory demonstrations. The possibilities continue with blades mounted on comb drives.

The axial flow fan is driven using a rotary SDA array made from nine individual SDA with a continuous sliding contact around the perimeter. Rotary SDA motors have been previously evaluated in the literature for output torque and optimized SDA design, yet our research work represents the first demonstrated application of such a motor. Each of the eight fan blades was assembled using 63Sn/37Pb solder with volume equivalent to a 4 mil diameter sphere, as shown in Figure T7-9.

A sample size of 27 blade angles was measured by capturing a side profile of each blade on a video image. The angles were calculated from the pixel distances in the captured video images, and the distribution of the assembly angles was estimated to be $\mu_{\text{angle}} = 107.24^\circ$ and $\sigma_{\text{angle}} = 7.95^\circ$. The SDA design and drive signal have been optimized and are capable of driving the fan at speeds over 180 RPM in an ambient air environment. The frequency of the drive signal and magnitude of the driving voltage control the rotational speed of the fan, as well as the direction of operation. Frequencies from 1 to 12 kHz were used to drive the fan with a 50 V zero-to-peak sinusoidal drive signal offset by 75 V DC.

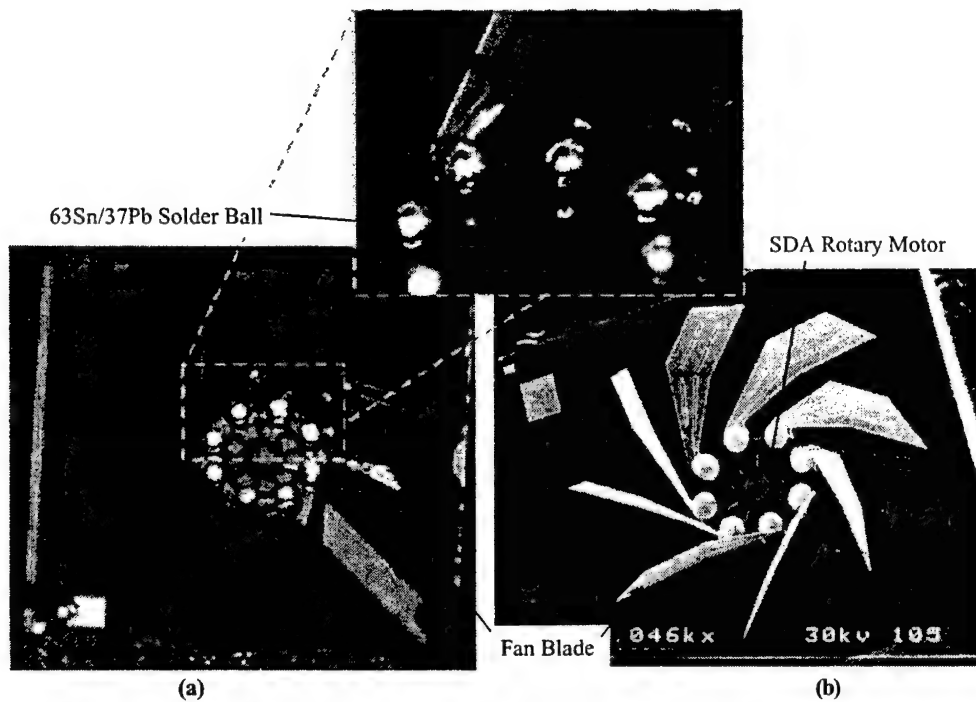


Figure T7-8: (a) Captured video image of the micro axial flow fan during operational testing with exploded view of 4 of the solder joints used to assemble the fan blades. (b) Scanning electron micrograph of a micro axial flow fan.

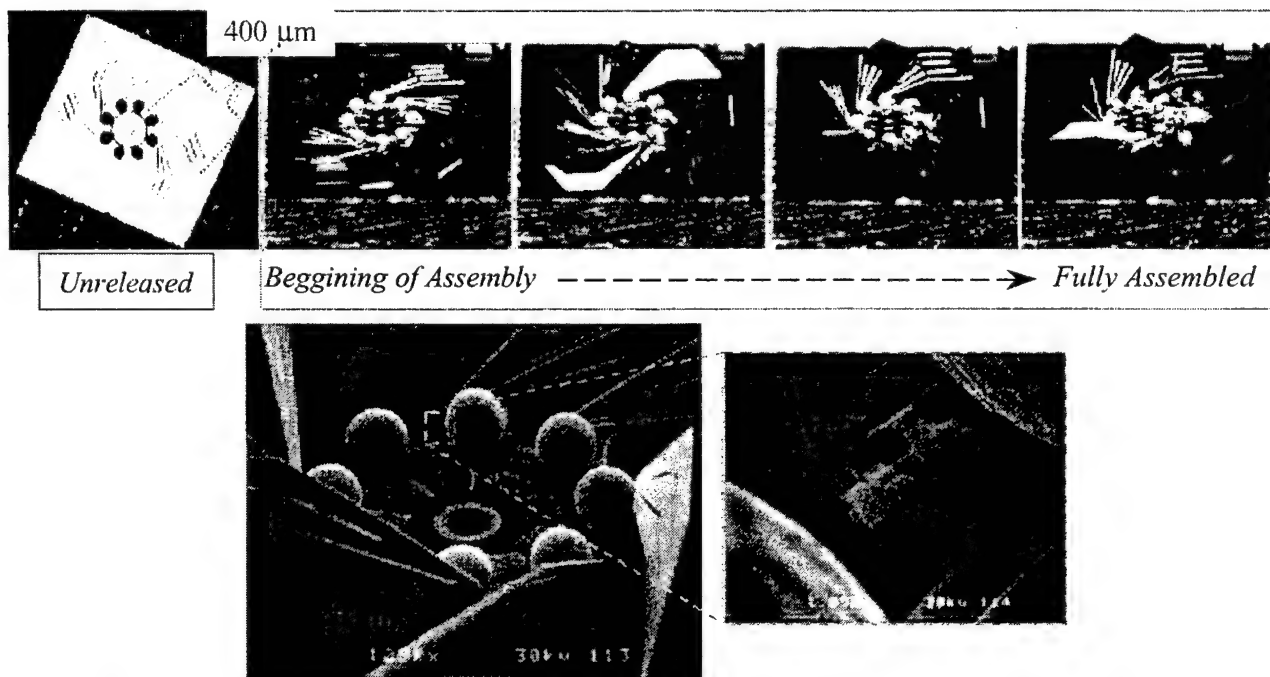


Figure T7-9: The top shows captured video images of an unreleased micro axial flow fan and the assembly sequence, after release, while solder is assembling the fan blades during heating on a hot plate. The bottom is a SEM showing the SDA rotary motor and solder joints with an exploded view of the fan blade hinges.

Task 8: Quality and Reliability

8.1 Introduction

It is widely recognized that warpage occurs in multilayer MEMS structures due to thermal expansion mismatch between the materials. Figure T8-1-1 (a) shows a gold/polysilicon plate that bends about $20\text{ }\mu\text{m}$ from the substrate. In Figure T8-1-1 (b), a gross cylindrical curvature of a capacitive plate that has been flip-chip transferred to another substrate is seen.

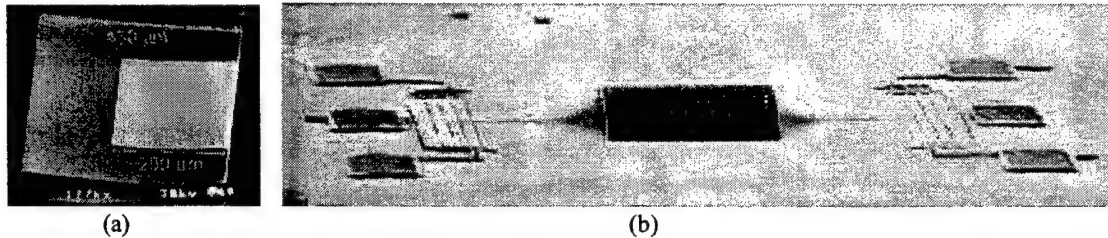


Figure T8-1-1: (a) SEM photo of gold/polysilicon plate (MUMPS 28) that bends upward from the substrate. (b) Capacitive plate (gold/polysilicon) on a transferred MEMS structure is substantially warped due to residual stresses.

Figure T8-1-2 shows a measurement of the deformation of a plate after it has been assembled (lifted to 90° off the substrate) using an 8 mil solder ball. The image is taken from the backside of the assembled plate and so the solder ball is hidden from view. The deformation due to the solder self-assembly force is evident. In this case, the observed peak-to-valley displacements across the plate are $3.7\text{ }\mu\text{m}$.

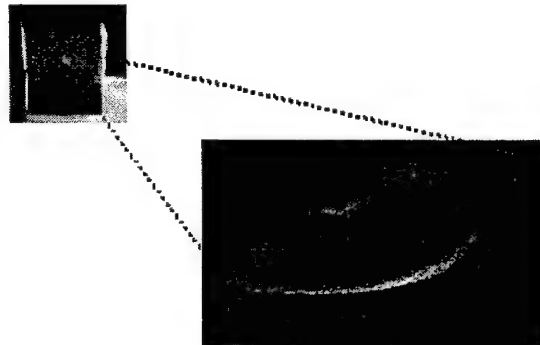


Figure T8-1-2: Deformation of a $500\text{ }\mu\text{m} \times 420\text{ }\mu\text{m}$, $2\text{ }\mu\text{m}$ thick polysilicon plate with a $0.5\text{ }\mu\text{m}$ thick $125 \times 125\text{ }\mu\text{m}$ gold pad. The plate was assembled with an 8 mil solder ball located underneath the plate.

This section summarizes our work on quality and reliability of developed MEMS. There are two principal deformation modes that we studied: i) deformation of multi-layer plate structures due to thermal expansion mismatch between individual layer materials (e.g. polysilicon and gold) after release, but before solder self-assembly; and ii) deformation of such plates after they have been assembled using solder. The experimental efforts consisted of full-field measurements of deformation over the entire surface of plates both before and after assembly. These measurements were made with an interferometric microscope. The modeling efforts consisted of the development of idealized models of multilayer plate structures before assembly, that consider the temperature dependence of material properties (stiffness and thermal expansion). Both elastic and elastic-plastic constitutive behavior is included.

8.2 Experiment capabilities

We measure full field deformed shapes using a scanning white light interferometric microscope, which is shown in Figure T8-2-1 (a). Figure T8-2-1 (b) shows the optical configuration of the interferometric microscope.

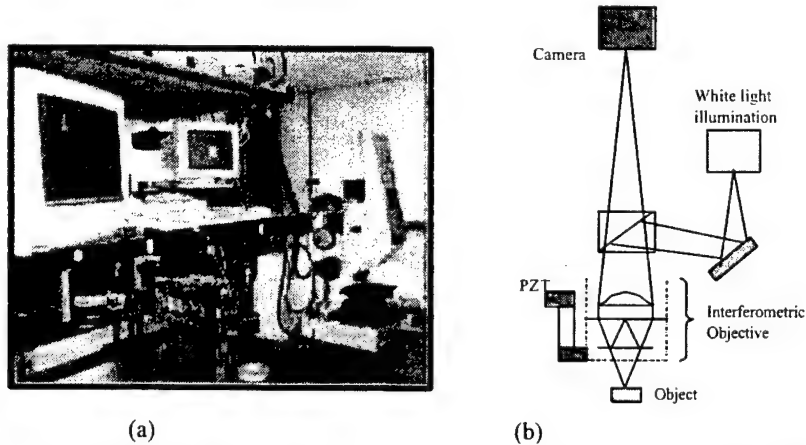


Figure T8-2-1: (a) Scanning white light interferometric microscope that is used to measure the full field deformed shapes; (b) optical drawing of the interferometric microscope.

A custom-built thermal chamber was designed that can be used together with the interferometric microscope, which allows to measure the deformation at elevated temperatures. Figure T8-2-2 shows the setup used to measure deformation at elevated temperatures.

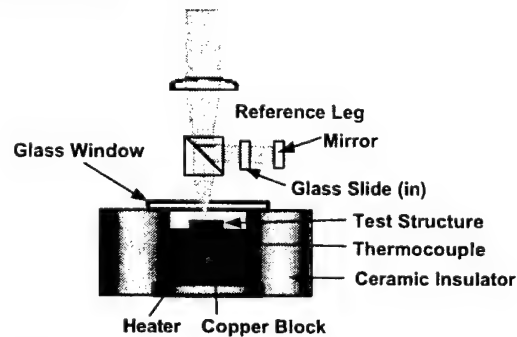


Figure T8-2-2: Setup for measuring plate deformation at various temperatures.

Ultra-low load indentation can measure the mechanical properties of materials at very small scales. The instrumented microindenter shown in Figure T8-2-3 employs high-resolution sensors and actuators that can continuously control and monitor the loads and displacements on an indenter as it is driven into and withdrawn from a material. Many material properties can be determined by analyses of the indentation load-displacement data.



Figure T8-2-3: Instrumented microindenter.

8.3 Linear and geometrically nonlinear behavior of gold/polysilicon fully covered plate microstructures subjected to thermal loading

An inherent characteristic of multilayer material structures is that misfit strains between the layers (for example, due to intrinsic processing stresses or thermal expansion mismatch between the materials upon a temperature change) lead to stresses in the layers and deformation of the structure. Curvature measurements are routinely used, e.g. in the microelectronics industry, to determine stress states in metal films deposited on a substrate. Their attractiveness is based on the fact that wafer curvature can be easily and accurately measured, and through use of the Stoney (1909) formula (based on small-deformation, linear elastic considerations), the measured curvature can be directly related to the film stress (which is typically biaxial and spatially uniform) without knowledge of the source of the stress or even the thermoelastic properties of the film. Much of the understanding regarding deformation of multilayers that has come from microelectronics applications is applicable to many MEMS applications, but significant differences exist and must be well understood to optimize the design of reliable MEMS. These include:

- In MEMS applications, the thicknesses of the layers are small (on the order of μm) and usually comparable. This leads to much larger deflections, relative to the thickness of structures, than are observed in microelectronics applications. For example, the maximum deflection of a $0.5\ \mu\text{m}$ gold film on a $500\ \mu\text{m}$ thick $100\ \text{mm}$ diameter silicon substrate subjected to a 100°C temperature change is about two percent of the thickness. These values are not unrealistic for microelectronics applications. For MEMS applications, a reasonable example is a $0.5\ \mu\text{m}$ gold film on a $1.5\ \mu\text{m}$ thick $400\ \mu\text{m}$ diameter polysilicon plate. For this case, when subjected to a 100°C temperature change, the maximum deflection is about six times the thickness.
- This can make it necessary to include geometric nonlinearity in order to accurately model deformation. Furthermore, the geometric nonlinearity can lead to bifurcations in the deformation behavior. These can be detrimental when dimensional stability is a requirement, or can be beneficial for actuator applications.
- Since the layers are of comparable thicknesses, stresses can vary appreciably through the thickness of the layers; the average stress in the layer may not be suitable to characterize film stresses as it is in many microelectronics applications.
- Tradeoffs between stress and curvature exist; for a given metal film thickness, decreasing the polysilicon thickness can reduce the stress in the metal, but at the expense of increasing the curvature, as shown in Figure T8-3-1. The significance of this is obvious as many MEMS applications have strict deformation requirements, perhaps more severe than stress requirements.
- The curvature, and thus stresses, may vary significantly over the in-plane dimensions of the structure; thus, the average curvature may be insufficient to adequately describe the deformation state of the structure.
- The patterning geometry of metal films on polysilicon (or other materials) may be arbitrary, as opposed to fully blanketed or thin line patterns. This can result in complex spatially nonuniform deformation states.

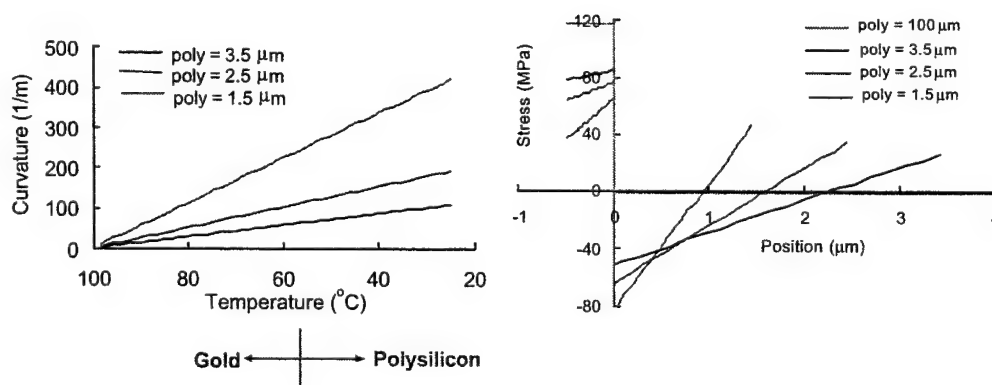


Figure T8-3-1: (a) Curvature study for fixed thickness of gold. (b) Stress across the thickness for fixed thickness of gold.

In this research we studied, via measurements and analysis, the deformation behavior of a series of square and circular gold/polysilicon plate microstructures fabricated by the MUMPs surface micromachining process and

subjected to uniform temperature changes which generate internal stress and deformation via thermal expansion mismatch of the gold and polysilicon. Linear and geometrically nonlinear deformations were observed, as well bifurcations in the equilibrium deformed shapes.

We designed a series of square and circular gold/polysilicon plate microstructures and fabricated them using MUMPS. The square and circular samples were implemented using the MUMPS 31 and 36 fabrication runs, respectively. In the series of microstructures, the polysilicon layer was fully covered by the gold layer, except for a couple of microns around the perimeter. We varied the square side length L and circle diameter D to include $L, D = 150 \mu\text{m}, 200 \mu\text{m}, 250 \mu\text{m}, \text{ and } 300 \mu\text{m}$, keeping the thickness of the gold and polysilicon fixed at nominal values of $0.5 \mu\text{m}$ and $1.5 \mu\text{m}$, respectively, as produced by the MUMPS process. The idea behind the design of the microstructures was to yield a gold/polysilicon bilayer structure that rests as freely as possible. To this end, the plates were supported on the substrate by a $16 \mu\text{m}$ diameter polysilicon post. SEMs of typical plate microstructures are shown in Fig. T8-3-2.

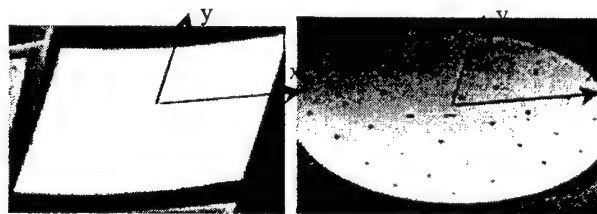


Figure T8-3-2: SEM of $L, D = 300 \mu\text{m}$ gold/polysilicon plate structures. The support post and etch holes are apparent and the x-y coordinate system used in subsequent measurements and analysis is identified.

We measured the full-field deformation of the plate structures as a function of temperature change using an interferometric microscope and a custom-built thermal chamber that is covered by a quartz window to allow optical access. The resolution of the out-of-plane displacement measurement, $w(x,y)$, is 0.1 nm ; the resolution of the temperature chamber is 1°C . The specific test protocol consisted of the following:

- Heat the sample to approximately 100°C where it is flat and thus presumably stress free. The sample is held at this temperature for a time period sufficient to ensure it has reached thermal equilibrium and a stable flat shape (≈ 3.5 minutes).
- The sample is then slowly cooled to room temperature. The temperature is held constant for ≈ 3.5 minutes roughly every 5°C so that thermal equilibrium is reached. Full-field out-of-plane displacements $w(x,y)$ are then measured over the entire surface of the plate. This data is stored for subsequent analysis.
- From the measured $w(x,y)$, we calculated the curvatures $\kappa_x(x,y) \approx -\partial^2 w / \partial x^2$ and $\kappa_y(x,y) \approx -\partial^2 w / \partial y^2$.

These are computed by fitting $w(x,y)$ with a 6th-order polynomial in x and y (which was sufficient to accurately describe the displacement profile in all cases) and then differentiating this function.

For each sample at least three replicas were tested and excellent repeatability resulted.

While an analytical model can be developed to model the deformation of two-layer plate structures, the simplest approach to tackle more general deformation problems is to use the finite element method to solve the geometrically nonlinear equations over an arbitrary spatial domain. This is also the most viable approach for complicated geometries. We used the ABAQUS finite element code with composite shell elements to approximate the thin-plate kinematics of the Kirchhoff theory. Both polysilicon and gold were modeled as linear elastic with isotropic material properties. Input parameters to the finite element calculations were $E_p = 163 \text{ GPa}$, $\nu_p = 0.22$, $E_g = 78 \text{ GPa}$, $\nu_g = 0.42$. The thermal expansion coefficients of the materials were assumed to vary linearly with temperature and values at $100(23)^\circ\text{C}$ used were $\alpha_p = 3.1(2.6) \times 10^{-6}/^\circ\text{C}$, and $\alpha_g = 14.6(14.2) \times 10^{-6}/^\circ\text{C}$. Here and throughout the subscripts p and g denote polysilicon and gold, respectively. Calculations were carried out to model the effect of the support post and it was found to be insignificant on the resulting displacements, curvatures, and stresses except in a region very near the post. If one carries out calculations as just described, the linear and geometrically nonlinear response of the plate can be computed, but the bifurcations, and the subsequent post-buckling behavior, can not because of the perfect

symmetry present in the geometry and material behavior. In order to model the bifurcations, one must seed an imperfection into the model. We did this in two ways, with the hope of identifying the likely actual imperfections that contribute to the observed behavior. First, we introduced a slight thermal expansion mismatch anisotropy into the model by assuming the thermal expansion coefficient of the gold is orthotropic. Specifically, we defined the in-plane thermal expansion coefficients to be $\alpha_x = \alpha_g$ and $\alpha_y = \alpha_g + \delta\alpha$, where $\delta\alpha$ was taken to be 0.01% of α_g . With this slight perturbation, the pre-bifurcation response was indistinguishable from that with the isotropic thermal expansion. The second approach to seed the imperfection was only used for the square plates; we defined one side of the plate to be slightly larger than the other, i.e., the plate has dimensions $L \times (L + \Delta L)$. Details of the bifurcation, e.g., its sharpness, are strongly influenced by small changes in the imperfection. We discuss this later in light of both our measurements and predictions. Calculations were carried out for the loading situation of an applied uniform temperature change consistent with that experienced in the measurements.

Figures T8-3-3 and T8-3-4 show contour plots of the measured and predicted displacement $w(x,y)$ at room temperature for all square and circular plates. Each contour band diagram represents a displacement of 0.23 μm , 0.35 μm , 0.45 μm , and 0.6 μm for $L = 150 \mu\text{m}$, 200 μm , 250 μm , and 300 μm ; and a displacement of 0.11, 0.24, 0.37, and 0.43 μm for the $D = 150, 200, 250$, and 300 μm plates, respectively. Due to the thermal expansion mismatch between the polysilicon and gold, the $L, D = 150 \mu\text{m}$ sample deforms in a spherically symmetric manner; contours of constant transverse displacement $w(x,y)$ are nearly circles. This is also the case as the size increases to $L, D = 200 \mu\text{m}$ and $L, D = 250 \mu\text{m}$, although the displacements increase as the plate size increases. At $L, D = 300 \mu\text{m}$, though, the transverse displacement contours are more elliptical than circular, indicating that the deformation is no longer spherically symmetric. It is apparent that upon cooling the different sized plates the same amount, there is a size dependence on not only the magnitude but also mode of deformation. As the in-plane dimension of the plate increases with the thickness held constant, the deformation mode changes from one of spherical symmetry to one more like cylindrical symmetry. Both the measured and predicted $w(x,y)$ contours show this same behavior and the agreement between them is quite good. As we will describe later, proper normalization of the curvature and temperature change yields the functional form of this size dependence before bifurcation.

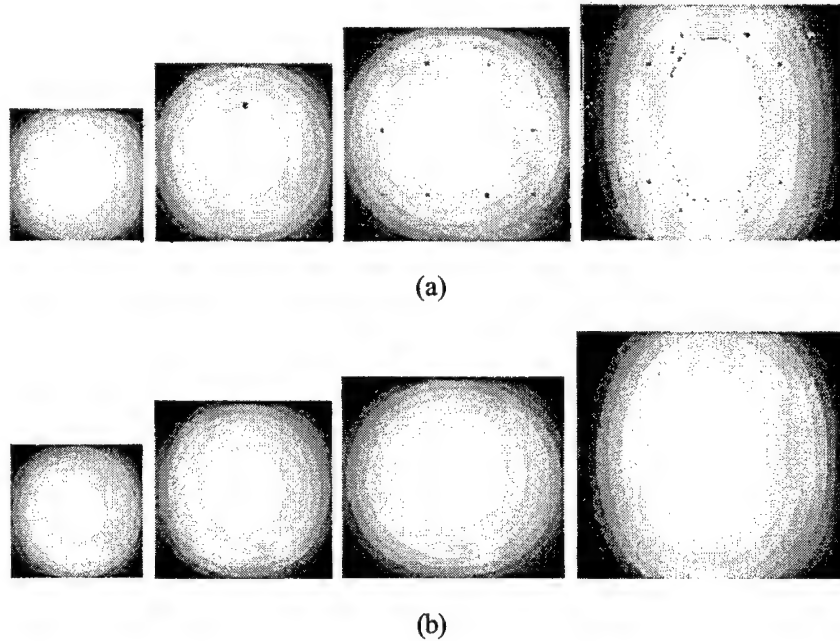


Figure T8-3-3: Transverse displacement contours at room temperature for square gold/polysilicon plate structures ($L = 150, 200, 250$, and $300 \mu\text{m}$ from left to right): (a) measured, and (b) predicted. 10 contours for each contour plot, each contour band diagram represents a displacement of 0.23 μm , 0.35 μm , 0.45 μm , and 0.6 μm for $L = 150 \mu\text{m}$, 200 μm , 250 μm , and 300 μm respectively.

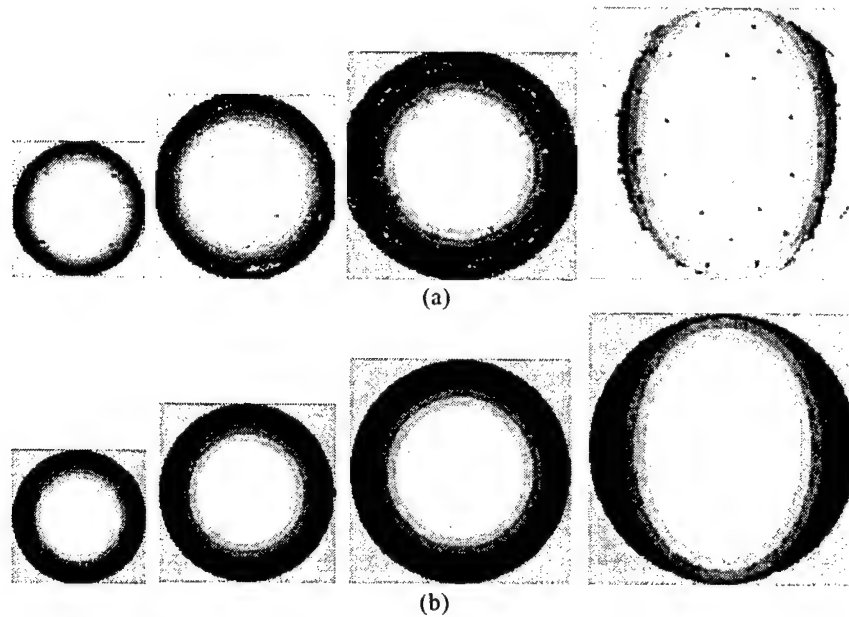


Figure T8-3-4: Transverse displacement contours at room temperature for circular gold/polysilicon plate structures ($D = 150, 200, 250$, and $300 \mu\text{m}$ from left to right): (a) measured, and (b) predicted. 10 contours for each contour plot, each contour band diagram represents a displacement of $0.11 \mu\text{m}$, $0.24 \mu\text{m}$, $0.37 \mu\text{m}$, and $0.43 \mu\text{m}$ for $D = 150 \mu\text{m}$, $200 \mu\text{m}$, $250 \mu\text{m}$, and $300 \mu\text{m}$, respectively.

In Figure T8-3-5 we plot the average curvature in the x - and y -directions as a function of the temperature change during cooling. In these plots, the average curvatures are determined from the measured and computed $w(x,y)$ by averaging $\kappa_x = -\partial^2 w(x,0)/\partial x^2$ and $\kappa_y = -\partial^2 w(0,y)/\partial y^2$ along the paths $y=0$ and $x=0$, respectively, over a length of $150 \mu\text{m}$ from the center of the plate. The x and y -directions are taken to be aligned with the principal curvatures after bifurcation. Before bifurcation, the response is axially symmetric and so the x - and y -directions are arbitrary and indistinguishable. The use of the average curvature as a measure of the plate deformation is obviously quite appropriate if the curvature is (or is close to) spatially uniform. This aspect will be taken up to some degree later. The measurements and predictions in Figure T8-3-5 show that in general three regimes of deformation exist: i) linear thermoelastic response independent of plate size, ii) geometrically nonlinear thermoelastic response that depends on plate size, and iii) bifurcations in the curvature-temperature response that also depend on plate size. By bifurcations we mean that as the temperature changes, the plate develops a nearly axially symmetric curvature with $\kappa = \kappa_y$ which at first increases linearly with the temperature change, and then nonlinearly. At some critical temperature change, the deformation mode changes from axially-symmetric to a mode closer to cylindrical bending where $\kappa_x \neq \kappa_y$; as the temperature change increases beyond this value the difference between κ_x and κ_y increases. In the first two regimes the measured deformations are axially symmetric, while in the third they are strongly nonsymmetric.

Figure T8-3-5 shows good agreement between the measurements and predictions in all three deformation regimes. The major discrepancy is the sharpness of the bifurcation for the $L, D = 300 \mu\text{m}$ plate; it is quite sharp in the predictions but much more gradual in the measurements. To understand this we remind that the source of the bifurcation is an *imperfection* of some sort that breaks the ideal symmetry. In the calculations that imperfection was simulated via the slight anisotropy of the thermal expansion coefficient. In Figure T8-3-6 we explore the effect of the imperfection that triggers the bifurcation on the deformation behavior. In order to simplify the interpretation of the results and identify basic phenomenological features, the calculations in Figure T8-3-6 were carried out with constant room-temperature material properties. This slightly alters the exact magnitudes of calculated quantities, but does not effect the conclusions drawn. In Figure T8-3-6 the thermal expansion coefficient of the gold $\alpha_x = \alpha_g$ and $\alpha_y = \alpha_g + \delta\alpha_g$, we alter the imperfection by increasing $\delta\alpha_g$ while keeping α_g fixed. Figure T8-3-6 shows that increasing $\delta\alpha_g$ from 0.01% of α_g to 1.0% of α_g resulted in a much more gradual bifurcation that initiated about 10°C higher. The details of the bifurcation are strongly influenced by slight perturbations of the imperfection. This sensitivity will probably

preclude a sharp bifurcation in practice. Indeed, the $\delta\alpha$ used here to simulate the imperfection is not an unreasonable measure of the anisotropy that can develop as a result of processing variations. It is, though, probably not easy to measure the thermal expansion anisotropy this accurately with available means. Furthermore, other imperfections such as slight variations in the circular geometry, the etch holes, and anisotropy and/or heterogeneity in other material properties also can play a role in the exact bifurcation details. As a result, the prediction of the bifurcation details is prohibitively difficult because of the strong sensitivity to the imperfection.

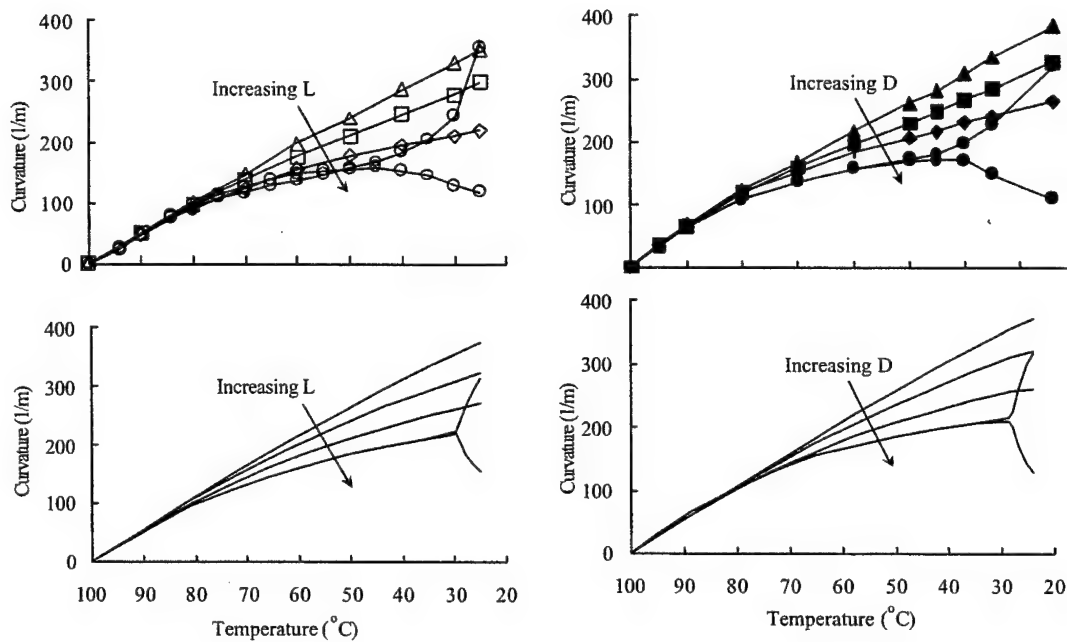


Figure T8-3-5: Average measured (top) and predicted (bottom) curvature as a function of temperature upon cooling from 100°C to room temperature. The curves from top to bottom are for the $L, D = 150, 200, 250$, and $300 \mu\text{m}$ structures, respectively.

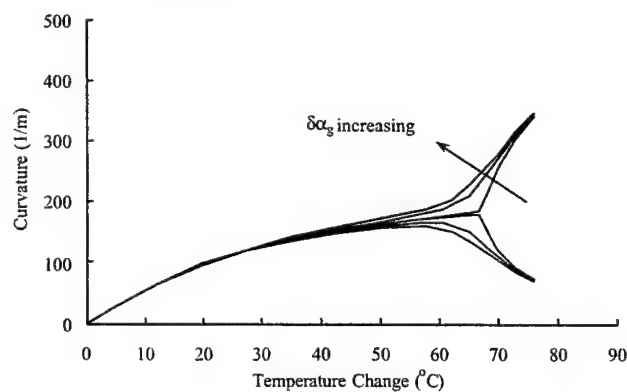


Figure T8-3-6: Average predicted curvature as a function of temperature upon cooling from 100°C to room temperature. $L = 300 \text{ mm}$ square plate: $\delta\alpha_g$ from 0.01% of α_g to 1.0 % of α_g .

We introduce the nondimensional curvature K and mismatch strain S :

$$K = \frac{\kappa \ell^2}{4t_p} \quad S = \frac{3\Delta\alpha\Delta T\ell^2 t_g M_g}{2t_p^3 M_p}$$

In these expressions, $\ell = R$ and $\ell = L/2$ for the circular and square plates, respectively; t_i is the layer thickness, $M_i = E_i/(1-\nu_i)$ for both the polysilicon and gold ($i = p, g$), and $\Delta\alpha = \alpha_p - \alpha_g$. The data of Figure T8-3-4, before bifurcation, are plotted in terms of these nondimensionalized variables in Figure T8-3-7. For plate structures with in-plane dimensions, D or L , much larger than the thickness, the average normalized curvature should be independent of plate size and shape. In fact, in Fig T8-3-7 predictions are shown for both the circular and square plates and they are indistinguishable. The measurements, though, differ slightly, particularly at larger values of S . Here the results for the circular structures are slightly above those for the square structures. The reason for this is unclear, but most likely is due to slight differences in properties between the two fabrication runs to produce the two sets of samples.

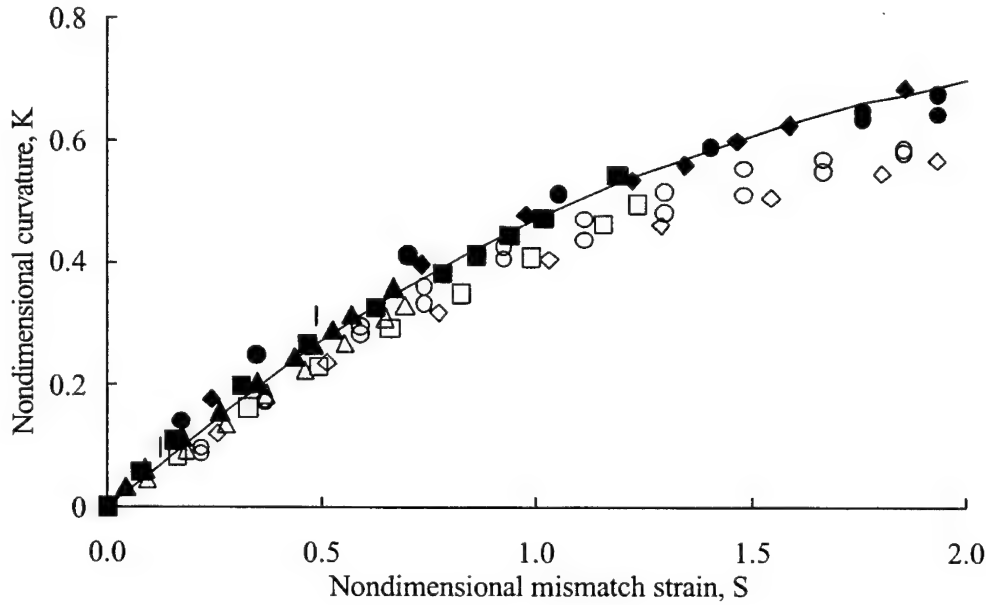


Figure T8-3-7: Nondimensional average curvature as a function of temperature change for the linear and nonlinear regimes. Measurements (open symbols for square structures and filled symbols for circular structures) and the prediction (solid line for square and circular structures).

In Figure T8-3-8 and Figure T8-3-9 we explore the connection between the thermomechanical loading (the temperature change), the geometry (plate size), and the boundaries between the three deformation regimes for the gold/polysilicon plate microstructures. Figure T8-3-8 shows the temperature change necessary to initiate nonlinear effects (the transition between regions *I* and *II*) as a function of polysilicon thickness when the gold film thickness is kept constant at 0.5 μm . Figure T8-3-9 shows similar results for the onset of bifurcation (the transition between regions *II* and *III*). For simplicity, the calculations leading to these results were carried out using an analytical model.

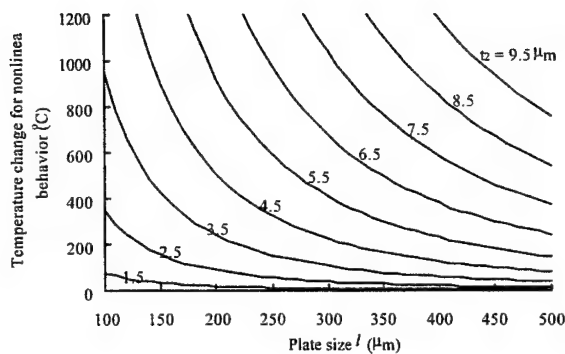


Figure T8-3-8: Temperature change required for the initiation of nonlinear geometry effects as a function of plate size and the thickness of polysilicon for the gold/polysilicon microstructures.

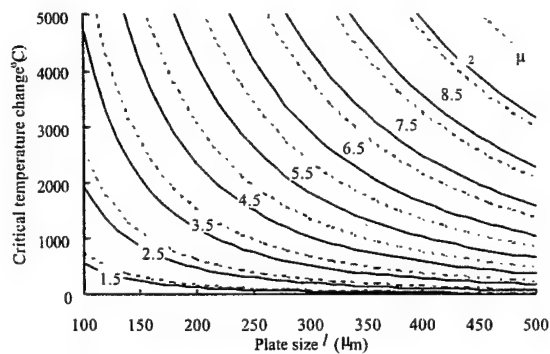


Figure T8-3-9: Critical temperature change for bifurcation as a function of plate size and the thickness of polysilicon for the square and circular gold/polysilicon microstructures.

The FE calculations allow the spatial variation of the curvature. Our full-field measurement allows us to study this experimentally. In Fig. T8-3-10 the curvatures $\kappa(x,y)$ and $\kappa_y(x,y)$ are plotted as a function of temperature change for four points along the x-axis ($y=0$) for the $L = 300 \mu\text{m}$ plate: $2x/L = 0.17, 0.33, 0.50$, and 0.67 . Predictions for these four locations, plus $2x/L = 1$ are also shown in Fig. T8-3-11. In the linear regime, the curves are indistinguishable implying that the curvature is uniform across the plate. In the nonlinear regime, though, the curvature varies appreciably with position, increasing by about a factor of two from the center to the periphery of the plate. Good agreement exists between data and predictions, with the predictions slightly overestimating the curvature in the nonlinear regime. The spatial variation of the curvature casts doubt on the suitability of an analysis based on constant curvature. The most widely used analysis of this type is Stoney's (1909), which is routinely used to connect measured (uniform) curvature to film stress in film/substrate systems.

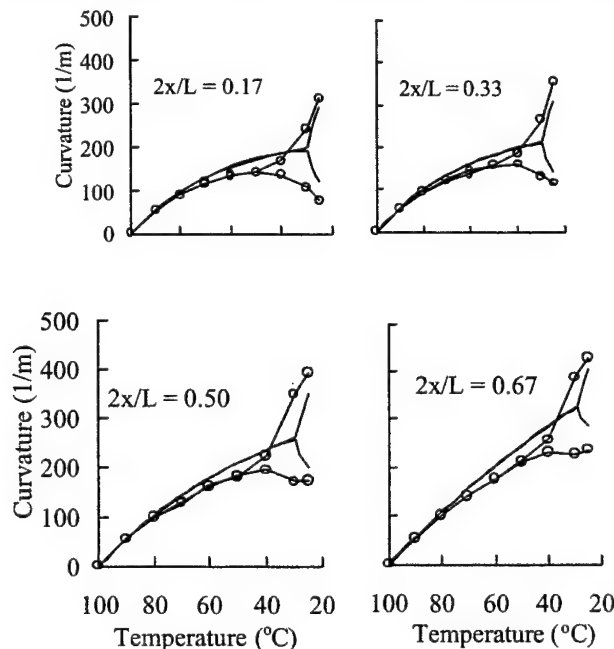


Figure T8-3-10: Point wise curvature as function of temperature change for the $L = 300 \mu\text{m}$ structure at four locations, $2x/L$. Solid lines are predictions and the open circles are measurements.

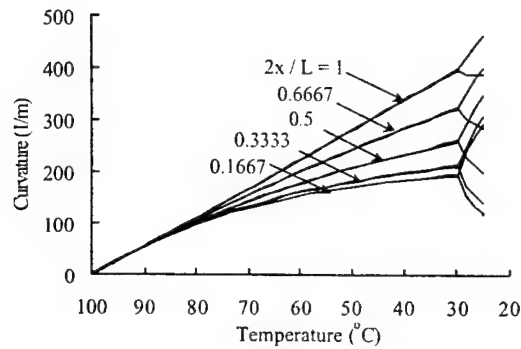


Figure T8-3-11: Predicted pointwise curvature as function of temperature change for the $L = 300 \mu\text{m}$ structure at various positions $2x/L$ along the x-axis ($y=0$).

In Figure T8-3-12 we plot the critical average curvature at which the bifurcation in the equilibrium shape occurs as a function of the plate size L . Three results are shown: an analytical prediction from the constant curvature calculation of Salamon and Masters (1995), results from the finite element calculations, and the measurement for the $L = 300 \mu\text{m}$ sample. Despite the fact that the constant curvature approximation becomes questionable for larger plate sizes, the model of Salamon and Masters for the critical curvature is a good approximation as seen by the good agreement with the finite element calculations, at least for the elastic mismatch and plate sizes considered here. Unfortunately we only show a single measurement, but it is accurately described by both the analytical and finite element results.

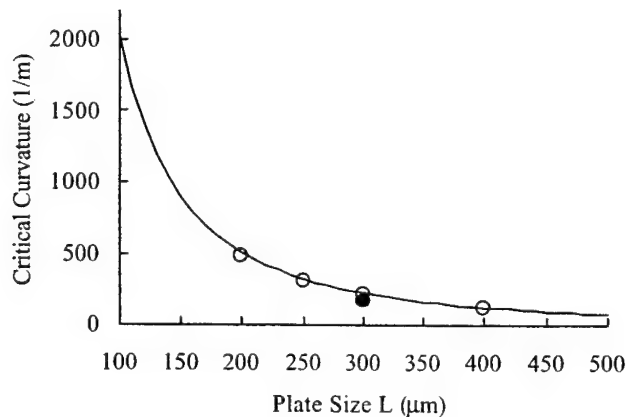


Figure T8-3-12: Critical average curvature for bifurcation as a function of plate size for the gold/polysilicon microstructures. The solid line is the analytical prediction of Salamon and Masters (1995) based on the constant curvature assumption. The open symbols are predictions from the finite element calculations and the filled symbol is the measurement.

8.4 Linear and geometrically nonlinear behavior of gold/polysilicon partially covered plate microstructures subjected to thermal loading

Figure T8-4-1 shows measured deformed shapes for the polysilicon plates with square gold pads. Without a gold pad, there is a small, roughly spherical, deformation due to processing-induced intrinsic stresses. For the smallest gold pad, the deformed shape is also roughly spherical, corresponding to the shape that is predicted by a linear analysis. However, as the size of the gold pad is further increased, the deformed shape changes dramatically. For the two larger gold pads it is nearly cylindrical. Thus, the deformed shape, as a function of gold pad size, exhibits a bifurcation as the pad size increases. In this case, the deformed shapes exhibit a nearly cylindrical curvature. Figure T8-4-2 shows similar measurement results for the polysilicon plates with circular gold pads. They too show a bifurcation from spherical to cylindrical curvature as the pad size increases. Interestingly, though, we observe what

appear to be two stable modes for the specimens with larger gold pad: a cylindrical mode deformed across the flats of the polysilicon plate, and a cylindrical mode deformed across the corners of the polysilicon plate. These deformed shapes cannot be predicted from linear theory.

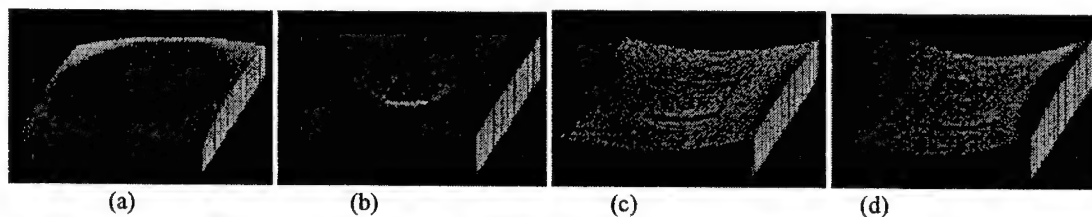


Figure T8-4-1: Measured room temperature deformed shapes of polysilicon ($450\ \mu\text{m} \times 450\ \mu\text{m}$)/gold ($L \times L$) test structures as a function of gold pad dimensions: a) $L = 0\ \mu\text{m}$, b) $L = 100\ \mu\text{m}$, c) $L = 150\ \mu\text{m}$, d) $L = 200\ \mu\text{m}$.

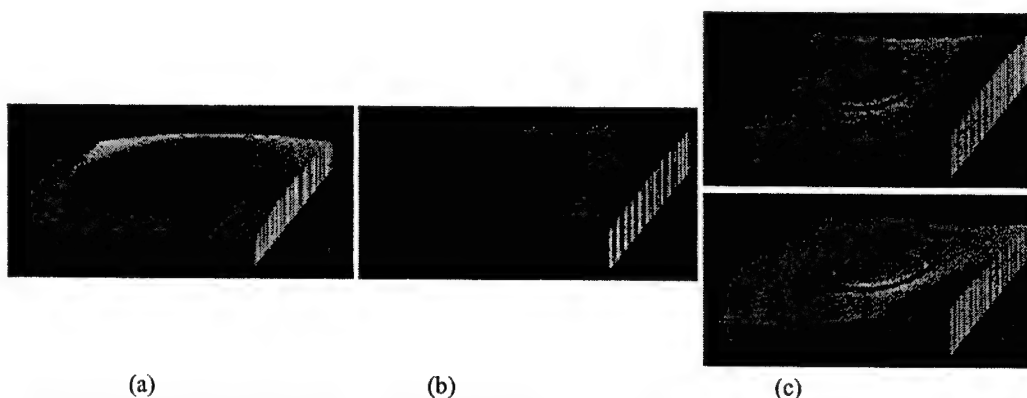


Figure T8-4-2: Measured room temperature deformed shapes of polysilicon ($450\ \mu\text{m} \times 450\ \mu\text{m}$)/gold ($D = \text{diameter}$) test structures as a function of gold pad dimensions: a) $D = 0\ \mu\text{m}$, b) $D = 100\ \mu\text{m}$, c) $D = 150\ \mu\text{m}$.

In order to better understand the deformation of partially covered structures, we designed a series of gold/polysilicon partially covered plate microstructures and fabricated them using MUMPs. A CAD layout of the test structures is shown in Figure T8-4-3. All test structures were supported by $16\ \mu\text{m}$ diameter polysilicon post in the center of the plate.

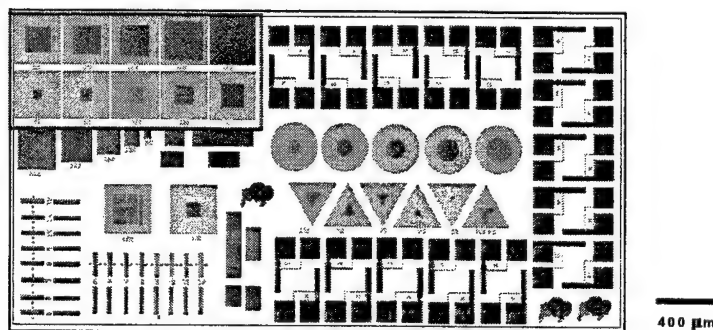


Figure T8-4-3: CAD layout of test structures to understand and guide modeling of MEMS deformation. The gray areas are polysilicon ($1.5\ \mu\text{m}$ thick) and the teal areas are gold pads ($0.5\ \mu\text{m}$ thick).

We measured the full-field deformation of the partially covered gold/polysilicon plate structures as a function of temperature change using an interferometric microscope and a custom-built thermal chamber that is covered by a quartz window to allow optical access. From the measured $w(x,y)$, we calculated the curvatures. Measured room temperature deformed shapes of polysilicon ($300\ \mu\text{m} \times 300\ \mu\text{m}$)/gold ($L \times L$) test structures are shown in Figure T8-4-4. The $L=140\ \mu\text{m}$ structure gives a symmetric deformation. The $L=160\ \mu\text{m}$ structure shows a little non-

symmetric deformation but no significant bifurcation. Bifurcation occurs for $L=180\text{ }\mu\text{m}$, $L=200$, $L=250$, and $L=300\text{ }\mu\text{m}$ structures.

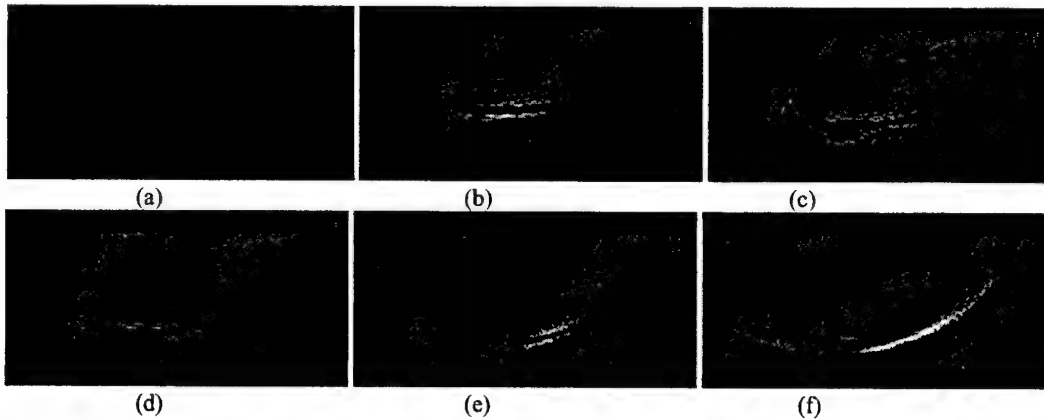


Figure T8-4-4: Measured room temperature deformed shapes of polysilicon ($300\text{ }\mu\text{m} \times 300\text{ }\mu\text{m}$)/gold ($L \times L$) test structures as a function of gold pad dimensions. (a) $L = 140\text{ }\mu\text{m}$, (b) $L = 160\text{ }\mu\text{m}$, (c) $L = 180\text{ }\mu\text{m}$, (d) $L = 200\text{ }\mu\text{m}$, (e) $L = 250\text{ }\mu\text{m}$, (f) $L = 300\text{ }\mu\text{m}$.

A finite element model was built which assumes the structures are stress free at $100\text{ }^{\circ}\text{C}$. Measured and predicted results showed good agreement. Bifurcation occurs from structures with $L=180\text{ }\mu\text{m}$ gold pad and larger. The curvature development in x and y direction from $100\text{ }^{\circ}\text{C}$ to room temperature ($25\text{ }^{\circ}\text{C}$) are shown in Figure T8-4-5 for $L = 180\text{ }\mu\text{m}$ and $250\text{ }\mu\text{m}$. Bifurcation temperature, the temperature at which the curvatures in x and y direction show significant difference, increases from $L=180\text{ }\mu\text{m}$ to $L=250\text{ }\mu\text{m}$. But, does the structure with a larger pad always bifurcate earlier than the structure with a smaller pad? The answer is no. Both experiment and model show that the $L=300\text{ }\mu\text{m}$ structure, which is a fully covered structure, bifurcates later. Figure T8-4-6 (a) shows the bifurcation temperatures are roughly $35\text{ }^{\circ}\text{C}$ for $L=180\text{ }\mu\text{m}$ and $45\text{ }^{\circ}\text{C}$ for $L=250\text{ }\mu\text{m}$, respectively. But in Figure T8-4-6 (b), the bifurcation temperature for $L=300\text{ }\mu\text{m}$ drops to about $35\text{ }^{\circ}\text{C}$.

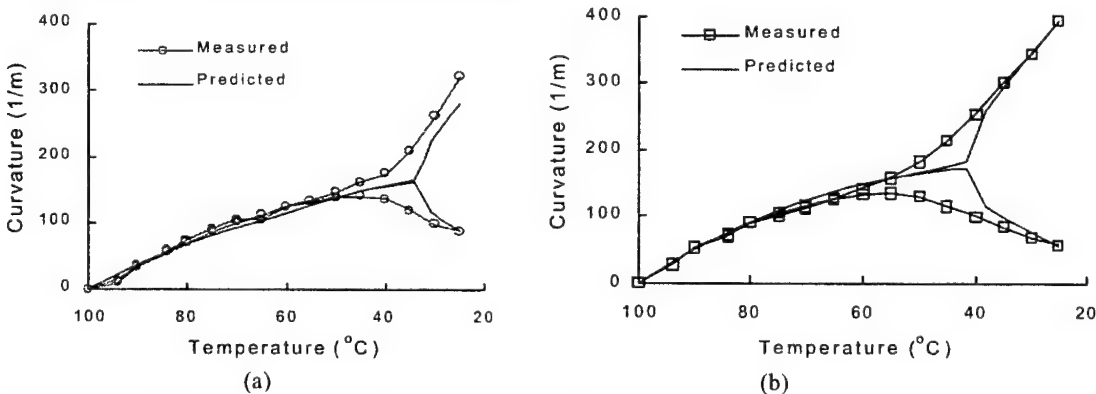


Figure T8-4-5: Measured and predicted curvature development during the cooling process from $100\text{ }^{\circ}\text{C}$ to room temperature for the center supported bilayer structures. The bilayer structures are composed of polysilicon plates ($W \times W$, $W=300\text{ }\mu\text{m}$) and partially covering gold pad ($L \times L$): (a) $L=180\text{ }\mu\text{m}$, (b) $L=250\text{ }\mu\text{m}$.

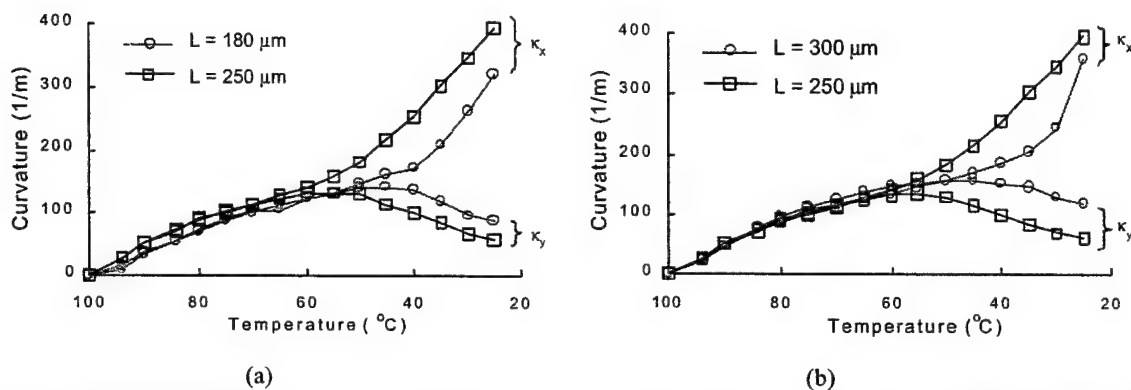


Figure T8-4-6: Experiment result shows: (a) the L=250 μm structure bifurcates earlier than the L=180 μm structure, (b) the L=250 μm structure bifurcates earlier than the L=300 μm structure.

To further understand the curvature development of partially covered structures during the cooling process, we parametrically studied the curvature development during the cooling process of partially covered gold/polysilicon plate. We fix the size of polysilicon plate (300 $\mu\text{m} \times 300 \mu\text{m}$) and vary the size of gold pad ($L \times L$) for $L = 100, 150, 175, 200, 225, 250, 275,$ and $300 \mu\text{m}$. The predicted results are shown in Figure T8-4-7. All the averaged curvatures are calculated over 100 μm . Figure T8-4-7 (a) shows that as L increases from 100 μm to 225 μm , bifurcation temperature increases. Also the curvature before the bifurcation point decreases. But as L increases further from 225 μm to 300 μm , as shown in Figure T8-4-7 (b), the reverse trend occurs, i.e. the bifurcation temperature decreases and the curvature before the bifurcation point increases.

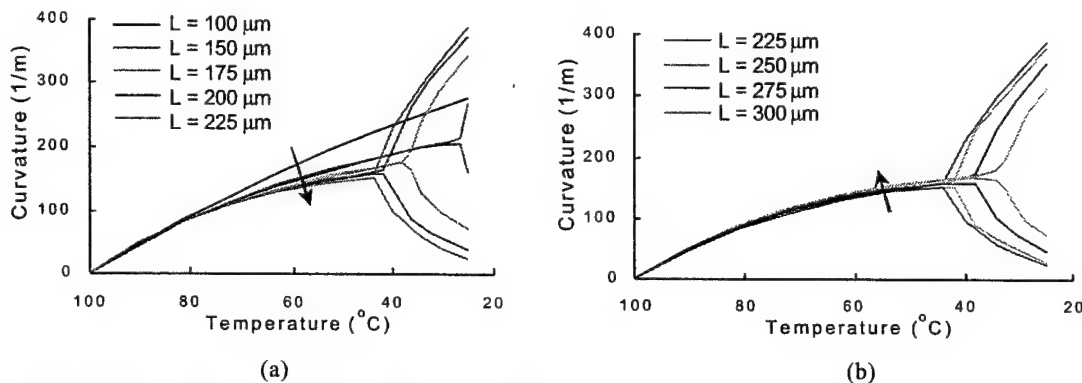


Figure T8-4-7: Prediction results of the cooling process from 100 $^{\circ}\text{C}$ to room temperature for *square* polysilicon plates (300 $\mu\text{m} \times 300 \mu\text{m}$) with *square* gold pads ($L \times L$). (a) $L = 100, 150, 175, 200,$ and $225 \mu\text{m}$; (b) $L = 225, 250, 275,$ and $300 \mu\text{m}$.

In order to study the effect of the peripheral polysilicon, we compared the deformation of a fully covered structure and a partially covered structure, in which the gold pads have the same size of 200 $\mu\text{m} \times 200 \mu\text{m}$, but the size of polysilicon is 200 $\mu\text{m} \times 200 \mu\text{m}$ in the fully covered structure and 300 $\mu\text{m} \times 300 \mu\text{m}$ in the partially covered one. We measured the average curvatures over the gold pad. Both measurement and prediction showed that the fully covered one doesn't bifurcate, but with a peripheral polysilicon plate, the partially covered structure bifurcated for a -75°C temperature change. This suggests that the uncovered circumference polysilicon can significantly affect the deformation behavior of the center gold/polysilicon plate. We also find that before the bifurcation point, the partially covered structure has lower curvature than fully covered one. This suggests that the peripheral plate restrict the deformation of the center part.

8.5 Thermal cycle experiment

Figure T8-5-1 shows the curvature variation during the thermal cycle experiment between 190 °C and room temperature (24 °C) of a center supported bilayer gold (0.5 μm thick) / polysilicon (3.5 μm thick) square plate ($L \times L$, $L = 200 \mu\text{m}$). The heating/cooling rate is about 10°C/3.5 minutes. During the first heating cycle thin film undergoes recrystallization and grain growth. There is no further grain growth in the subsequent thermal cycles. As shown in Figure T8-5-1, the curvature development repeats in the temperature cycles after the first heating cycle.

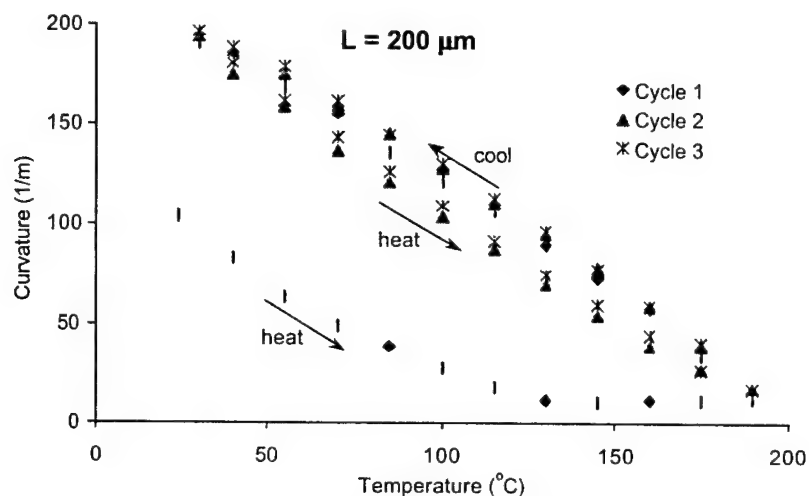


Figure T8-5-1: Curvature variation during the thermal cycle process between 190 °C and room temperature for the center supported gold/poly1+poly2 200 $\mu\text{m} \times 200 \mu\text{m}$ square plate.

8.6 Study on stress relaxation

For many applications, it is important to accurately control the deformation of multilayer material structures in order to meet the performance requirements, especially for structures subjected to thermal loading and/or operated at elevated temperatures. However stress relaxation and creep can significantly influence deformation and compromise structural integrity.

In this research we studied both experimentally and theoretically the stress relaxation behavior of a series of gold/polysilicon MEMS plate microstructures fabricated by the MUMPS surface micromachining process and subjected to thermal loading. We measured, using an interferometric microscope with a custom-built temperature chamber, full field deformed shapes of square ($L \times L$) gold (0.5 μm thick)/polysilicon (1.5 or 3.5 μm thick) plate structures of sizes $L = 200 \mu\text{m}$ and $L = 300 \mu\text{m}$. The structures were thermal cycled between room temperature and 190°C to stabilize the microstructure. After the initial thermal cycle, the structures were cooled from 190 °C to 120 °C and held at 120°C for about 7 days. We measured full-field displacements (and from these determined the average curvatures in x and y directions) as a function of temperature during the initial thermal cycle and the subsequent temperature drop 190 °C to 120 °C, and as a function of time at 120 °C. The deformation during the temperature drop results from thermoelastic phenomena, and includes linear and geometrically-nonlinear behavior. In fact, for microstructures within certain size and thickness regimes, the equilibrium configurations exhibit a bifurcation from symmetric to strongly nonsymmetric deformation, i.e., buckling. During the isothermal hold, stress relaxation was observed in all of the microstructures. Interestingly, for microstructures that have *buckled* during the thermoelastic deformations, the stress relaxation can cause them to *unbuckle*. Typical results are shown in the Figure T8-6-1.

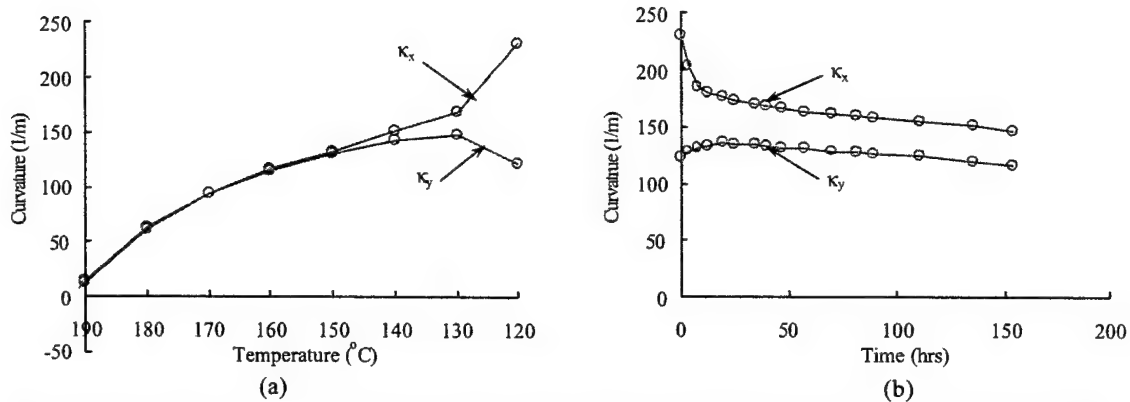


Figure T8-6-1: Measured curvature development during cooling and a subsequent stress relaxation process at elevated temperature of a $300\text{ }\mu\text{m} \times 300\text{ }\mu\text{m}$ gold ($0.5\text{ }\mu\text{m}$ thick) / polysilicon ($1.5\text{ }\mu\text{m}$ thick) plate structure: (a) Curvature development during cooling from $190\text{ }^{\circ}\text{C}$ to $120\text{ }^{\circ}\text{C}$; (b) Curvature development due to the stress relaxation when the structure was held at a constant temperature of $120\text{ }^{\circ}\text{C}$.

We attempted to model the stress relaxation process by assuming simple power-law creep $\dot{\epsilon} = A\sigma^n$ in the gold, and assuming the polysilicon did not relax at the modest temperature of $120\text{ }^{\circ}\text{C}$. We found that a stress component of $n = 7$, provided self-consistent results among all measurements, but such agreement required different values of A for the different thickness microstructures (Figure T8-6-2). The microstructural reasons for this are unclear, but these results resonate with similar studies of thin films on thick substrates in microelectronics contexts. Interestingly, in our samples there are substantial stress variations through the thicknesses of the layers since they are of comparable thickness.

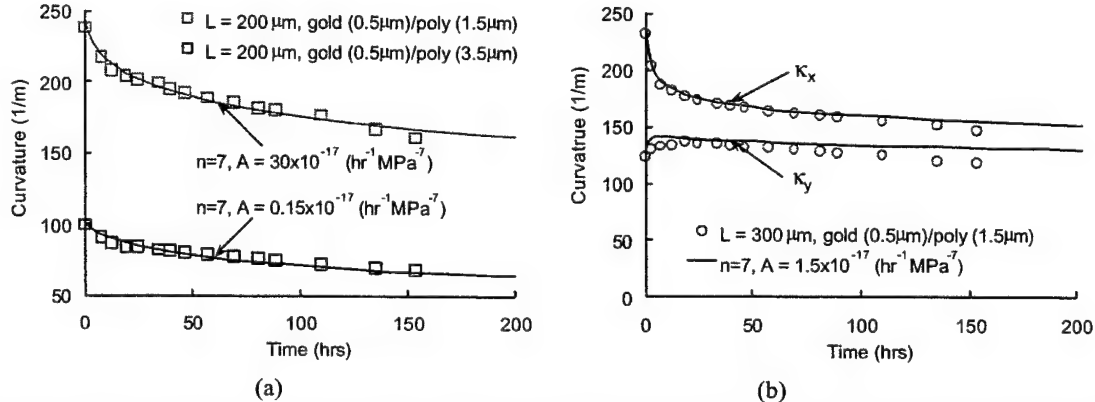


Figure T8-6-2: Measured and predicted curvature development during isothermal stress relaxation process at elevated temperature of $120\text{ }^{\circ}\text{C}$. (a) $200\text{ }\mu\text{m} \times 200\text{ }\mu\text{m}$ gold / polysilicon plate structure with different thickness of polysilicon; (b) $300\text{ }\mu\text{m} \times 300\text{ }\mu\text{m}$ gold/polysilicon plate structure.

8.7 Solder deposition test

Indium solder was deposited on top of the gold pad of the gold/polysilicon bilayer structures using evaporator (Figure T8-7-1). In order to study the intermetallic reaction between indium and gold, we cast the structures into epoxy and polished the cross section. Energy dispersive X-ray (EDS/EDX) analysis, which detects elements by their emitted X-ray energy signature, was carried out to test the elements on the cross section. Figure T8-7-1 (b) shows the position of dot test and line scan test.

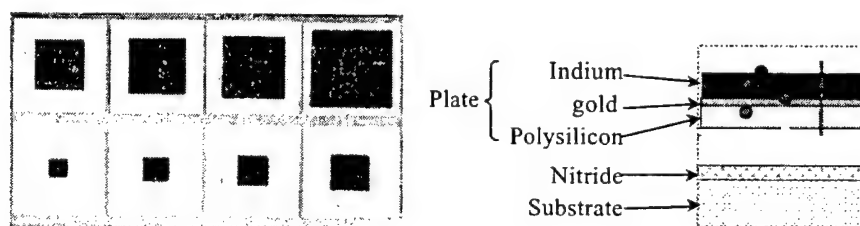


Figure T8-7-1: (a) Multilayer structures after indium deposition; (b) schematic diagram of the plate and substrate, red dots indicate the locations of the dot test, red lines indicate the locations of the line scan test.

The line scan test result is shown in Figure T8-7-2. Gold and indium distributed almost at the same area, which indicate the intermetallic reaction between gold and indium. For the scan length of $6.076\text{ }\mu\text{m}$, the intermetallic layer is about $1.5\text{ }\mu\text{m}$. The dot test result is shown in Figure T8-7-3. Gold and indium are found at both the very top of the plate and in the middle of the plate. One dot from the very top of the plate shows relative equal percent of gold and indium, which suggest compound AuIn is formed. The other dot from the middle of the plate shows two times of indium as gold, which suggest the compound AuIn_2 . Dot mapping test result is shown in Figure T8-7-4. This again shows intermetallic reaction between gold and indium.

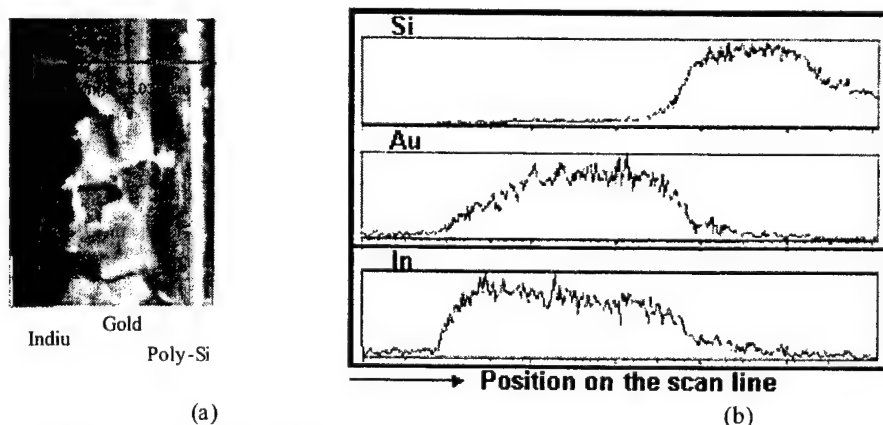


Figure T8-7-2: (a) SEM picture of the line scan area. (b) Line scan result which shows Si, Au, and In element component distribution along the scan line.

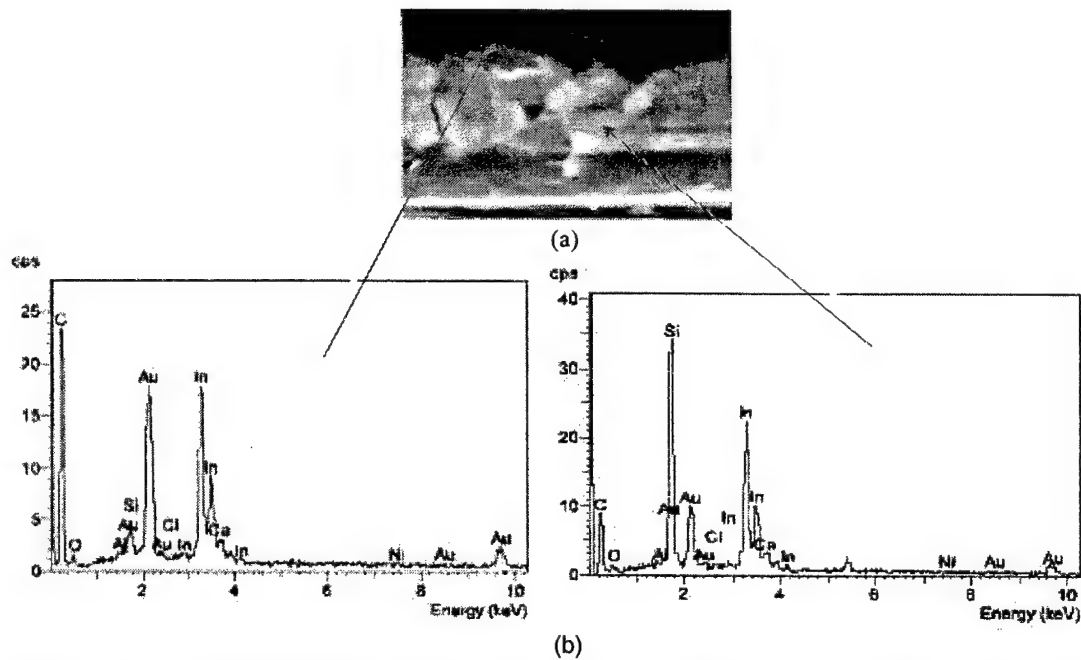


Figure T8-7-3: (a) SEM picture of the dot test position. (b) Dot test results which show element component at the point.

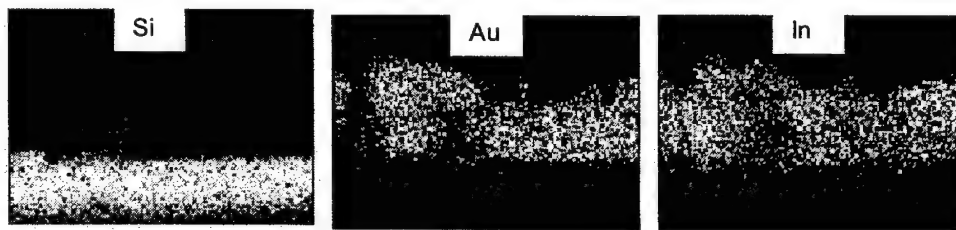
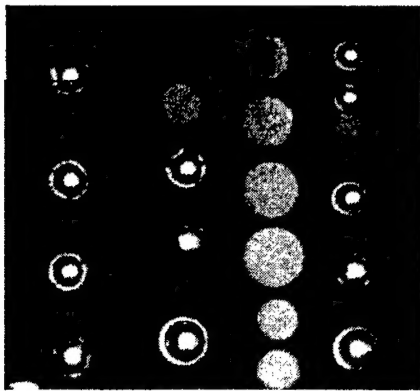


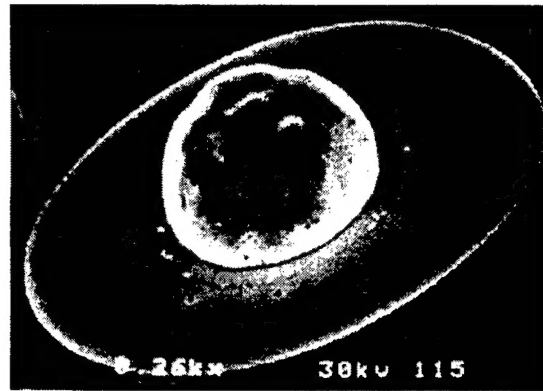
Figure T8-7-4: Dot map results which show element distribution at the area.

8.8 Solder reflow test

So far we discussed our study on the deformation behavior of multilayer structures before solder self-assembly. How would these structures deform after they are assembled? We did the solder reflow test on some partially covered structures composed of circular polysilicon plate and circular gold pad, as shown in figure T8-8-1 (a). The solder balls are 60In/40Pb alloy and the diameter is 5 mil. During the reflow process, the solder will spread only on the gold pad and the shape of the solder after reflow is formed according to the minimum surface energy principle. At about 205 °C, the solder was fully reflowed, and then the structures were cooled down to room temperature in the reflow chamber. Figure T8-8-1 (b) is a SEM picture of room temperature solder ball after reflow; the gold pad size is 200 μm in diameter and the polysilicon plate is 450 μm in diameter. Since the thickness of the polysilicon plate is only 1.5 μm , it is very thin compared with the dimension of the center solder.



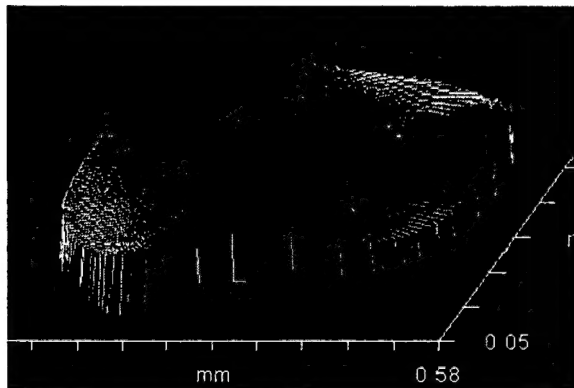
(a)



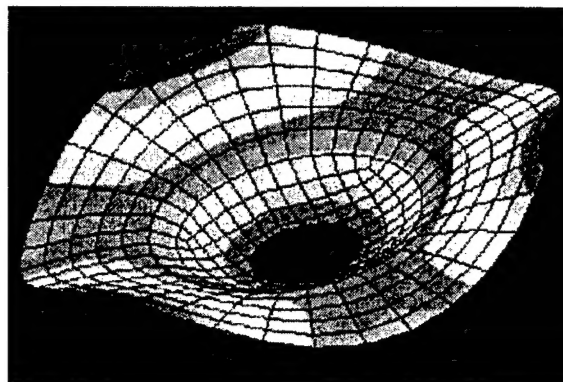
(b)

Figure T8-8-1: (a) 5 mil solder balls were put on top of circular structures and reflowed ; (b) SEM picture of room temperature solder shape after reflow.

Although the center solder part can't be measured under the microscope, the deformation of the uncovered part of the polysilicon plate can still be measured after solder reflow test. Figure T8-8-2 (a) shows the measured deformation of the uncovered part of polysilicon plate (diameter $D = 450 \mu\text{m}$) after the reflow process. The circumference polysilicon plate shows a 3-fold bifurcation. This happens because the solder increases the bending stiffness of the center part and thus makes the bending of the center part difficult. But as the temperature change increases, the structure can not deform symmetrically due to the geometric nonlinearity. Thus the circumference polysilicon plate has to fold around and the 3-fold bifurcation occurs. Figure T8-8-2 (b) shows the predicted deformation from Abaqus, which quantitatively agrees with the experiment result.



(a)



(b)

Figure T8-8-2: Measured and predicted deformation of polysilicon plate with solder in the center. (a) Measured; (b) Predicted.

3. Publications Relevant to This Effort and Technology Transfer

Publications

1. J.R. Reid, V.M. Bright, and J.T. Butler, "Automated Assembly of Flip-Up Micromirrors," *Sensors and Actuators A*, vol. 66, pp. 292-298, 1998.
2. Q.Tan and Y.C. Lee. "Soldering for Optoelectronic Packaging", *IEEE transactions on Components, Packaging and Manufacturing Technology, Part C.*, pp. 28-30, May 1996.
3. P.E. Kladitis, V.M. Bright, K.F. Harsh, and Y.C. Lee, "Prototype microrobots for micro positioning in a manufacturing process and micro unmanned vehicles," *Technical Digest of 12th IEEE International Conference on MicroElectroMechanical Systems – MEMS '99*, pp. 570-575, 17-21 January 1999, Orlando, FL.
4. K.F. Harsh and Y.C. Lee, "Modeling for Solder Self-Assembled MEMS," *Proceedings of SPIE*, San Jose, CA, vol. 3289, pp. 177-184, Jan. 1998.
5. K. F. Harsh, R. S. Irwin, and Y.C. Lee, "Solder Self-Assembly for MEMS," *Proceedings of the 44th International Instrumentation Symposium*, Reno, NV, vol. 44, pp. 249-255, 3-7 May 1998.
6. K. F. Harsh, V. M. Bright, and Y. C. Lee, "Solder Self-Assembly for Three-Dimensional Microelectromechanical Systems," *Sensors and Actuators A*, vol. 77, pp. 237-244, 1999.
7. M. L. Dunn, Ya. Zhang, J. Roy, P. E. W. Labossiere, and V. M. Bright, "Nonlinear Deformation of Multilayer MEMS Structures," *Proc. 1999 ASME IMECE MEMS Symposium*, MEMS-Vol. 1, pp. 75-79, Nashville, TN, Nov. 1999.
8. P.E. Kladitis, K.F. Harsh, V.M. Bright, and Y. C. Lee, "Three-Dimensional Modeling of Solder Shape for the Design of Solder Self-Assembled Micro-electro-mechanical Systems," *Proc. 1999 ASME IMECE MEMS Symposium*, MEMS-Vol. 1, pp. 11-18, Nashville, TN, Nov. 1999.
9. P.E. Kladitis and V.M. Bright, "Prototype microrobots for micro positioning and micro unmanned vehicles," *Sensors and Actuators A.*, Vol. 80, pp. 132-137, 2000.
10. K. F. Harsh, V. M. Bright and Y. C. Lee, "Study of Micro-scale Limits of Solder Self-assembly for MEMS", *Proc. of the Electronics and Components Technology Conference*, pp.1690-1695, Las Vegas, Nevada, May 21-24, 2000.
11. K. F. Harsh, P. E. Kladitis, Y. H. Zhang, M. L. Dunn, V. M. Bright, and Y. C. Lee, "Tolerance and Precision Study for Solder Self-Assembled MEMS," *Proceedings of the 2000 Micro-Opto-Electro-Mechanical Systems Conference – MOEMS 2000*, Vol. 4075, pp. 173-184, Glasgow, Scotland, May 22-25, 2000.
12. R.J. Linderman and V.M. Bright, "Optimized Scratch Drive Actuator for Tethered Nanometer Positioning of Chip Sized Components," *Technical Digest 2000 Solid-State Sensor and Actuator Workshop*, pp. 214-217, June 4-8, 2000, Hilton Head Island, SC.
13. P.E. Kladitis and V.M. Bright, "Novel Resistive Point Heater for MEMS Remote Solder Self-Assembly," *Proceedings of the 2000 International Mechanical Engineering Congress and Exposition (IMECE 2000)*, MEMS-Vol. 2, pp. 161-167, Nov. 5-10, 2000, Orlando, Florida.
14. M.L. Dunn, Y. H. Zhang, and V. M. Bright, "Linear and Geometrically Nonlinear Behavior of Metal/Polysilicon Plate Microstructures Subjected to Temperature Changes," *Proceedings of the 2000 International Mechanical Engineering Congress and Exposition (IMECE 2000)*, MEMS-Vol. 2, pp. 207-213, Nov. 5-10, 2000, Orlando, Florida.
15. P.E. Kladitis, R.J. Linderman, and V.M. Bright, "Solder Self-Assembled Micro Axial Flow Fan Driven by a Scratch Drive Actuator Rotary Motor," *Proc. 14th IEEE International Micro Electro Mechanical Systems Conference (MEMS 2001)*, pp. 598-601, 21-25 Jan. 2001, Interlaken, Switzerland.
16. K.F. Harsh, V.M. Bright, Y.C.Lee, "Micro-Scale Limits of Solder Self-Assembly for MEMS", to appear in the *International Journal of Micro-electronics Packaging*, vol. 1, 2001.
17. K.F. Harsh, V.M. Bright, Y.C. Lee, "Design Optimization of Surface Micro-machined Self-assembled MEMS Structures" to appear in the proceedings of (InterPACK01) The Pacific Rim International, Intersociety, Electronic Packaging Technical Conference & Exhibition, July 8-13, 2001, Kauai, Hawaii.
18. Dunn, M. L., Zhang, Y., and Bright, V. M., 2001, "Deformation and Structural Stability of Layered MEMS Plate Microstructures Subjected to Thermal Loading," *Mechanical Properties of Structural Films*, ASTM STP 1413, in press.

19. K. Gall, M. L. Dunn, B. Corff, and Y. Zhang, "Modeling the Deformation of Bilayer Thin Films for MEMS," to appear in the proceedings of the Symposium on the Modeling and Simulation of Micro and Nano Systems at the 6th US National Congress on Computational Mechanics, Dearborn, MI, Aug. 1-4, 2001.

Patents

1. K. F. Harsh, P. E. Kladitis, Y. C. Lee, V. M. Bright, W. Zhang, M.L. Dunn, Y. Zhang "Controlled Surface Tension or Shrinkage Assembly of 3D MEMS," Provisional Patent Application, University of Colorado - Boulder, May 18, 2001.
2. R. J. Linderman, P. E. Kladitis, and V. M. Bright, "Micro Axial Flow Fans," Provisional Patent Application, University of Colorado - Boulder, June 4, 2001.

Student Thesis

1. R.J. Linderman, Development of the Scratch Drive Actuator Motor, Master's Thesis, University of Colorado at Boulder, Dept. Mechanical Engineering, Boulder, CO 80309, 2000.
2. K.F. Harsh, "Design Optimization for MEMS Self-Assembly", Doctoral Thesis, University of Colorado, Department of Mechanical Engineering, Boulder, CO 80309, 2001.
3. P.E. Kladitis "Issues in the Design, Manufacture, Processing, Modeling and Assembly Precision of Complex Solder Self-Assembled Micro-Electromechanical Systems", Doctoral Thesis, University of Colorado, Department of Mechanical Engineering, Boulder, CO 80309, 2001.

Technology Transfer

SBIR/STTR Phase I,II, NSF

Company: Sporian Microsystems, Boulder, CO 80303

Project Title: Novel Joining Method for Self-Assembly of Reliable Three Dimensional Micro-Electro-Mechanical Systems.

***MISSION
OF
AFRL/INFORMATION DIRECTORATE (IF)***

*The advancement and application of Information Systems Science
and Technology to meet Air Force unique requirements for
Information Dominance and its transition to aerospace systems to
meet Air Force needs.*